Magnetometry and Magnetic Imaging of Ferromagnetic Micro- and Nanostructures

Dissertation
zur Erlangung des Doktorgrades
des Fachbereichs Physik
der Universität Hamburg

vorgelegt von
René Eiselt
aus Ratzeburg

Hamburg
2006

Gutachter der Dissertation:	Prof. Dr. U. Merkt Prof. Dr. W. Hansen
Gutachter der Disputation:	Prof. Dr. U. Merkt Prof. Dr. D. Heitmann
Datum der Disputation:	24.03.2006
Vorsitzende des Prüfungsausschusses:	Prof. Dr. D. Pfannkuche
Vorsitzender des Promotionsausschusses:	Prof. Dr. G. Huber
Dekan des Fachbereichs Physik:	Prof. Dr. G. Huber

Abstract

This thesis deals with lateral ferromagnetic micro- and nanostructures and $CoPt_3$ nanocrystals that are suitable for applications in magnetoelectronics and in future spintronic devices. The main fabrication technique used for pattering the lateral nanostructures to electrodes is electron-beam lithography. This technique allows the preparation of structures with lateral sizes of less than 100 nm with a position accuracy of 10 nm. The ferromagnetic materials are deposited by electron-beam and thermal evaporation as well as by sputter processes. The thickness of the micro- and nanostructures typically are about 20 nm.

For the magnetic characterization of the electrodes and $CoPt_3$ nanoparticles various techniques are employed. The domain configurations of the micro- and nanostructures are investigated with magnetic-force microscopy (MFM) and magnetic transmission x-ray microscopy (MTXM). Magnetic-force microscope has been performed at the Institute for Applied Physics in Hamburg. Magnetic transmission x-ray microscopy has been carried out at the Center for X-Ray Optics at the Advanced Light Source (ALS) in Berkeley, USA. MTXM is a non-invasive technique, i. e., it allows the measurement of stray field interaction of ferromagnetic microelements. Magnetic-force and magnetic transmission x-ray microscopy also have been employed to image the magnetization configurations of the same microstructured electrodes in order to compare these two imaging methods.

Hall micromagnetometry is an excellent non-invasive and adaptable tool to detect local stray fields of nanostructured ferromagnets. A particular advantage of Hall micromagnetometry concerns the wide length scale of structure sizes that can be studied. In the submicrometer range ferromagnetic electrodes suitable for spintronic devices in spin-valve and spin-FET-configuration have been investigated with this method. The high sensitivity of microstructured Hall sensors for nanometer-sized ferromagnetic elements is demonstrated by the detection of $CoPt_3$ nanoparticles that have been spin-coated onto the Hall sensors. Magnetic properties like the coercive field, the blocking temperature, and the switching behavior of the particles have been determined.

Inhaltsangabe

Die vorliegende Arbeit befasst sich mit der Untersuchung von mikro- und nanostrukturierten Elektroden aus ferromagnetischen Materialien und $CoPt_3$ Nanopartikeln, die für Anwendungen in der Magnetoelektronik sowie in der Spinelektronik geeignet sind. Als zentrales Herstellungsverfahren zur Präparation der Elektroden wurde die Elektronenstrahllithographie verwendet. Mit diesem Verfahren können Strukturen mit lateralen Abmaßen von weniger als 100 nm bei einer Positionierungsgenauigkeit von 10 nm definiert werden. Die Deposition der ferromagnetischen Schichten erfolgte durch elektronenstrahlgestütztes und thermisches Aufdampfen sowie durch Sputter-Prozesse. Die ferromagnetischen Schichten haben eine typische Dicke von 20 nm.

Zur magnetischen Charakterisierung der Elektroden und der $CoPt_3$ Nanopartikel stehen verschiedene Messmethoden zur Verfügung. Die Domänenstrukturen der Elektroden wurden mit Hilfe der Magnetkraft-Mikroskopie (MFM) und der magnetischen Transmissions-Röntgenmikroskopie (MTXM) untersucht. Die Messungen mit dem Magnetkraft-Mikroskop fanden am Institut für Angewandte Physik in Hamburg statt. Die Ergebnisse der magnetischen Transmissions-Röntgenmikroskopie wurden am Center for X-Ray Optics an der Advanced Light Source in Berkeley gewonnen. MTXM ist insbesondere für die Untersuchung von Streufeld-Wechselwirkungen zwischen Elektroden geeignet. Beide Verfahren zur Abbildung von Magnetisierungszuständen wurden auf dieselben ferromagnetischen Nanostrukturen angewendet, so dass ein Vergleich der Mikroskopie-Techniken möglich war.

Die Hall-Mikromagnetometrie stellt eine wichtige nichtinvasive und an verschiedene Probengrößen anpassbare Methode zur Detektion von magnetischen Streufeldern dar. Es wurden ferromagnetische Elektroden mit einer lateralen Ausdehnung von kleiner einem Mikrometer untersucht, die für die Verwendung in spinelektronischen Bauelementen geeignet sind. Die hohe Empfindlichkeit der Hall-Sensoren wird durch die Detektion von einer Monolage $CoPt_3$ Nanopartikeln demonstriert. Mit Hilfe der Hall-Magnetometrie konnten magnetische Eigenschaften wie das Koerzitivfeld, die dipolare Wechselwirkung und die Temperaturabhängigkeit der Magnetisierung der $CoPt_3$ Nanopartikel bestimmt werden.

Contents

1. Introduction

Magnetism plays a fundamental role in the evolution of computer memory and storage technology. Most apparent are the enduring applications as permanent data storage systems, evolving through approximately ten orders of magnitude in density from tapes and drums in the late 1940s to the tape and disk storage systems of today. From the mid-1950s into the early 1970s magnetic core elements were predominantly used as active computer memory. At that time the high performance of the magnetic core memory in reliability and access time was not achieved by semiconductor memories for several years [1]. Further evolution of core memories would have been possible, but by the late 1960s it had become evident that semiconductor bipolar and field-effect transistor memories, e. g. dynamic random access memory (DRAM), would undergo even more rapid advances in density and performance at lower power consumption. Though, higher-performance plated-wire and thin-film magnetic memories that were being developed at that time never saw widespread use.
In the mid-1980s magnetic memories with read operations based on the use of anisotropic magnetoresistance (AMR) rather than magnetic induction were pursued for the market of non-volatile and radiation hard memories [3]. Later, the discovery of the giant mag-

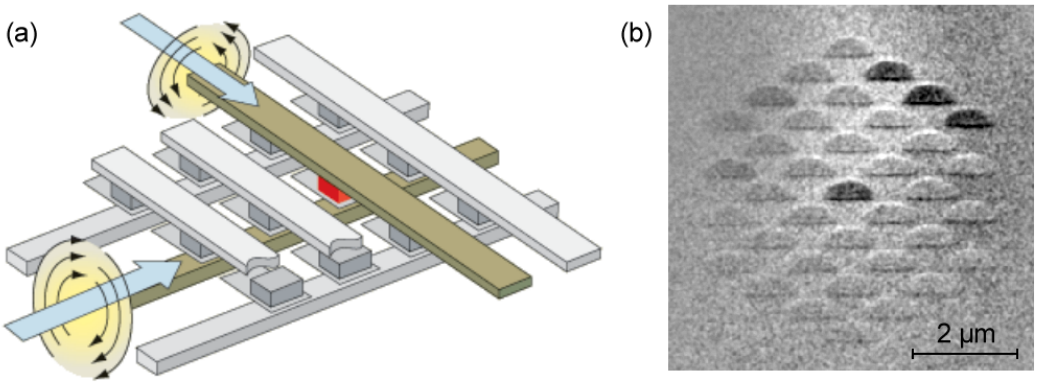

Fig. 1.1.: (a) Illustration of the MRAM write operation, taken from Ref. [2]. The selected magnetic tunnel junction (red) is situated between the selected word and bit line (both olive) which are orthogonal to each other. The vector sum of the magnetic fields at the tunnel junction must be sufficient to switch its magnetization. (b) Magnetic transmission X-ray microscopy (MTXM) image of an hexagonal array of Fe "beans" suitable for MRAM bits with a quasi-single domain magnetization. The magnetization of the four dark grey beans have switched in an external magnetic field.

netoresistance (GMR) in magnetic multilayers and sandwiches and the invention of the spin-valve device allowed innovative applications of magnetic materials in storage technology [4]. The great promise of GMR read-head sensors in hard disk drives led to the proposal for a new "universal" spin-valve-based memory which could simultaneously achieve high speed, high density, and non-volatility. The realization of the so-called magnetic random access memory (MRAM) was provided by the development of the magnetic tunnel junction over the last decade [5]. A schematic drawing of a MRAM device is shown in Fig. 1.1(a). The broader range of applicability has led to widespread research and development activity which aim at demonstrating magnetic tunnel junction RAM with commercial market potential. At the end of 2005 the MRAM Development Alliance (MDA) of IBM and Infineon Technologies Corporation presented a 16 Mb demonstrator chip in 180 nm CMOS technology with the smallest cell size (1.42 μm^2) among multi-megabit MRAM designs.

In recent years technological advances have enabled enormous increases in the storage capacity and in the density of processing units. The success in miniaturization of electronic and magnetic devices is obtained by, e. g., the improvement of lithography processes down to sub-micron dimensions. The physics concerning the structure and composition of theses materials on the nanoscale is treated by nanotechnology which is an emerging set of tools, techniques and unique applications. So far, many other milestones have been achieved in the context of nanotechnology like the invention of the spin-polarized scanning tunneling microscope (SPSTM) capable of imaging individual magnetic atoms [6].

The present thesis deals with the magnetic characterization of ferromagnetic micro- and nanostructures suitable for applications in magnetic memory cells and in future spintronic devices. The study of the magnetic properties of micro- and nanostructures is performed with magnetic-force microscopy (MFM), magnetic transmission X-ray microscopy (MTXM), and Hall micromagnetometry. The imaging techniques MFM and MTXM which provide a spatial resolution of 20 nm [7] and 15 nm [8], respectively, have been used to investigate magnetic domain structures and stray field interaction between adjacent electrodes in great detail. Figure 1.1(b) shows an example of bean-like elements which are suitable for MRAM devices. The iron electrodes have been fabricated with an inter-element distance of 300 nm and a thickness of 20 nm. The image taken with MTXM reveals a quasi-single domain behavior of the magnetic elements within the hexagonal array. In order to extend the understanding of micromagnetic properties regarding, e. g., the stray field distribution of domain walls and domain wall movements both imaging techniques have been applied on the same microstructured elements in dependence of an external magnetic field. The direct comparison of MFM and MTXM images provides new opportunities to understand micromagnetic properties.

Hall micromagnetometry has been further improved in this work. It is an excellent non-invasive and adaptable tool to detect local stray fields of nanostructured ferromagnets. A particular advantage of Hall micromagnetometry concerns the wide scale of the elements structure sizes that can be studied. In the sub-micrometer range ferromagnetic electrodes suitable for spintronic devices [9] in spin-valve and spin-transistor configuration have

been investigated. The sensitivity of microstructured Hall sensors in the nanometer range is demonstrated by the detection of self-assembled $CoPt_3$ nanocrystals. Magnetic properties like the coercive field, the blocking temperature, and the switching behavior of these particles with a diameter of less than 10 nm have been determined.
The thesis is organized as follows: The second chapter describes the preparation techniques applied for the fabrication of the samples and introduces the micro- and nanostructures which have been investigated in this work. Then an overview of the measurement techniques is given including the methods of microscopy. Chapter 3 summarizes the theoretical background of ferromagnetism and micromagnetism of thin-film elements and presents the results obtained by Hall magnetometry, magnetic transmission X-ray microscopy and magnetic-force microscopy on various ferromagnetic micro- and nanostructure. Finally, the imaging techniques are compared. In Chapter 4 the experimental results of the Hall measurements on $CoPt_3$ nanoparticles are shown. The superparamagnetic properties like the blocking temperature and the switching behavior of the particles are discussed. The thesis closes with an outlook and conclusions in Chapter 5.

2. Sample preparation and experimental techniques

In this chapter different preparation techniques applied for the fabrication of the samples are described. The preparation includes optical and electron-beam lithography, sputter and physical vapor deposition of metal films, and plasma enhanced chemical vapor deposition (PECVD) of oxide films. At the end of the chapter a short introduction to the experimental measurement techniques is given. These include transport measurements with Hall micromagnetometry at liquid helium temperatures which have been performed with lock-in technique. Magnetic domain structures have been investigated and imaged with magnetic-force microscopy and magnetic-transmission X-ray microscopy.

2.1. Semiconductor heterostructures and Si_3N_4 membranes

Two different substrates are used for the fabrication of samples. Hall bar structures which are described in the following section are prepared on modulation doped GaAs/AlGaAs heterostructures. The investigation of ferromagnetic domain structures with magnetic-transmission X-ray microscopy (MTXM) is performed with thin membrane windows of less then 200 nm thickness and a lateral size between 1×1 mm^2 and 5×5 mm^2.
The GaAs/AlGaAs heterostructures used throughout this work originate from two different wafers both grown by molecular-beam epitaxy (MBE) [10]. The first one (Q1105HE) has been produced at the Institute of Applied Physics in Hamburg. The other one (B1101) has been grown at the "Lehrstuhl für Angewandte Festkörperphysik" in Bochum.
The MBE allows the fabrication of different III-V semiconductors which also can be compound to ternary alloys. In this sense, the semiconductor systems AlAs and GaAs are prominent candidates. Both alloys have the so-called zincblende structure with nearly the same lattice constant of $d_{\mathrm{AlAs}} = 5.660$ Å and $d_{\mathrm{GaAs}} = 5.653$ Å. In addition, GaAs has a direct bandgap of 1.4 eV at 300 K whereas AlAs shows an indirect bandgap of 2.2 eV [11]. The alloy system $Al_xGa_{1-x}As$ offers the possibility to adjust the bandgap by the stoichiometry x and thus to achieve different electronic and optical properties. Typical values for the stoichiometry are around $x = 0.3$.
The layer sequences of both wafers used in this work are almost equal. In Fig. 2.1(a) a schematic drawing of the GaAs/AlGaAs heterostructure is shown. To reach a smooth surface with zincblende structure a comparatively thick layer of 1000 nm is grown first as buffer. After an undoped $Al_{0.33}Ga_{0.67}As$ spacer layer of 30 nm with the stoichiometry of $x = 0.33$ a silicon doped $Al_{0.33}Ga_{0.67}As$ layer is deposited. The donor concentration

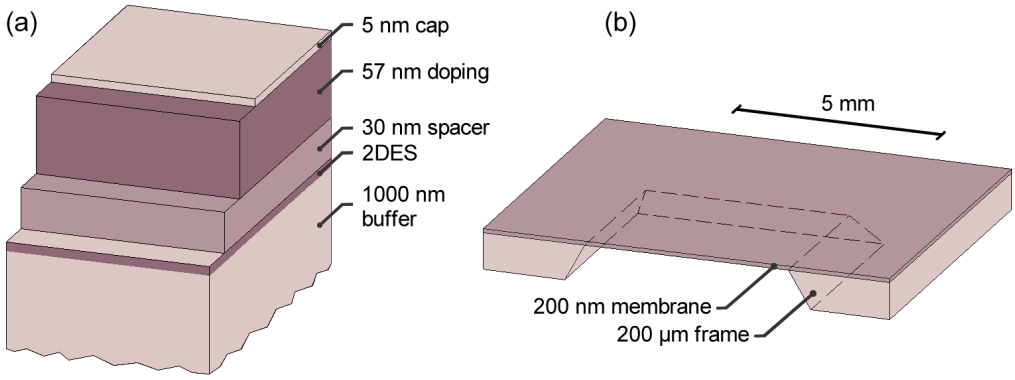

Fig. 2.1.: (a) Schematic drawing of the GaAs/AlGaAs heterostructure layer sequence. The 2DES is located below the 30 nm thick spacer layer. (b) Sectional view of the silicon nitride membrane windows. The membrane upon the silicon substrate has a thickness of merely 200 nm.

is $n_{\mathrm{Si}} = 3.8 \cdot 10^{18}$ cm^{-2} and the thickness 57 nm. Finally, a GaAs cap layer of 5 nm is grown as protection for the doped layer.
The differing bandgaps of the heterostructure and the modulation doping result in a deflection of the band structure. The conducting band of the GaAs buffer layer lowers under the Fermi level at the boundary of the AlGaAs spacer. The confinement potential formed this way has a nearly triangular shape and is filled with electrons from the Si doped layer. Since the motion the electrons is confined perpendicular to the surface the heterostructure forms a quasi two-dimensional electron system (2DES). The distance of the 2DES to the surface is approximately 90 nm.
A basic parameter concerning transport experiments accomplished with low-dimensional electron systems is the electron mobility, μ. Its value is directly related to the mean free path of the electrons

$$l_{\mathrm{e}} = v_{\mathrm{F}} \cdot \tau = \frac{\hbar k_{\mathrm{F}} \cdot \mu}{e} \quad . \tag{2.1}$$

In this equation v_{F} is the Fermi velocity and $k_{\mathrm{F}} = \sqrt{2\pi \cdot n}$ the Fermi wave vector. At low temperatures the mobility and thus the mean free path is reduced by scattering at ionized impurity traps [12]. The spacer mentioned above has the function to separate the donor traps in the Si-AlGaAs spatially from the quantum well. Due to the spacer the scattering is significantly decreased and an extremely high low-temperature mobility can be reached. Heterostructures with this property are called "high electron mobility transistors" (HEMT). The samples used in this work show a mobility of approximately $\mu = 1\,000\,000\ \frac{\mathrm{cm}^2}{\mathrm{Vs}}$. An average carrier density of $n = 2.2 \cdot 10^{11}$ cm^{-2} results in a mean free path of 7.7 μm. Within this range the motion of the high mobility electrons can be assumed as ballistic.
Magnetic transmission X-ray microscopy is accomplished with thin membrane windows

which consists of silicon nitride (Si_3N_4). To produce the membranes a thin layer of Si_3N_4 is deposited upon a silicon substrate. Thereby, the Si_3N_4 acts as an etch-stop layer. Since the etch rate depends on the crystallographic direction the boundaries of the etched window have a gradually sloping wall [13].
The silicon nitride membrane windows used in this work are produced by Silson Ltd, England[1]. For the membranes a thickness of 200 nm has been chosen and a square window size of 5×5 mm^2. The frame thickness, i.e. silicon substrate inclusive the silicon nitride layer is 200 μm and the frame side length 10 mm (see Fig. 2.1(b)).
Silicon nitride belongs with silicon carbide to the class of non-oxide ceramics. It stands out by the particular combination of its properties like extremely high mechanical strength and toughness. Moreover, silicon nitride features a small heat strain, a medium thermal conductivity and an extremely high chemical resistance. All these characteristics are important since the membrane is caught in various strains during the preparation.
With respect to transmission experiments with soft X-rays the membranes should offer a high penetrability for photons. In fact, silicon nitride shows a suitably low absorption coefficient. The transmitted intensity through the material can be estimated by the absorption law

$$I = I_0 \cdot e^{-\sigma \rho \cdot d} \quad . \tag{2.2}$$

A silicon nitride density[2] of $\rho = 3.23 \, \frac{\mathrm{g}}{\mathrm{cm}^3}$ and a maximum mass absorption coefficient of $\mu = 5 \cdot 10^4 \, \frac{\mathrm{cm}^2}{\mathrm{g}}$ in the photon energy range from 300 eV to 1000 eV [14] leads to a relative transmitted intensity $\frac{I}{I_0} > 97\,\%$.

2.2. Hall bar preparation

The preparation of the Hall bar structure follows various processing steps which begin with the actual Hall bar within the center of the structure. After fabrication of the input leads which establish the connection on the sample between bond pads and Hall crosses the bond pads are further processed to provide ohmic contacts to the 2DES of the GaAs heterostructure. On completion of these steps ferromagnetic or superconducting micro- and nanostructures are deposited on top of the Hall crosses.
For the fabrication several exposure steps with a mask aligner or an electron-beam lithography system are essential in order to define selected areas for a subsequent preparation. Small areas in nanometer-sized range are structured via electron-beam lithography. For this purpose the scanning-electron microscope (SEM) Zeiss DSM 962 is available which is controlled by a computer with the software Raith ELPHY Plus V2.07. Areas which are larger than few micrometers are defined by optical lithography with the mask aligner Karl Suss MJB-3. Here, the exposure can be accomplished considerably faster where the lower resolution of the mask aligner is sufficient.

[1] Webpage: http://www.silson.com/.
[2] Rauschert GmbH, webpage: http://www.rauschert.com/.

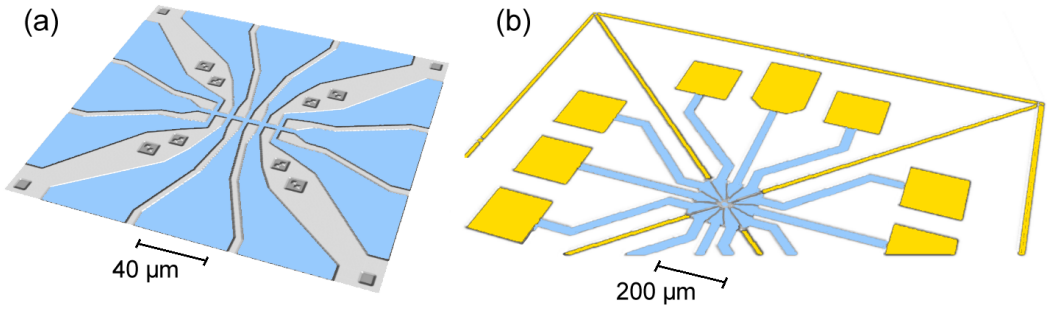

Fig. 2.2.: (a) Center area of the Hall bar structure. The 2DES (blue) is located 90 nm below the surface. The distances between the Hall crosses are 10 μm. (b) Section of the completed Hall bar structure with input leads containing a 2DES (blue) and bond pads made of gold (yellow). The outer alignment structures of gold serve to coarsely adjust a coordinate system for subsequent preparation steps.

The samples which are used to structure the Hall sensors are prepared by breaking the wafers along the [100]- and [010]-direction. They have a squared outline and a side length of 5 mm. The complete Hall bar structure covers an area of 2×2 mm^2 including an outer alignment area of gold, so that four whole structures build a 2×2 array upon a single sample. Due to the redundant preparation a high yield of measurable Hall sensors is guaranteed.
At first, the center area of the Hall bar structure is defined in which the actual Hall sensor is located. In Fig. 2.2(a) the completed processing step is depicted. The detailed parameters of the fabrication sequences which are resumed in the following and a stepwise description of all processing steps can be found in [15].
For electron-beam lithography the sample initially is coated with PMMA 600K resist with a thickness of 500 nm and baked out 60 min at 160 °C. To define all areas which do not belong to the conductive leads of the Hall crosses the resist is exposed within a writefield size of 200×200 μm^2. After developing the sample, traces of the resist might remain in the illuminated areas. These impurities are ashed by an oxygen plasma in a barrel reactor. Finally, the 2DES is removed to a depth of 90 nm by wet etching. Solely the doped layer which is responsible for providing free electrons is eliminated while the channel of the two-dimensional electron system stays intact. This selective etching offers the advantage of reduced interface scattering and a decrease of the depletion region [16]. A distance of 10 μm between the Hall crosses has been chosen, in order to avoid interference effects between adjacent sensors and between micro- and nanostructures on top of the five Hall sensors. The width of the Hall bar is adjusted according to the size of microstructured electrodes in the range of $1.0 - 3.5$ μm.
Analogous to the center area the input leads and bond pads in the exterior area are fabricated by wet etching. Here, like in the Hall bar the 2DES is used as conducting layer. Figure 2.2(b) shows the completion of the Hall bar structure. Since the surface area which has to be etched strongly exceeds the size of the center area, optical lithography is used

for structuring. The appropriate resist Shipley Microposit S1813 is applied via spin coating with the same parameters like PMMA. The exposure of the sample is accomplished with chrome masks which have been produced by electron-beam lithography.
To achieve an electric contact with bond wires between the chip carrier and the 2DES, metal has to be alloyed into the bond pads. The bond pad areas are defined with an optical exposure step and AuGe combined with Ni is deposited upon the sample by means of thermal evaporation. After a lift-off procedure the AuGe/Ni only remains upon the bond pads. Finally, the sample is heated in argon atmosphere up to 400 °C to establish the contacts by alloying.
For completion of the Hall bar structure the bond pads are evaporated using Au. The gold layer guarantees a robust junction of the bond wires upon the pads. In the same evaporation step additional outer alignment structures are deposited on the sample. These structures serve to coarsely adjust a coordinate system for the SEM preparation of the micro- and nanostructures upon the Hall crosses.

2.3. Microstructured ferromagnetic electrodes

The interest in ferromagnetic electrodes is fuelled by their use in magnetoelectronic and spintronic devices. Here, quadratic and rectangular structures in size up to 8 μm and thickness in the region of 30 nm are investigated. Beside isolated electrodes also double electrodes and arrays of quadratic structures have been prepared. In order to study the ferromagnetic electrodes with different magnetic imaging techniques the structures have been deposited upon Hall sensors as well as on membrane windows.
The precision of the shape of the electrodes and the positioning especially upon the Hall sensors plays a decisive role for the magnetization and for the measurement signal. For this reason specific requirements for the preparation and alignment of the electrodes are to be fulfilled. On the one hand, the corners of the rectangular structures should not be rounded. Additionally, the inter-element distances of the double electrodes and the arrays, respectively, should be less than 200 nm. On the other hand, the position of the electrodes upon the Hall crosses determines the signal strength and the gradient of the magnetic stray field which is detected by the 2DES. This specification defines a positioning accuracy of the structures which should be better than 200 nm.
The requirements for the fabrication of micro- and nanostructures are fulfilled by the high resolution provided by electron-beam lithography. Inhomogeneities and roundings are primarily induced by the so-called proximity effect, i. e. an overexposure of the structure's boundaries caused by backscattered electrons. The effect of rounding can be reduced by an additional exposure of the corners.
A precise positioning of the electrodes upon Hall sensors with the scanning-electron microscope is carried out via two different alignment systems. An outer alignment structure of Au serves to adjust the SEM stage with respect to the center position of the Hall structure. An inner system of etched alignment marks (confer Fig. 2.2) is applied to adjust the write field of the SEM to the preprocessed Hall crosses using the lithography software.

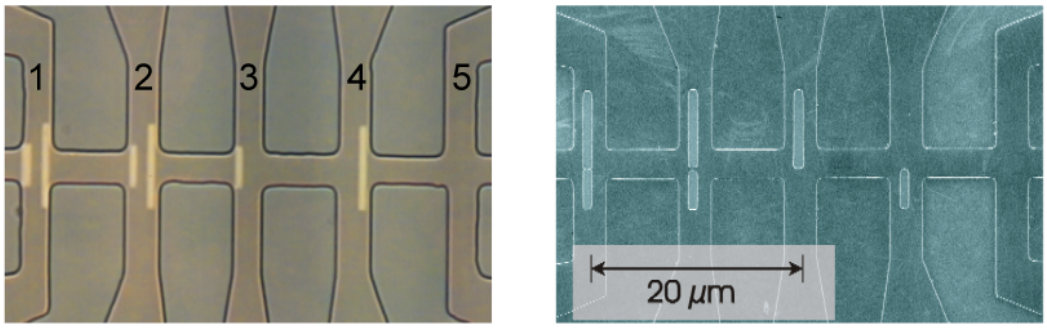

Fig. 2.3.: Hall samples with electrodes made of permalloy (Py). (a) The double electrodes in "spin-valve configuration" are separated 800 nm. (b) The gap of the double electrodes in "spin-FET configuration" has been positioned in the center of the Hall cross.

In Fig. 2.3 two samples with Hall sensors of the same size are shown. On top of the sensors electrodes made of permalloy[3] (Py) are located. The electrodes of both samples have been deposited with a DC sputter process. To investigate the magnetic anisotropy the samples have been mounted peripheral onto the sample holder with a radial orientation of the electrodes. A description of the basics and technical details of sputter processes can be found in [17]. Nominal widths of 3.2 μm have been chosen for both Hall bars in order to fit the Hall crosses to the size of the structures. The fifth Hall cross served as empty reference sensor on all samples.
The double electrodes in Fig. 2.3(a) are arranged in the "spin-valve configuration". The size of the large electrode is 8.0×0.8 μm^2. The small electrode has been prepared with two different widths. Upon sensor one the lateral geometry is 4.0×1.0 μm^2 and upon sensor two and three a size of 4.0×0.8 μm^2 has been chosen. The gaps between the double electrodes have a value of 800 nm and the thickness of the structures is 20 nm.
On top of the second sample the double electrodes are placed in "spin-FET configuration" as depicted in Fig. 2.3(b) with a thickness of 17 nm. The large electrodes have a same lateral geometry as in spin-valve configuration of 8.0×0.8 μm^2. The small electrodes have size of 4.0×0.8 μm^2. For the investigation of the stray field between the double electrodes the gap has been positioned in the center of the Hall cross. The electrodes on top of the first sensor are in slight contact while the electrodes upon sensor two are separated with a distance of 200 nm.
In addition to permalloy as ferromagnetic material iron has been chosen for the investigation with Hall micromagnetometry. Figure 2.4(a) shows an atomic-force microscope (AFM) image of a double electrode made of iron. The other sensors of the Hall bar structure are used for single electrodes. The side length of the iron electrodes are 1×1 μm^2 and 2×1 μm^2 with an inter-element distance of 150 nm. The structures have been de-

[3] Alloy compounded of 80 % Ni and 20 % Fe.

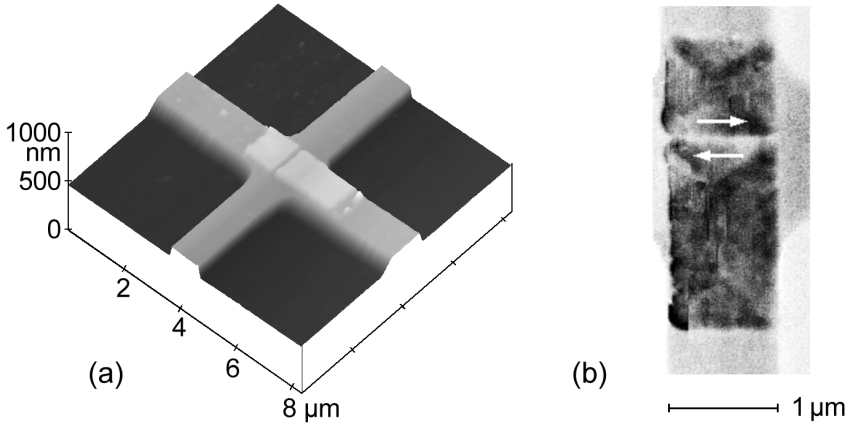

Fig. 2.4.: (a) AFM and (b) MFM image of an iron double electrode on top of a Hall sensor. The size of the electrodes are $1 \times 1\ \mu\text{m}^2$ and $2 \times 1\ \mu\text{m}^2$. The z-axis of the AFM image is enlarged for clarification. The MFM image reveals a magnetization direction of the electrodes at the gap in antiparallel orientation as the arrows indicate.

posited via thermal evaporation with a thickness of 27 nm. The z-axis of the AFM image is enlarged for clarification. In Fig. 2.4(b) a magnetic-force microscope (MFM) image of the same iron double electrode at remanence is depicted. The arrows next to the gap indicates the magnetization direction of the electrodes. The antiparallel orientation of the domains is a required condition for experiments in spin-valve configuration. A detailed description of magnetic-force microscopy can be found in Sec. 2.6.2.

2.4. Preparation of membrane samples

Two sets of microstructured electrodes upon membrane windows have been prepared for magnetic-transmission X-ray microscopy. The first structure series consists of isolated electrodes of different size and additional double electrodes. Membrane windows of the second series contain square lattice arrays of thin microelements with varying inter-element distance.

In Fig. 2.5(a) a section of the CAD designed structure of the first series can be seen. Due to the chessboard-like configuration isolated electrodes with side lengths between 0.5 μm and 4 μm and varying aspect ratios can be treated. The double electrodes have a size of $2 \times 2\ \mu\text{m}^2$ and $4 \times 2\ \mu\text{m}^2$ and separations which range between 100 nm and 600 nm. Via thermal evaporation multiple layers have been deposited within a single process step upon the membrane. The coupled microcontacts consist of 11 nm Al as seed layer, 30 nm Fe as lower and 30 nm Ni as upper ferromagnetic layer. A 6 nm thick Al cap serves as protection.

The square lattice arrays of the second structure series are composed of 5×5 elements with a side length of each $2 \times 2\ \mu\text{m}^2$. The inter-element distance has been varied between

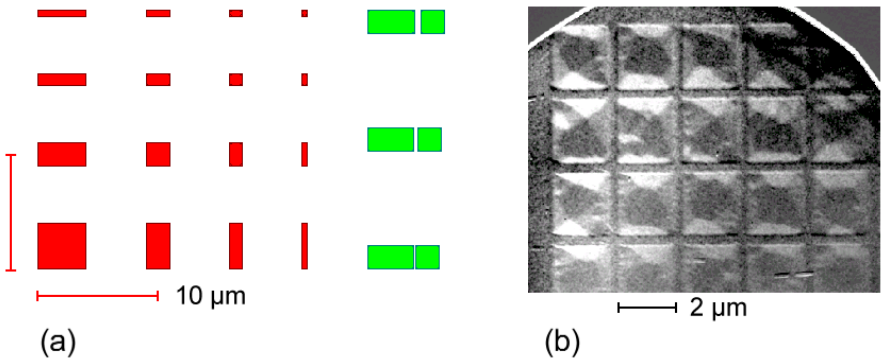

Fig. 2.5.: (a) Section of the designed structure of the first membrane window series used for the exposure with lithography software. (b) MTXM image of an array of Fe microelements separated by 200 nm.

200 nm and 2000 nm in multiple steps. In Fig. 2.5(b) a magnetic transmission X-ray microscope image of an array with 200 nm distance is depicted. Like the first series the elements have been deposited via thermal evaporation. The layer sequence consists of 5 nm Al, 20 nm Fe as ferromagnetic layer and 3 nm thick Al cap as protection.

2.5. Deposition of $CoPt_3$ nanoparticles

Ferromagnetic nanoparticles are promising candidates for various applications which includes ultra-high storage media and medical therapy like drug targeting. They additionally are suitable as biomedical markers for diagnostics. Prominent representatives are FePt and $CoPt_3$ nanoparticles [18, 19]. These materials have a high crystalline anisotropy which is required for a good thermal stability of the magnetization – an important property for storage applications. Typically the particles show a temperature dependent evolution from superparamagnetic behavior at high temperatures to an anisotropic superparamagnetism just above the blocking temperature, and a blocked superparamagnetic behavior at low temperatures [20].
Hall micromagnetometry is suitable to investigate the magnetic properties of such nanoparticles with a high sensitivity and resolution. For this purpose structures are required in the lower nanometer range. The fabrication of ferromagnetic nanostructures with conventional lithography processes is rather complex. Alternatives for preparation of nanoparticles are magnetron sputtering [21] and microemulsion techniques [22].
The ferromagnetic nanocrystals investigated in this work have been produced through organometallic synthetic approaches and are provided by the Institute of Physical Chemistry in Hamburg. They consist of cobalt (Co) and platinum (Pt) and have been synthesized using a solution-phase method. Briefly, the $CoPt_3$ nanocrystals are formed via a modified "polyol" process in a high-boiling-point coordinating solvent [23]. First ferromagnetic nanocrystals prepared by this organometallic route were FePt [24] and

Co [25]. Due to the larger spin-orbit coupling of cobalt, Co-based nanoparticles may be expected to provide a higher anisotropy, even in the as grown state.
As-synthesized $CoPt_3$ nanocrystals represent single domain particles and have a chemically disordered face-centered cubic (fcc) structure. The mean particle size can be varied from 1.5 nm to 7.2 nm by controlling the reaction conditions and the type of coordinating mixture.
In order to obtain a sufficiently large measuring signal a close packed monolayer has been attempted to prepare. Due to the organometallic synthesis a narrow size distribution of nanocrystals and an arrangement in two- and also three-dimensional lattices with controllable inter-particle spacing can be reached.
Figure 2.6 shows SEM images of a Hall sample on which nanometer sized $CoPt_3$ crystals are located. On the left image an overview with two Hall sensors can be seen. The right image is an blow-up of a section at the edge of the Hall bar. On the right side of the edge the mesa of the Hall bar can be seen on which two distinct sizes of particles are located. The particles have been deposited in a monolayer upon the whole sample via a spin coating process. They are self-assembled into a hexagonal lattice in selected areas. The size of the nanoparticles of 3 nm and 6 nm has been determined from SEM images. Countings of the two different particle sizes result in $1.28 \cdot 10^5$ for the 3 nm particles and $2.90 \cdot 10^4$ for the 6 nm particles on top of the 3.2×3.2 μm^2 Hall cross. This is only a small fraction of material required, e. g., for SQUID magnetometry. In principle a further reduction of the sensor size is possible which could enable the measurement of accordingly less $CoPt_3$ particles.

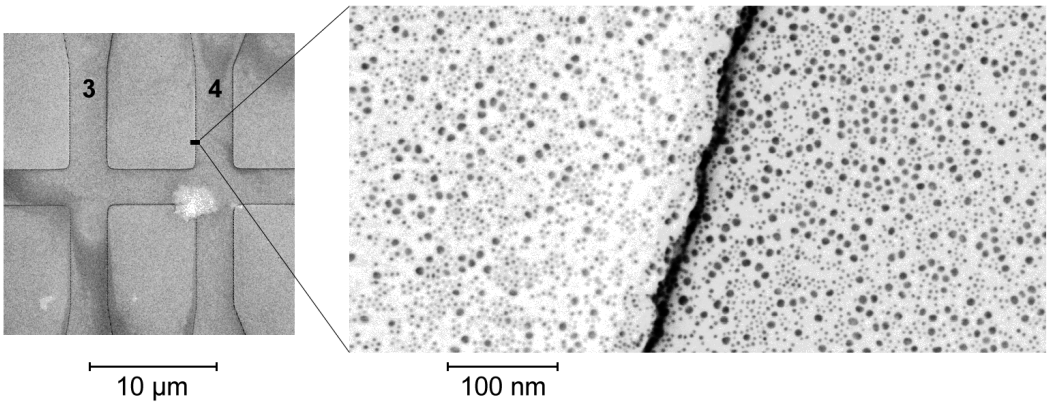

Fig. 2.6.: SEM image of $CoPt_3$ nanoparticles on top of two Hall sensors. The width of the Hall bar is 3.2 μm and the distance between the sensors amounts 10 μm. On top of both sensors the $CoPt_3$ nanoparticles are primarily arranged in a monolayer. Hall sensor four additionally shows a cluster of nanoparticles located in the left bottom area. In the blow-up the right area next to the edge shows a part of the Hall bar. Two different particle sizes of 3 nm and 6 nm can be seen.

2.6. Measurement techniques

Magnetism down to the nanometer scale continues to be the focus of extensive research. It is of fundamental importance in magnetic sensing and information storage. Numerous nanofabrication techniques have been employed and developed to generate a wide variety of magnetic nanostructures. However, only a few micromagnetic techniques are available as highly sensitive and non-invasive measuring methods. One technique that has produced an impressive array of results is the magnetometry with superconducting quantum interference devices (SQUID) of micrometer sizes [26]. Their operation is admittedly limited to low temperatures and small applied fields.
In this work other measurement techniques have been applied to study individual micro- and nanoscale magnetic units as well as double structures and arrays. Hall micromagnetometry, based primarily on two-dimensional electron systems (2DES) in semiconductor heterostructures, suffers almost no restrictions and limitations in temperature range and applied magnetic fields. For practical applications in magnetic recording, field sensing, or biomagnetic detection, high sensitivity techniques at room temperature are necessary. Here, magnetic-force microscopy (MFM) offers spatially-resolved information in applied magnetic fields. Magnetic-transmission X-ray microscopy (MTXM) provides non-invasive measurements and element-specific investigations.

2.6.1. Hall micromagnetometry

Hall magnetometers for ferromagnetic and superconducting materials are becoming increasingly popular since they feature distinct advantages:

a) non-invasive measurements,

b) high magnetic field sensitivity suitable for time- and space-resolved detection of individual vortices in superconductors [27],

c) very small active region [28], i. e. the cross region of the Hall bar is less than a micron wide,

d) sensitivity in a broad temperature and magnetic field region,

e) versatile [29, 30] and comparatively simple setup.

Hall micromagnetometry has been applied for patterned submicron- or nanomagnets [31] and also as scanning magnetic probe [32]. Marked improvement in resolution, especially at high fields, can be realized by using gradiometry to circumvent the difficulty of measuring a tiny signal on top of a much larger background [33].
The signal measured by Hall micromagnetometry depends on the magnetic stray field of the electrodes on top of the Hall sensor. In contrast, e. g., to XMCD the method not directly detects or images the magnetization of the electrodes but measures the Hall response of the 2DES to the small dipole fields originating from the magnetic micro- or

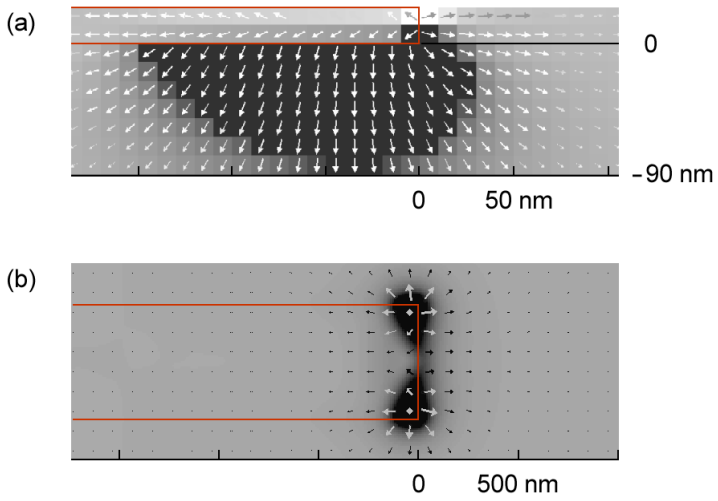

Fig. 2.7.: Simulated magnetic stray field of a 20 nm Permalloy electrode with a size of $3.0 \times 0.6\ \mu\mathrm{m}^2$ located 90 nm above the 2DES. (a) The side view along the border of the electrode illustrates the vertical stray field of the magnetic end domain. (b) The top view demonstrates the horizontal stray field (arrows) and z-component (grey scaling) within the plane of the 2DES. The maximum and minimum local stray field strengths are 32 mT for black and 0 mT for light elements, respectively.

nanostructure. Due to the constricted motion of the electrons within the two-dimensional system exclusively the z-component of the stray field is detected.
In Fig. 2.7 a simulation of the magnetic stray field of a 20 nm thick Permalloy electrode with a size of $3.0 \times 0.6\ \mu\mathrm{m}^2$ located 90 nm above the 2DES is depicted. The magnetic pattern inside and below the electrode is simulated with the computer code OOMMF supplied by Porter and Donahue [34]. For permalloy, a saturation magnetization of $860\,000\ \frac{\mathrm{A}}{\mathrm{m}}$, an exchange constant of $13 \cdot 10^{-12}\ \frac{\mathrm{J}}{\mathrm{m}}$, and a zero anisotropy constant are chosen. The applied grid size of 10 nm is close to the exchange length of Py. The side view in Fig. 2.7(a) illustrates the cross section of the stray field distribution along the border of the electrode. In the area directly below the end of the magnetic domain the stray field predominantly crosses the 2DES in perpendicular direction. With increasing distance to the edge of the electrode the perpendicular component rapidly vanishes. The grey scaling demonstrates the amount of the z-component in the area below the Py structure. In Fig. 2.7(b) the stray field distribution 90 nm below the electrode in the plane of the 2DES is shown in top view. Arrows illustrate the x-y-component and back grey scaling the z-component of the magnetic field. As apparent, the Hall signal is primarily generated by the stray field below the edges of the electrode.
The heterostructures which have been used for fabricating Hall sensors provide two-dimensional electron systems with an extremely high low-temperature mobility (see Sec. 2.1). Due to the large mean free path of the electrons, scattering primarily occurs at the boundaries of the mesoscopic Hall bar. A quantitative theory can be derived to relate

the measured Hall voltage to the local flux through the Hall sensor [35]. The correlation of the Hall effect and the average magnetic field in the cross junction [36] is given by

$$R_{xy} = \frac{U_{\mathrm{H}}}{I_x} = \frac{\langle B_z \rangle}{ne} \quad . \tag{2.3}$$

The averaging $\langle B_z \rangle$ refers to the characteristic area $S \approx (w + 1.4 \cdot r)^2$ of a Hall cross with rounded corners of radius r and width w. The result has been obtained for a square junction with sharp corners in analytical calculations and numerically for rounded corners and rectangular junctions [37, 38]. In addition, Monte Carlo simulations of mesoscopic Hall bars containing a locally inhomogeneous magnetic field demonstrate that in the regime of low magnetic fields the Hall resistance is independent of the shape and position of the profile [39]. The measured signal as well as the average magnetic field

$$\langle B_z \rangle = \frac{1}{S} \int_S B_z(x,y) \, \mathrm{d}x \, \mathrm{d}y = \frac{\Phi}{S} \tag{2.4}$$

is rather determined by the flux Φ through the characteristic area of the Hall cross. As obvious, a ballistic Hall probe works exactly as a micro-fluxmeter. The sensor area in particular can reach dimensions of less than 0.1 $\mu\mathrm{m}^2$. Diffusive transport applies for larger Hall crosses and for higher temperatures [40].
Without an external magnetic field ($B_{\mathrm{ext}} = 0$) the ballistic electrons are solely deflected by the stray field of the electrodes on top of the Hall sensor. To investigate the structures not only at remanence an external field is applied in varying directions to the surface of the Hall sensor. In order to study the magnetic signal of the electrodes the external magnetic field has to be separated from the measured Hall voltage. Therefore, the empty reference Hall sensor is employed

$$M_{\mathrm{B}} = \frac{ne}{\mu_0 I} \left(U_{\mathrm{Mag}} - U_{\mathrm{Ref}} \right) \quad . \tag{2.5}$$

However, the calculated magnetization M_{B} of the electrode's stray field cannot directly be associated with the magnetization M. The Hall response is rather an image of the local magnetization of that part of the electrode which is located within the sensor area. The measured Hall signal which is generated by nanoparticles on top of the sensors also cannot quantitatively be evaluated. Since the total stray field is composed in a complex way by the contributions of all particles no conclusion can be drawn on the magnetization of a single nanoparticle.

2.6.2. Magnetic-force microscopy

Especially for magnetic information technology interest focuses on observing the domain distributions of magnetic structures at sub-micrometer scale. Here, magnetic-force microscopy [41] combines spatially-resolved information acquisition with the performance of room temperature measurements in external magnetic fields. Important advantages are a comparatively simple and efficient set-up and a minimum of requirements concerning

the preparation of the samples. On the other hand, magnetic-force microscopy is a rather slow measurement technique and shows indications of invasive nature on the magnetic states.

Magnetic-force microscopy is an extension of atomic-force microscopy (AFM) [42]. In contrast to AFM the probe is sensitive to magnetic stray fields. For this purpose microtips coated with magnetic films are applied. The tip can be thought as a magnetic dipole [43] inside the tip volume. In the present mode of operation [44] with the used system Digital Instruments Nanoscope SPM the magnetic tip is driven twice in same line scan across the sample surface. Within the first scan the topography of the surface is probed similar to the AFM mode. The second scan is carried out in Lift Mode 50 – 100 nm above the surface. In this distance only the long-range magnetic force from the stray field $\vec{H}$ of the ferromagnetic sample is effective. This force acting on the magnetic tip is equal to the negative gradient of the corresponding Zeeman energy

$$\vec{F} = -\nabla E_H = \int_{V_{\mathrm{Tip}}} \nabla \left(\vec{M}\vec{H} \right) \mathrm{d}V = \nabla \left(\vec{m}\vec{H} \right) \quad . \tag{2.6}$$

Here, the magnetic dipole $\vec{m} = \int \vec{M}\,\mathrm{d}V$ represents the magnetization of the tip whose orientation further on is assumed to point perpendicular to the sample surface ($m_x = m_y = 0$, $m_z \neq 0$). Accordingly the force result in

$$\vec{F} = \left(m_z \frac{\partial H_z}{\partial x},\ m_z \frac{\partial H_z}{\partial y},\ m_z \frac{\partial H_z}{\partial z} \right) \quad . \tag{2.7}$$

For laterally extended structures the approximation $\frac{\partial H_z}{\partial x}, \frac{\partial H_z}{\partial y} \ll \frac{\partial H_z}{\partial z}$ can be utilized.

The signal measured by MFM corresponds to the phase shift $\Delta\Phi$ of the cantilever oscillating close to its resonance frequency at about 60 – 70 kHz [45]. Since the phase shift is proportional to the gradient of the magnetic force the MFM signal can be identified as second derivative of the stray field's z-component

$$\Delta\Phi(x,y) \propto \nabla\vec{F} \approx \frac{\partial F_z}{\partial z} = m_z \frac{\partial^2 H_z}{\partial z^2} \quad . \tag{2.8}$$

Usually, a grey scales image indicates the magnetization direction of the probed magnetic sample. Black and white pixels of the image are interpreted as areas of low and high magnetic stray field in z-direction.

The magnetic-force microscope used in this work is equipped with an Helmholtz coil. It provides external magnetic fields up to ± 100 mT. The tip magnetization generally is not influenced by this field since hard magnetic materials are used for tips. The resolution of the MFM depends on the radius of the magnetic tip as well as on the tip-sample distance and ranges between 10 nm and 100 nm [46].

For comparison of measured MFM images with simulated magnetization patterns MFM images can be calculated according to Eq. (2.8) [47]. In order to compute the overall stray field the simulated structure is interpreted as an array of magnetic dipoles. Here, the approximation for laterally extended structures is not needed and the full set of derivatives

can be included. This can be important in regions of strongly inhomogeneous stray fields at edges or domains walls. A proper consideration of edges is particularly relevant for the calculation of stray fields in hybrid devices.
The combination of MFM and micromagnetic simulations has proven to be a powerful tool to determine the magnetization of micro- and nanostructured ferromagnets. The direct comparison of the stray field images is provided by add-ons to OOMMF and enables to analyze the consistence between experiment and simulation.

2.6.3. Magnetic transmission X-ray microscopy

A novel technique to image element specifically magnetic domain structures is magnetic transmission X-ray microscopy (MTXM). It combines X-ray magnetic circular dichroism (XMCD) with a high resolution transmission X-ray microscopy [48]. The high lateral resolution down to 20 nm is achieved by Fresnel zone plates [49]. The magnetic contrast with values up to 50 % can be obtained at the $L_{2,3}$ edges in transition metals like Fe, Co or Ni. In detail, the absorption of circularly polarized X-rays depends on the projection of the magnetization onto the photon propagation direction and serves as a contrast mechanism [50]. The first set-up was demonstrated at the synchrotron facility BESSY I in Berlin [51]. The results used in this work have been recorded at the soft X-ray microscope XM-1 at the Advanced Light Source (ALS) in Berkeley, CA.
A unique feature of magnetic transmission X-ray microscopy is the inherent chemical specificity, i. e. the MTXM contrast is a measure of the elemental magnetization. This characteristic reveals that MTXM particularly is suitable to investigate multilayer systems and stray field coupled microcontacts. Additionally, due to the non-invasive photon based technique, the images can principally be recorded in unlimited external magnetic fields. Thus, MTXM allows for detailed studies of magnetization reversal processes. However, the penetration depth of soft X-rays sets sample thickness limits to about 100 – 200 nm for the soft X-ray regime below 1 keV. Moreover, X-ray transparent substrates for sample preparation are required (compare Sec. 2.1).
The MTXM signal corresponds to the scalar product of the transmitting X-ray beam with the magnetization of a ferromagnet. To study in-plane magnetization, the sample has to be tilted with respect to the beam direction [52]. The MTXM images taken at the Fe L_3 absorption edge at a photon energy of 706 eV exhibit a contrast reversal from dark to light when the external field is reversed. Areas of homogeneous gray shades (see Fig. 2.5(b)) display regions of a ferromagnetic structure having the same magnetization, i. e. domains. With a proper normalization of the images to the saturated image MTXM can be used as a highly sensitive local magnetometer. To achieve this, the mean value of the grey scale data in the magnetic part of an image is offset by the mean value of the non-magnetic neighborhood and normalized with it. By this method possible spatial fluctuations of the synchrotron light intensity are significantly reduced and hysteresis loops of a single microelement can be measured. Magnetic moments down to $1 \cdot 10^{-13}$ Am$^2 = 0.1$ nemu can be resolved which illustrates the ultra-high sensitivity.

MTXM is an excellent tool to investigate the fragile and complex dipolar magnetic interaction in arrays of micro- and nanostructured elements. It allows non-invasive exploration of magnetic reversals within large arrays due to the full-field scope with a high spatial resolution [53, 54]. In this work MTXM is used in external magnetic fields of up to ± 100 mT.

3. Ferromagnetic microstructures

This chapter deals with the investigation of microstructured thin-film elements made of ferromagnetic materials. First a short introduction to the theory of magnetism and especially to the concept of the micromagnetic model is given. In the following, experimental results of ferromagnetic microstructures are presented which are obtained by Hall micromagnetometry, magnetic transmission x-ray microscopy, and magnetic-force microscopy.

3.1. Theoretical background

3.1.1. Introduction to Ferromagnetism

In vacuum a direct proportion exists between an external magnetic field, H, and the magnetic induction, B, whereas the correlation is modified in the presence of material. From experiment it is known that every material acquires a magnetic moment in external fields. The influence on the magnetic induction can be taken into account multiplicatively by the relative permeability, μ_r, or additively by the magnetization[1], M

$$\vec{B} = \mu_0 \left(\vec{H} + \vec{M}\right) = \mu_0 \vec{H}\,(1+\chi) = \mu_0\,\mu_\mathrm{r}\vec{H} \quad . \tag{3.1}$$

The relation of the magnetization which is defined as the magnetic moment per unit volume $\vec{M} = \sum \vec{m}_i$ and the magnetic field $\vec{H}$ is written as

$$\vec{M} = \chi \cdot \vec{H} \quad , \tag{3.2}$$

where $\chi = \mu_r - 1$ is dimensionless and called the magnetic susceptibility [55]. In the case of weakly magnetic materials, μ_r and χ are normally field-independent. Substances with a negative magnetic susceptibility $\chi < 0$ are classified as "diamagnetic" while material with a positive magnetic susceptibility $\chi > 0$ are called "paramagnetic". These properties can be comprehended by the free atom's magnetic moment.
Diamagnetism solely occurs in materials containing no atomic magnetic moment. The negative susceptibility is induced by the change of the Bohr orbital moment of an electron in an applied magnetic field. According to Lenz's Law, the magnetic flux produced by an orbital electron is always opposite to the one of the external field.
Paramagnetism is found in materials that contain widely separated atoms or ions. Each of them has a fixed magnetic moment $\vec{m}$ which is given by

$$\vec{m} = g\,\frac{\mu_\mathrm{B}}{\hbar} \cdot \vec{J} \quad , \tag{3.3}$$

[1] SI units are used throughout this work (confer DIN 1325 and DIN 1339).

where the total angular momentum $\vec{J}$ is the sum of the orbital $\vec{L}$ and spin $\vec{S}$ angular moments [56], $\mu_B = \frac{e\hbar}{2m}$ the Bohr magneton. The quantity g is the Landé factor. Thus, gyromagnetic experiments give information about the ratio of orbital and spin angular moments to the total magnetization of the paramagnetic material.
In ferromagnetic materials the relative permeability μ_r is comparatively large (ranging from 10^2 to 10^6) and typically depends non-linearly on the field $\vec{H}$. In this case the magnetization is a complex function of $\vec{H}$ and Eq. 3.1 holds only approximately in a limited range of fields. A complete correlation depends on the history of the applied magnetic field and can be described by a magnetization curve (confer Sec. 3.1.3). In non-cubic crystal groups μ_r and χ additionally correspond to tensors of rank two.
The strong magnetization of ferromagnetic materials particularly in the absence of an external magnetic field cannot be attributed to classical magnetostatic. For production of a spontaneous magnetization the dipole interaction between neighboring atoms is too small. However, according to Weiss an effective field called molecular field [57] can be considered to cause the spontaneous magnetizations. The physical origin is due to quantum mechanical effects which result from Pauli's exclusion principle as first proposed by Heisenberg [58]. Between neighboring atoms with spin $\vec{S}_i$ and $\vec{S}_j$ an exchange interaction is suggested with the Hamiltonian

$$H_{ex} = -2 \sum_{i<j} J_{ij}\, \vec{S}_i \cdot \vec{S}_j \quad , \tag{3.4}$$

where J_{ij} is the exchange integral. The magnitude of J_{ij} is approximately 10^3 times larger than the dipole interaction [59]. If the exchange integral is positive ($J_{ij} > 0$), the energy is lowest when $\vec{S}_i \parallel \vec{S}_j$, so that a ferromagnetic alignment is stable, while for a negative exchange integral ($J_{ij} < 0$) an antiferromagnetic alignment results. The model of localized electrons is valid for many ferromagnetic metals and alloys as well as for metal oxides like Fe_2O_3 and MnO.
For the ferromagnetic 3*d* transition metals Fe, Co, and Ni the calculation of the exchange energy proves to be extremely difficult. The carriers of the magnetism, the 3*d* electrons, are located relatively far from the atomic core. They are considered to be moving among the atoms rather than localized at individual atoms. Thus, a simple approach of a 3*d* electron wave function is not possible. The direct *d*-*d* exchange of localized moments cannot be utilized and the spontaneous magnetization is described by means of a band structure with 3*d* and 4*s* electrons [11].
The exchange energy in the ferromagnetic 3*d* materials, i. e., the spin coupling between the incomplete *d* shells and the 4*s* conduction electrons leads to a redistribution of the electronic states. The exchange coupling causes a shift between the two *d* spin bands partially overlapped by the s bands. Thereby electrons from one spin band are transferred to the other by reversing their spins and bringing their Fermi level to a common value. Despite the increase of kinetic energy due to the occupation of higher energy levels the total energy within the 3d transition metals Fe, Co, and Ni decreases and a ferromagnetic alignment of *d* spins is observed [60]. However, most of the metals are paramagnetic

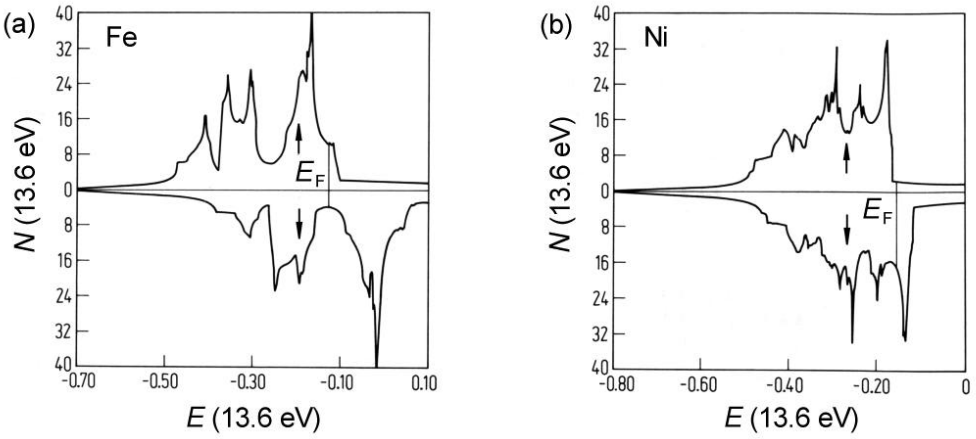

Fig. 3.1.: Electronic density of states $N_E(E)$ of d and s electrons in ferromagnetic materials [61]. (a) The two spin sub-bands of Fe are shifted 2.4 eV to each other due to the exchange coupling. (b) The (↑)-sub-band of Ni is located below the Fermi level.

since the kinetic energy which has to be expended for arranged spin orientation is too high.
In Fig. 3.1(a) the density of states of s and d electrons for both spin bands of Fe is depicted. The calculations are based on parameter-free density-functional theory [61]. The intense structured area within the density of states primarily corresponds to the d electrons whereas the broad region at the upper and lower band edge belongs to the s electrons. The shift of the two spin sub-bands of 2.4 eV due to the exchange coupling leads to a different number of spin states at the Fermi level. In the case of Ni the two spin sub-bands are less shifted by 1.0 eV as shown in Fig. 3.1(b). In contrast to Fe the (↑)-sub-band is located below the Fermi level.
In the discussion of hybrid devices the degree of spin polarization at the Fermi energy E_F is a crucial parameter of ferromagnetic materials. Note that only electrons in the energy range $\Delta E \approx \pm k_\mathrm{B} T$ around E_F contribute to the conductivity. The degree of spin polarization can be defined in several different ways [62]. For transport experiments in the ballistic regime an appropriate description is obtained with the Fermi velocities v_F

$$P_{Nv} = \frac{\langle N v_\mathrm{F} \rangle_\downarrow - \langle N v_\mathrm{F} \rangle_\uparrow}{\langle N v_\mathrm{F} \rangle_\downarrow + \langle N v_\mathrm{F} \rangle_\uparrow} \quad . \tag{3.5}$$

The brackets denote suitable averages over the Fermi surface.

3.1.2. Micromagnetic equations

The transition of a microscopic quantum theoretical description of ferromagnetic materials to macroscopic magnetization properties is obtained by the continuum theory. This so-called micromagnetic theory of ferromagnetism published by Brown [63, 64] provides a description of inhomogeneous magnetization patterns in consideration of the inter-atomic

exchange coupling. Calculations of domain structures, spin distributions, in domain walls as well as the interpretation of the characteristic parameters of hysteresis loops are possible. In order to determine the local direction of the spontaneous magnetization, $\vec{M}_S$, in dependence on time and external magnetic field the magnetic Gibbs free energy

$$G = F - \mu_0 \int \vec{M}_S \cdot \vec{H}_{ext} \, dV \tag{3.6}$$

has to be minimized. The last term in Eq. 3.6 is known as the Zeeman energy. It is the magnetostatic energy of $\vec{M}_S$ in an external magnetic field $\vec{H}_{ext}$. The first term, F, consists of diverse energy contributions and overall represents the free energy

$$F = \int (F_{ex} + F_S + F_K + F_0) \, dV \quad , \tag{3.7}$$

which is equivalent, at $T = 0$, to the internal energy. The exchange energy, F_{ex}, is responsible for an arranged spin orientation of localized and quasi-free electrons [**?**]. A characteristic property of ferromagnetic materials is their magnetostatic stray field. The total stray field energy is given by

$$F_S = -\frac{1}{2} \mu_0 \int \vec{M}_S \cdot \vec{H}_S \, dV \quad . \tag{3.8}$$

The dependence of the internal energy on the direction of spontaneous magnetization is described by the magnetic anisotropy energy, F_K. A rotation of the spin direction relative to the crystal axes changes the exchange energy. The simplest case is the uniaxial magnetic anisotropy which can be found in hexagonal cobalt

$$F_K = K_1 \sin^2 \theta + K_2 \sin^4 \theta \quad , \tag{3.9}$$

where θ is the angle between the magnetization and the hexagonal axis. According to the specific point group the expressions for the local anisotropy in case of cubic and tetragonal symmetries can be derived. Further energy contributions like the magnetoelastic energy, F_M, considering magnetostrictive deformation are combined in F_0 which can be neglected in many cases.

For the calculation of magnetic ground states and quasi static magnetization processes Gibbs free energy has to be minimized. Another approach to determine the magnetic domain configurations of thin microstructured elements is the treatment of a torque $\vec{L}$ on the magnetization

$$\vec{L} = \frac{d\vec{P}}{dt} = \mu_0 \left[\vec{M}_S \times \vec{H}_{eff} \right] \quad . \tag{3.10}$$

Here, $\vec{H}_{eff}$ corresponds to an effective field composed of the external field and contributions of exchange, anisotropy, dipolar and magnetoelastic energies. Generally the effective field can be written as

$$\vec{H}_{eff} = -\frac{dG}{\mu_0 \, d\vec{M}_S} \quad . \tag{3.11}$$

A static micromagnetic equilibrium is achieved by the condition of a vanishing torque $\vec{L} = 0$, i. e., a parallel orientation of effective field and spontaneous magnetization [66, 67]. When deviating from the magnetic ground state the spin system has a dynamic character and is described by a time-dependent magnetization. In this case the magnetization performs an undamped precession in a magnetic field. Since a damping term cannot be derived theoretically from basic principles Landau and Lifshitz added a phenomenological term [**?**]. An alternative equation which has been proposed by Gilbert [68] leads to the combined form

$$\frac{\mathrm{d}\vec{M}_\mathrm{S}}{\mathrm{d}t} = \frac{\gamma_0}{1+\alpha_\mathrm{G}^2}\left[\vec{M}_\mathrm{S}\times\vec{H}_\mathrm{eff}\right] - \frac{\alpha_\mathrm{G}\,\gamma_0}{\left(1+\alpha_\mathrm{G}^2\right)M_\mathrm{S}}\left[\vec{M}_\mathrm{S}\times\left[\vec{M}_\mathrm{S}\times\vec{H}_\mathrm{eff}\right]\right] \quad , \tag{3.12}$$

which is denoted as Gilbert form of the Landau-Lifshitz equation. The first term on the right side describes a homogeneous precessional rotation of $\vec{M}_\mathrm{S}$. Here $\gamma_0 = -\frac{e\cdot g}{2m_\mathrm{e}}$ is the gyromagnetic ratio. The second term determines the damping process where α_G is the damping parameter.
With respect to the experiments performed in the framework of this thesis the static micromagnetic properties are important. However, the observed static magnetization is the result of a dynamic damping process, e. g., after switching the local magnetization vector. For microstructures of iron, nickel, cobalt, and permalloy analyzed here the micromagnetic simulations with the OOMMF code showed the same static magnetization states either by minimizing the Gibbs free energy or by solving the Gilbert equation numerically.

3.1.3. Domain configurations and domain walls

A uniformly magnetized configuration is exceedingly uneconomic in a ferromagnet of finite size. The so-called single-domain magnetization produces a high magnetic stray field energy F_S. In order to reduce F_S the spin distribution within the confined structure has to be altered. The deviation from the complete parallel spin alignment results in an increase of the exchange energy, F_ex, and magnetic anisotropy energy, F_K, in the first instance. A further reduction of the stray field energy is reached by dividing the ferromagnetic structure into multiple domains, in which the spontaneous magnetizations take different orientations. However, with growing number of domains the domain walls which separate the neighboring areas increasingly store domain wall energy. As mentioned above the stable equilibrium state finally is characterized by the minimum of the total free energy, G.
In Fig. 3.2 an example is depicted which illustrates the reduction of the stray field energy of a ferromagnetic disc of radius r and thickness d. In case of a uniformly magnetized configuration free magnetic poles N and S at the edges are present (see Fig. 3.2(a)). The free poles produce a demagnetization field, $\frac{NM_\mathrm{S}}{\mu_0}$, which appears opposite to the spontaneous magnetization, M_S, with a stray field energy given by

$$F_\mathrm{S} = \frac{1}{2\,\mu_0} N M_\mathrm{S}^2 \cdot V \quad , \tag{3.13}$$

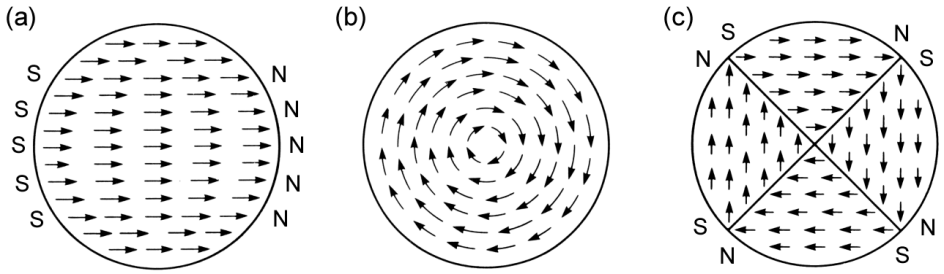

Fig. 3.2.: (a) Uniformly magnetized disc with magnetic free poles N and S in a single-domain state. (b) Circular configuration with vanishing stray field energy. (c) Domain structure caused by magnetocrystalline anisotropy [59].

where $V = \pi r^2 \cdot d$ is the volume of the disc. The demagnetization factor N depends only on the shape of the specimen and can be approximated by a thin oblate spheroid with a demagnetization factor $N = \frac{1}{3}$ [59]. To reduce the free magnetic poles and thus stray field energy one possible arrangement of spins is the circular configuration shown in Fig. 3.2(b). In this configuration no divergence of magnetization appears and the stray field energy vanishes completely ($F_S = 0$). Since the angle between neighboring spins has a finite value the exchange energy is increased in comparison to a parallel alignment. In Fig. 3.2(c) the disc consists of a ferromagnetic material with a cubic magnetocrystalline anisotropy. In this case the spins within the crystal are forced to align parallel to one of the easy axes. The domain structure is similar to the circular configuration in which the stray field energy is reduced by closed lines of the magnetic field. However, the remaining free magnetic poles at the edges of the domain walls still store some stray field energy. In addition, concerning the domain walls various energy contributions have to be considered. There are treated in the following.

For a quantitative understanding of domain patterns the spin arrangement and the magnetic parameters of domain walls have to be investigated. The change of the magnetization from one domain to the other is not abrupt. The exchange energy of spin pairs increases as the square of the angle φ which is between neighboring spins and thus causes strong forces for large angles. But, since the force is only short-ranged small angles over a distance of many atoms do not involve a large exchange energy. Therefore a domain wall consists of a number of transition layers in which the direction of the magnetization changes gradually. Due to the rotating spin orientation anisotropy energy additionally increases within the domain wall. In ferromagnets with magnetocrystalline anisotropy the spins in the wall have to turn away from an easy direction. The number of transition layers finally is determined by minimizing the sum of all energy contributions.

In thick ferromagnetic samples most commonly Bloch walls occur, called after F. Bloch [69] who first investigated the spin structure of transition layers in detail. In Bloch walls the azimuthal rotation angle, $\varphi(z)$, of the magnetization depends only on the z-coordinate, which is taken perpendicular to the domain wall. Thus, the normal component of the

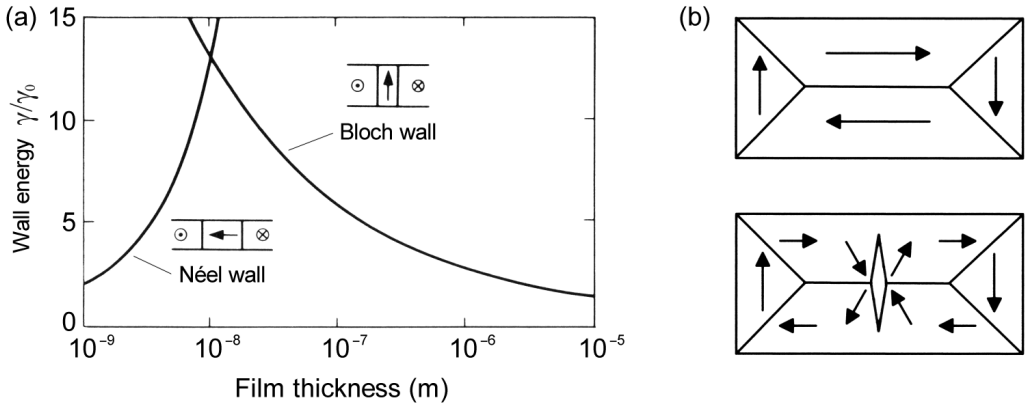

Fig. 3.3.: (a) Normalized wall energy as a function of film thickness for Bloch walls and Néel walls [59]. (b) Landau pattern with a closed domain structure and a 180° Néel wall (top) and a 180° cross-tie wall (bottom) [71].

magnetization is continuous across a domain wall, which results in vanishing magnetic volume charges in the case of planar walls. The thickness of a Bloch wall is obtained to

$$\delta_{\mathrm{B}} = \pi \sqrt{\frac{JS^2}{K_{\mathrm{u}}\, a}} \quad , \tag{3.14}$$

where a is the lattice constant and K_{u} the uniaxial anisotropy constant [59]. The production of magnetic free poles of Bloch walls on the sample surface has little effect in thick samples. In the case of very thin films Néel suggested a rotation of the spins in a plane parallel to the film surface [70]. Changes of the direction of M_{S} in-plane are connected with magnetic stray fields due to magnetic volume charges $\rho = -\mathrm{div}\, M_{\mathrm{S}}$. Since in thin films the stray field energy of surface charges becomes larger than that of volume charges, the Néel walls become stable in thin films.

The transition from Bloch walls to Néel walls in thin films is not clearly defined and has been investigated in several publications [72, 73, 74]. Information about the preference of one wall type can be found from the wall energy which essentially contributes to the formation of domain structures. In Fig. 3.3(a) the normalized wall energy, $\frac{\gamma}{\gamma_0}$, is plotted as a function of film thickness for both wall types. Due to free poles at the film surface in Bloch walls the magnetostatic energy increases with a decrease of film thickness. On the other hand, the magnetostatic Néel wall energy is reduced by a decrease of the film thickness. This is due to the demagnetization factor, N, which becomes smaller with decreasing film thickness.

In the region of intermediate film thickness, where the energies of both domain wall types are comparable, a third type of wall is observed. This cross-tie wall consists of alternative Bloch-type and Néel-type spin configurations along the domain boundary [75]. On both sides of the wall the spin direction changes discontinuously. In Fig. 3.3(b) the transition between a Néel-type wall and a cross-tie wall is depicted. The upper element shows a

Landau pattern with a 180° Néel wall and a closed domain structure which minimize the stray field energy. In the lower domain structure the symmetric 180° Néel wall is decomposed into a special arrangement of 90° Néel walls. The so-called 180° cross-tie wall is characterized by surface free poles which appear as bright or dark spots in images of the stray field.

3.2. Hall micromagnetometry of electrodes for spintronic devices

Semiconductor based spintronics is an active field of research [76, 77, 78]. The idea of a spintransistor [79] has created a new branch of research in solid state physics, combining semiconductors with ferromagnetic metals or utilizing ferromagnetic semiconductors in all-semiconductor devices [80]. Currently, the injection, transport, and detection of spin-polarized electrons in semiconductors are investigated. On the way to a possible spintransistor and other devices using the electron spin in semiconductors a multitude of issues must be addressed. First of all, the injection of spin-polarized charge carriers from a ferromagnet into a semiconductor has to be demonstrated. This problem has been discussed controversially in the last few years but now a consensus on the basic principles has been reached, at least for the limiting cases of diffusive and ballistic transport in the semiconductor.
Here we focus on Hall micromagnetometry of the ferromagnetic electrodes. Ferromagnetic electrodes play an important role in the context of spin injection independent of the specific type of material which could be a ferromagnetic semiconductor [80], a conventional ferromagnetic transition metal, or a half-metallic magnet [81, 82]. Beside the high quality of the interface a defined magnetization direction is an decisive requirement. In a simple approach this requirement could be met by a single-domain contact, in which nearly all microscopic magnetic moments are parallel.
The two limiting magnetization configurations for ferromagnetic in-plane source and drain contacts are depicted in Fig. 3.4. In the spin-valve configuration the magnetic mo-

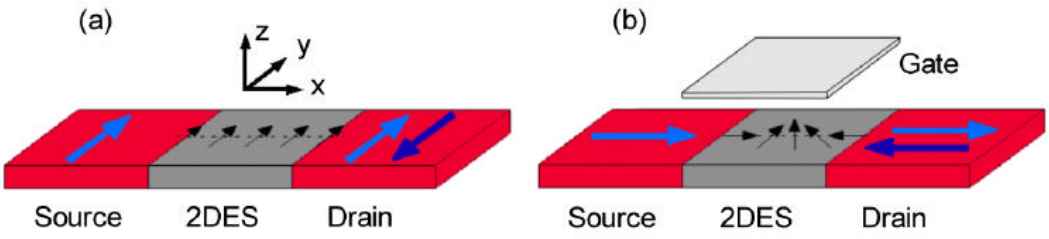

Fig. 3.4.: Sketch of a hybrid device with a two-dimensional electron system (2DES) between two ferromagnetic contacts (source, drain) in (a) spin-valve configuration and (b) spin-FET configuration.

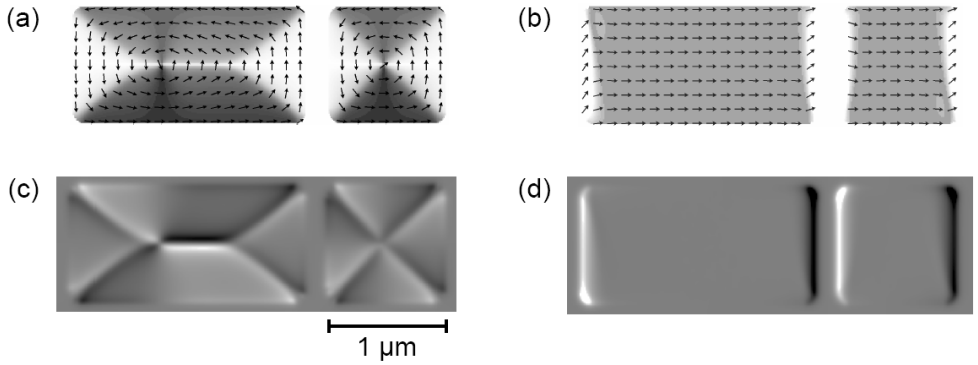

Fig. 3.5.: Simulated magnetization of Py contacts at (a) $B = 0$ and (b) next to saturation. The thickness of the electrodes is 20 nm and the size 2×1 μm^2 and 1×1 μm^2. A saturation magnetization $M_S = 800$ $\frac{\text{kA}}{\text{m}}$, an exchange constant $A = 13 \cdot 10^{-12}$ $\frac{\text{J}}{\text{m}}$, and an anisotropy constant $K_1 = 500$ $\frac{\text{J}}{\text{m}^3}$ are used. In (c) and (d) simulated MFM images are shown. The grey scales comprise 0.04 $\frac{\text{mT}}{\text{nm}^2}$ and 0.16 $\frac{\text{mT}}{\text{nm}^2}$ between black and white, respectively.

ments and spins in the ferromagnet are aligned parallel to the ferromagnet-semiconductor interface. In a ballistic model the spin is then conserved within 2DES [83]. In the spin-transistor case the magnetic moments and spins point in the direction perpendicular to the interfaces. Then the injected spin is not a constant of motion in the channel. It can be shown that the optimal coupling to the spin-precession state is given for normally injected modes, i. e. for modes injected perpendicularly to the interface [83]. From the micromagnetic point of view the spin-valve configuration implies no difficulties. Given the micromagnetic energy contributions in ferromagnets, namely crystalline and shape anisotropy, the micromagnetic behavior can be tailored to obtain parallel or antiparallel magnetization configurations of two neighboring end domains in the hybrid device. However, in single-domain configuration a problem arises from an additional effect in the semiconductor caused by the strong stray field of the end domains. The so-called local Hall effect [84] complicates the measurement of small effects due to spin-polarized injection or makes an identification even impossible. A solution to this problem may be provided by electrodes with a tailored multi-domain structure as shown in the micromagnetic simulation in Fig. 3.5. Such electrodes should combine a high degree of polarization of the injected charge carriers with a small stray field. We have shown that this aim can be achieved using only one domain of a four-domain electrode exhibiting a Landau magnetization pattern at remanence [85].
The following journal articles deal with the experimental, quantitative determination of stray fields by means of Hall micromagnetometry as well as the imaging of magnetization patterns of various ferromagnetic structures with MFM and MTXM techniques.

Publication 1

J. Appl. Phys. **92**, 7296 (2002)

JOURNAL OF APPLIED PHYSICS VOLUME 92, NUMBER 12 15 DECEMBER 2002

Hall micromagnetometry on iron electrodes suitable for spin-polarized transport

G. Meier,[a] R. Eiselt, and M. Halverscheid
Institut für Angewandte Physik and Zentrum für Mikrostrukturforschung, Universität Hamburg, Jungiusstrasse 11, D-20355 Hamburg, Germany

(Received 19 April 2002; accepted 17 September 2002)

Iron electrodes suitable as injectors and detectors for spin-polarized transport in ferromagnet/semiconductor hybrid devices are investigated by Hall micromagnetometry. The Hall effect generated by the stray field of the iron structures is measured for single electrodes and electrode pairs with the external magnetic field aligned in plane either parallel or perpendicular to their easy axes. The strength of the stray field of the double structure in the sensor area is comparable for both configurations. © *2002 American Institute of Physics.* [DOI: 10.1063/1.1519939]

I. INTRODUCTION

Spin injection at room temperature is a key issue for spintronic devices based on semiconductors.[1,2] In this regard iron as a spin injector has attracted a lot of interest theoretically as well as experimentally. From the theoretical point of view it is interesting because of its band structure and concomitant distinct group velocities for spin-up and spin-down subbands at the Fermi energy[3,4] and because of the symmetries of the Bloch part of the wave functions.[5] Experimentally it has been shown recently by optical means that an iron layer can inject a spin-polarized current into a GaAs quantum well through a Schottky barrier with a spin-injection efficiency of about 2%.[6] This proof of principle strengthens the case that iron is a good candidate as an electrode material in room temperature spintronics. In-plane magnetization has been proposed for real spintronic device applications where the magnetic hysteresis behavior can be utilized to sustain spin injection without any external magnetic field.[6] In a spin-transistor device like that proposed by Datta and Das[7] two limiting magnetization geometries are possible, and they have been introduced as spin-valve geometry and spin-transistor geometry.[4] In the former the magnetizations of the electrodes are aligned parallel to each other, whereas in the latter case they are collinear.

In this work we present results of Hall micromagnetometry on individual micrometer-sized iron electrodes with in-plane magnetizations suitable for spin-polarized transport. Structures of similar geometry made of permalloy ($Ni_{80}Fe_{20}$) have been investigated previously by magnetic-force microscopy (MFM) at remanence as well as by micromagnetic simulations in externally applied magnetic fields.[8,9] Electrodes of this geometry have also been used for transport measurements in ferromagnet/InAs hybrid transistors.[10] In these experiments the field effect was examined as a function of the gate voltage in external magnetic fields whereby the observed resistance has indicated spin-polarized transport via an oscillatory gate–voltage dependence of resistance jumps when the magnetization of the ferromagnetic electrodes reverses. However, spin-polarized transport in ballistic hybrid devices based on common ferromagnets to date has resulted in rather subtle effects in the range of percent and is difficult to determine. This is mainly due to the small degree of spin injection as well as to competing effects.[10] Amongst them are weak localization/antilocalization, anisotropic magnetoresistance, and fringe or stray field Hall effects. In this work we focus on the stray fields of microstructured ferromagnets utilized in ferromagnet/semiconductor hybrid devices. In particular, we address their magnitude, their dependence on the strength of an in-plane external magnetic field applied either parallel or perpendicular to the easy axis of the large electrode, as well as the magnetostatic interaction between the electrodes.

II. PREPARATION

The micrometer-sized Hall magnetometers are prepared from modulation doped GaAs/AlGaAs heterostructures with a two-dimensional electron system (2DES) 90 nm below the surface. Hall crosses of geometrical width $w = 1.15\ \mu$m are patterned as mesas by electron-beam lithography and chemical etching (depth 100 nm) with a standard etch solution ($1H_2SO_4:8H_2O_2:200H_2O$). Optical lithography and electron-beam evaporation are used for the wiring and bond pads. Each sample consists of four sensor areas which incorporate the micro-Hall crosses. In a subsequent step the ferromagnetic structures are defined on top of the Hall crosses by electron-beam lithography employing alignment marks defined in a previous step. Iron thin films with a thickness of 27 nm were deposited by thermal evaporation. Figure 1(a) shows an atomic force microscope (AFM) image of an iron double structure located on top of a Hall cross. In the preparation process the exposure of the corners of the structures are corrected for proximity effects in electron-beam lithography in order to optimize their shapes. The AFM measurements revealed that the rectangular shape of the mask was completely transferred to the material.

[a]Electronic mail: meier@physnet.uni-hamburg.de

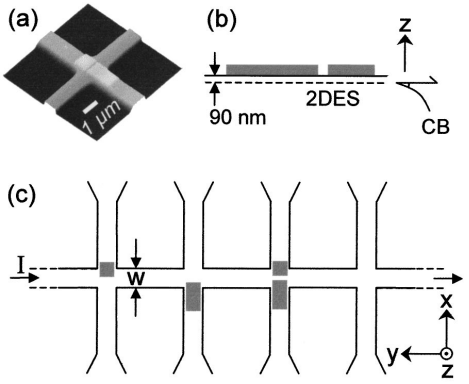

FIG. 1. (a) Atomic force microscope image of a micro-Hall cross ($w = 1.15\ \mu$m) with a pair of iron electrodes on top. (b) Sketch of the cross section. The 2DES is located 90 nm below the surface. (c) Top view of the complete device with a quadratic ($1\ \mu$m$\times 1\ \mu$m), a rectangular ($1\ \mu$m $\times 2\ \mu$m), and a double structure ($1\ \mu$m$\times 2\ \mu$m and $1\ \mu$m$\times 1\ \mu$m). The fourth Hall cross is empty and serves as a reference.

III. EXPERIMENTAL TECHNIQUE AND CALIBRATION

For the measurements an ac current of typically 0.5 μA amplitude and 37.8 Hz frequency is driven through the sensor. The Hall voltages of the crosses are measured simultaneously. A sensor chip is mounted on a chip carrier, which is positioned on a rotatable stage in a probe stick suitable for measurements in the temperature range of 1.6–300 K. The rotatable stage enables characterization of the 2DES with a superconducting magnet in fields of up to 9 T along the z direction directly prior to stray field measurements of the iron structures with the magnetic field in the x or y direction (see Fig. 1). The x and y directions correspond to the spin-transistor and spin-valve geometry, respectively.[4] From carrier concentration of $n_s = 5\times 10^{11}$ cm^{-2} and mobility of $\mu = 700.000$ cm^2 V^{-1} s^{-1} the sensor sensitivity, i.e., the ratio of the Hall voltage to the average stray field $V_H/\langle B_H\rangle$ can in principle be calculated.[11] On the other hand, the most reliable and easiest way to calibrate the sensor is to use the well-known field of the superconducting magnet aligned in the z direction to measure sensor response. It is important to note that this type of calibration procedure is only valid if the Hall sensor is operated in the ballistic regime, i.e., the mean free path l_e of the electrons must exceed the size of the Hall cross.[11,12] In the diffusive regime interpretation of the Hall signal is more complex.[13] In the present samples the ballistic condition is easily satisfied since $l_e = 8.2\ \mu$m.

It is well known that both longitudinal and transverse resistance in a ballistic narrow channel in a 2DES show a nonlinear dependence on weak perpendicular magnetic fields.[14] In our micro-Hall sensors these effects could be observed at low temperatures. In Fig. 2 the longitudinal and the transverse voltage measured at $T = 2$ K exhibit features that have been called the ''last Hall plateau'' and ''camel back.'' [14] From the data in Fig. 2 we calculate an electronic width of the sensor of $w_e = 0.85\ \mu$m, i.e., the depletion width of our mesas is approximately 150 nm.

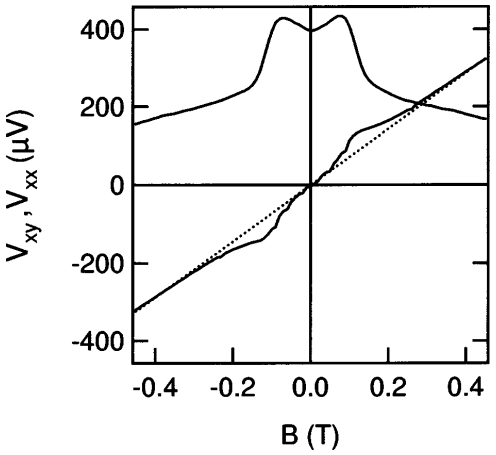

FIG. 2. Transverse and longitudinal voltage measured for a micro-Hall cross at temperature of $T = 2$ K with bias current of $I = 0.5\ \mu$A. Mesoscopic effects known as the last Hall plateau and camel back are clearly observed. The dotted line is a guide to the eye and is the linear sensor response in the absence of mesoscopic effects. From these data an electronic width $w_e = 0.85\ \mu$m is estimated.

IV. RESULTS AND DISCUSSION

We have simultaneously measured three micro-Hall sensors containing a single small ($1\ \mu$m$\times 1\ \mu$m), a single large ($1\ \mu$m$\times 2\ \mu$m), and a double structure ($1\ \mu$m$\times 1\ \mu$m and $1\ \mu$m$\times 2\ \mu$m with a spacing of 150 nm). An empty sensor serves as a reference. This setup ensures that the bias current, temperature, and external magnetic field are identical for all the sensors as well as for the reference.

Figures 3(a)–3(c) show MFM images of the iron electrodes on top of the micro-Hall sensors measured in zero external magnetic field at room temperature in the as-prepared state. The magnetization patterns of the small structures are close to Landau patterns.[15] While in the double structure this is easily seen, the single small structure exhibits a more complex pattern with an additional small closure

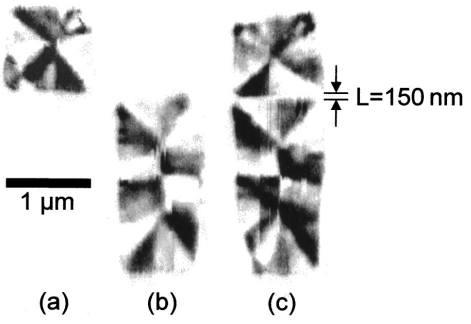

FIG. 3. (a) Magnetic-force microscope images of the iron structures on top of the sensors measured at room temperature. (a) Single small electrode, (b) single large electrode, and (c) electrode pair. The thickness of the structures is 27 nm. The magnetization configuration of the electrode pair right at gap of width $L = 150$ nm is antiparallel.

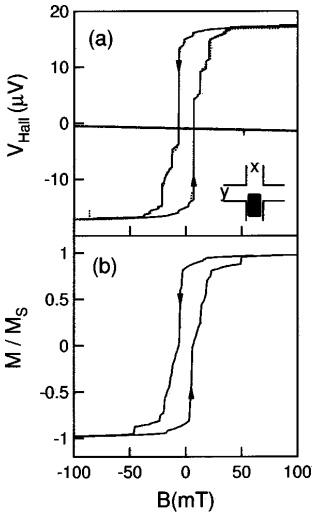

FIG. 4. (a) Hall voltage of the sensor with the single large electrode and the empty reference cross (flat line) at $T=36.5$ K. Shown are two successive sweeps that exhibit nearly no deviations (solid and dotted lines). (b) Simulated hysteresis curve of the integral magnetization for a rectangular ($1\ \mu m \times 2\ \mu m$) iron structure with a thickness of 20 nm.

domain in its lower left corner. In polycrystalline ferromagnetic thin film elements with low overall anisotropy symmetric Néel walls and cross-tie walls are expected for a thickness of 27 nm.[15,16] The large structures in the single as well as in the double structure in Figs. 3(b) and 3(c) exhibit essentially the same magnetization state with closure domains consisting of 90° Néel walls at each end and one cross-tie wall in the middle. The latter can be identified by the chirality of the pattern measured and is not a curl in the magnetization as is often observed in permalloy structures of the same geometry.[17] With respect to transport experiments that use such electrodes as injectors and detectors, the magnetization in the vicinity of the small spacing of the double structure is particularly important. In the MFM image of the double structure antiparallel alignment of the domains next to the spacing is observed in Fig. 3(c), which would correspond to the spin-valve geometry. This behavior is also known from experiment as well as from micromagnetic simulations for permalloy electrodes of the same geometry.[8,9] These calculations also predict that a parallel and an antiparallel magnetization configuration in these domains can be adjusted at will.

Prior to magnetometer measurements the 2DES was characterized by Shubnikov–de Haas oscillations and quantum Hall effect in external magnetic fields aligned perpendicular to the 2DES as previously mentioned. For the stray field measurements that we are pursuing, the sample is within the same cooling cycle, rotated so that the magnetic field becomes aligned in the plane of the 2DES in either the x or y direction. In Fig. 4(a) the transverse voltages of two sensors are shown as a function of the external magnetic field applied along the x direction in two subsequent sweeps (shown by solid and dotted lines).[18] The flat line is the result of the empty reference where the second sweep perfectly reproduces the first. This curve proves that the 2DES itself is not sensitive to magnetic fields applied in plane. It can be used to optimize adjustment of the sensor in the external field. Small constant deviations of the transverse voltage from zero could be caused by structural irregularities on a mesoscopic scale. The voltage measured for the single large electrode in Fig. 4(a) closely resembles a classical hysteresis curve of the integral magnetization. Moving from positive to negative saturation, the transverse voltage displays a reversible change in magnetization followed by two tiny irreversible steps at 6.4 and -1.6 mT, three huge irreversible magnetization jumps at -6.2, -12.2, and -21.2 mT, and again some tiny steps. The way back to positive saturation closely matches the downward sweep, yielding highly reproducible symmetric hysteresis. A simulated hysteresis curve calculated with a computer code supplied by Porter and Donahue[19] displays the normalized magnetization versus the external magnetic field and is shown in Fig. 4(b). Good overall correspondence between both curves is observed, i.e., the squarenesses of the loops and the values of the coercive fields agree well. Still, deviations between experiment and simulation in details of irreversible magnetization switching are evident. Details of the simulation are discussed below.

The temperature dependence of the hysteresis curves measured is rather small. In the regime between 2 and 50 K the amplitude of the Hall signal is constant. Changes of the switching fields between subsequent sweeps are generally small. They tend to be more prominent at the lowest temperatures. Even at 36.5 K almost perfect agreement between two successive sweeps is observed [see Fig. 4(a)]. Above 50 K the signal strength, i.e., the amplitude of the Hall voltage, decreases slowly with an increase in temperature. This can be understood in terms of an increase in carrier concentration n_s in the 2DES which yields a reduced Hall voltage since $V_H \propto 1/n_s$.

An interesting feature was observed when passing through the hysteresis sweep multiple times. While in the first few runs the changes between subsequent sweeps were prominent, the deviations diminished in further sweeps. This training effect was observed in all structures at low temperatures. We attribute this to the special magnetization pattern in the as-prepared state. Although a rather strong magnetic field of 200 mT is applied some field sweeps are required to place the magnetization under the influence of the external field to reach an energetically favorable state. With respect to the application of ferromagnetic structures in spintronics this observation is important because a defined reproducible magnetization state is required.

As mentioned above the sensors are operated in the ballistic regime, i.e., the voltage measured can easily be converted into the average stray field in the sensor area using the calibration in homogeneous perpendicular external magnetic fields. From this procedure the average stray field $\langle B_H \rangle$ generated by the single small structure is obtained. A maximum value of 10.7 mT is observed at saturation, which becomes understandable from a simple model of magnetic charges located right in the sensor area. Accordingly, the stray field measured in the opposite saturation state is equal but re-

versed in sign. By driving the magnetic field up to values of 9 T we examined the possible pinning of domain walls, which could possibly prevent a fully saturated state. However, we observe no difference in the hysteresis curve after the application of such strong fields and conclude that the magnetization state at ± 100 mT is indeed closest to saturation.

This finding is supported by micromagnetic simulations of the hysteresis curve and the corresponding magnetization patterns for the single large electrode. For each external magnetic field a local energy minimum is sought and the corresponding magnetization is calculated. The thermal evaporation process yields polycrystalline iron films and therefore we use a random distribution of the anisotropy direction in the simulation. Different radii of the corners are tested whereby the best agreement is in fact obtained for a rectangular structure. For calculation of the remanent state a grid size of 5 nm is used. The magnetization pattern obtained is in good agreement with the magnetization state observed with the MFM [see Fig. 3(b)]. The resulting magnetization pattern is used as the starting point for computation of the hysteresis curve, which is performed with a grid size of 10 nm. This is a compromise between the actual exchange length $l_{\mathrm{ex}} = \sqrt{A/K_d} = 3.4$ nm of iron,[15,19] where A is the exchange constant and $K_d = \mu_0 M_s^2/2$ the stray field energy constant, on the one hand, and a reasonable computing time on the other. The hysteresis simulated this way is shown in Fig. 4(b). It is in good overall correspondence with the measured curve. The Hall voltage in Fig. 4(a) and the calculated hysteresis curve show a number of irreversible magnetization changes that occur approximately at the same values of the external magnetic field. The deviation of the magnitudes of the jumps between the simulated and experimental curves is expected since the measured transverse voltage is not directly comparable to the normalized integrated magnetization M/M_s plotted in the hysteresis curve.

In the following we discuss the results of the measurements in terms of magnetic stray fields, but the original transverse voltage can easily be recovered via a conversion factor of 0.66 μV/mT (see Fig. 2). With respect to the application of such iron structures in spin-polarized transport it is interesting to compare the behavior of isolated single structures with interacting double ones. The question is whether the interaction completely changes the micromagnetic behavior of the individual structures or if the interaction is small enough to be regarded as a minor correction. Furthermore it is interesting to investigate the difference in magnetic behavior between the two magnetic field configurations when the field is applied in the x and the y directions, respectively. In the y direction a parallel and an antiparallel state should be achievable which corresponds to spin-valve geometry.[4] With the field applied in the x direction a magnetization state close to spin-transistor geometry[4] should be obtainable. To answer these questions we have investigated the structures shown in Fig. 1(c) by recording four transverse voltages simultaneously. Typical data are depicted in Figs. 5(a)–5(c) for the single small, the single large, and the double structure. The solid (and dotted) lines denote measurements for the magnetic field in the x and the y direction, respectively.

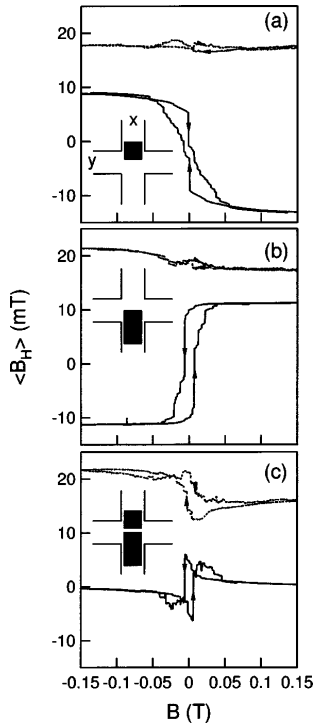

FIG. 5. Measured Hall curves for the (a) small, (b) large, and (c) double structures. Measurements with the external magnetic field aligned in the x direction (solid line) and in the y direction (dotted line) are shown. The latter are offset by $+20$ mT for clarity.

We start with the spin-transistor geometry, i.e., the magnetic field aligned in the x direction (solid lines). As can be seen in Fig. 5(a) the sign of the average stray field for the single small structure deviates from the loop of the single large electrode in Fig. 5(b). This is caused by the mirrored position of the structure on the sensor with respect to the current. This indicates again that the measured stray field curves are not directly comparable to conventional hysteresis curves. Also, details of the micromagnetic behavior in the two electrodes deviate, implying that the shape anisotropy governs the overall micromagnetic behavior. Obviously, other anisotropy contributions play a minor role, presumably because they are averaged out by the polycrystalline composition of the iron. As a matter of fact, in the easy direction with the magnetic field parallel to the x direction the saturated state of the large structure is more readily reached than that of the smaller one. Notice, however, the main irreversible change in magnetization is observed at smaller magnetic field values for the small structure. The stray field strengths of the two single structures are comparable in this field geometry. This is obvious because the magnetic charges at the edge of the electrodes in the sensor areas, i.e., the magnetic

line charge density times the width of the structure, are nearly the same at saturation.

Results for the double structure are shown in Fig. 5(c). Here the stray field curves deviate strongly from conventional hysteresis. This is expected because the simple connection between average stray field in the sensor area and integral magnetization is no longer valid. Interestingly, the stray field is considerably reduced in the double structure, with a maximum value of only 6.3 mT. The main irreversible jumps observed for the single structures can be identified in the measurement for the double structure at approximately the same field values. For example, the first huge jump in the downward sweep of the single large structure at -6.2 mT appears at -5.8 mT in the downward sweep of the double structure. This suggests magnetostatic interaction between the two electrodes which is however a small perturbation for a spacing of 150 nm. This is supported by the magnetization pattern in Fig. 3(c), which closely resembles the pattern of the noninteracting structures in Figs. 3(a) and 3(b). Accordingly, the overall micromagnetic behavior of the single structures can be identified in the loop measured for the double structure. This is consistent with micromagnetic simulations based on permalloy structures of comparable geometry.[9] On the other hand, the stray field in the sensor area, which should be kept at a minimum in spin-polarized transport, is considerably reduced. This is caused by interaction of the two ferromagnetic contacts being in close proximity which tends to reduce the demagnetization energy, i.e., the stray field.

The consistency of our interpretation becomes even more evident when the sum of the curves for the single structures is compared to the directly measured trace of the interacting electrodes. This can be seen in Figs. 6(a) and 6(b). The shape of the total curve for the noninteracting structures exhibits the same features as the directly measured curve for the interacting electrodes. Remarkably, it is possible to identify the irreversible jumps and their switching fields which are only slightly reduced for the interacting structures. As an example, we concentrate on the jumps indicated by arrows that are marked in both curves. Altogether, the interaction seems to reduce the coercivity.

In the following we proceed to the experiments in spin-valve geometry, i.e., the magnetic field is aligned in the y direction. The corresponding traces are shown by dotted lines in Fig. 5(a)–5(c). The stray fields measured for the single structures are small in comparison to the ones in spin-valve geometry discussed before. Their amplitudes are in the range of 1 mT for both structures. In the model of magnetic charges they now reside on the edges which do not lie in the sensitive area of the sensor, i.e., the stray field is expected to be strongly reduced. For spintronic devices based on ferromagnet/semiconductor hybrids this means that electron transport through the channel is hardly affected by stray fields in spin-valve geometry. The shape of these curves is not as regular as in spin-transistor geometry. When repeating the magnetic field sweep the coarse shape of the curve remains the same but the deviations are more pronounced in comparison to in spin-transistor geometry. The result for the double structure depicted in Fig. 5(c) cannot be associated straightforwardly with the sum of the single structures.

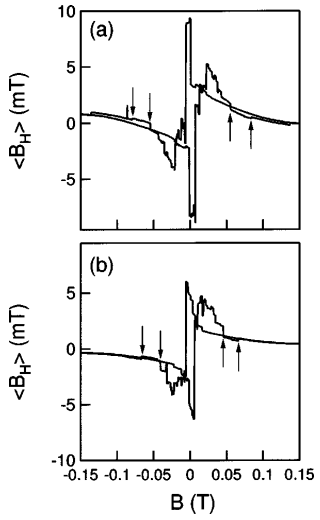

FIG. 6. Comparison of (a) the sum of the Hall signals for the single small and the single large structures with (b) the Hall signal measured for the double structure. The arrows indicate examples of irreversible magnetization changes which can be found in (a) and (b). The external magnetic field is applied parallel to the x direction.

An important consequence for the application of such structures in spin-polarized transport is that the stray field strength produced by ferromagnetic electrodes is comparable for both geometries. One might expect at first glance that the stray field is strongly enhanced if the external magnetic field is applied along the x direction in comparison to along the y direction. The experimental result, however, is that the stray field strength in both configurations is virtually equal for ferromagnetic electrodes in close proximity. In principle, this can be understood as a reduction of demagnetization energy of the two adjacent electrodes.

V. CONCLUSIONS

By means of Hall micromagnetometry we have studied thin individual and interacting iron structures in the μm-size range. Such structures are suitable as electrodes for spin-polarized transport experiments in ferromagnet/semiconductor hybrid devices. The interaction between the closely coupled electrodes is small because the hysteretic behavior of the single structures can be retrieved in the hysteresis curve of the double structure. The measured stray field of the double iron structure is considerably reduced in comparison to that of the single structures and it is found to be of the same size independent of the alignment of the external in-plane magnetic field.

ACKNOWLEDGMENTS

The authors would like to thank U. Merkt for valuable discussions and encouragement, D. Grundler for his support in Hall micromagnetometry, and Ch. Heyn for the MBE

samples. They thank S. McVitie for discussion about the interpretation of MFM images. The expertise and technical assistance of J. Gancarz is appreciated. The authors acknowledge financial support by the Deutsche Forschungsgemeinschaft through the Sonderforschungsbereich 508 ''Quantenmaterialien'' and by the NEDO international joint research grant program.

[1] G. A. Prinz, Phys. Today **48**, 58 (1995).
[2] S. A. Wolf, D. D. Awschalom, R. A. Buhrman, J. M. Daughton, S. von Molnár, M. L. Roukes, A. Y. Chtchelkanova, and D. M. Treger, Science **294**, 1488 (2001).
[3] D. Grundler, Phys. Rev. B **63**, 161307 (2001).
[4] T. Matsuyama, C.-M. Hu, D. Grundler, G. Meier, and U. Merkt, Phys. Rev. B **65**, 155322 (2002).
[5] O. Wunnicke, Ph. Mavropoulos, R. Zeller, P. H. Dederichs, and D. Grundler, Phys. Rev. B **65**, 241306 (2002).
[6] H. J. Zhu, M. Ramsteiner, H. Kostial, M. Wassermeier, H.-P. Schönherr, and K. H. Ploog, Phys. Rev. Lett. **87**, 0166011 (2001).
[7] S. Datta and B. Das, Appl. Phys. Lett. **56**, 665 (1990).
[8] G. Meier and T. Matsuyama, Appl. Phys. Lett. **76**, 1315 (2000).
[9] G. Meier, M. Halverscheid, T. Matsuyama, and U. Merkt, J. Appl. Phys. **89**, 7469 (2001).
[10] G. Meier, T. Matsuyama, and U. Merkt, Phys. Rev. B **65**, 125327 (2002).
[11] A. Geim, S. V. Dubonis, J. G. S. Lok, I. V. Grigorieva, J. C. Maan, L. Theil Hansen, and P. E. Lindelof, Appl. Phys. Lett. **71**, 2378 (1997).
[12] F. M. Peeters and X. Q. Li, Appl. Phys. Lett. **72**, 572 (1998).
[13] I. S. Ibrahim, V. A. Schweigert, and F. M. Peeters, Phys. Rev. B **57**, 15416 (1998).
[14] C. W. J. Beenakker and H. van Houten, Phys. Rev. Lett. **63**, 1857 (1989).
[15] A. Hubert and R. Schäfer, *Magnetic Domains—The Analysis of Magnetic Microstructures* (Springer, Berlin, 1998).
[16] S. Middelhoek, J. Appl. Phys. **34**, 1054 (1963).
[17] S. McVitie, G. S. White, J. Scott, P. Warin, and J. N. Chapman, J. Appl. Phys. **90**, 5220 (2001).
[18] An offset in magnetic field B of -6 mT observed in all measurements is presumably generated by remanence of the superconducting coil and is corrected.
[19] Oommf, object oriented micromagnetic framework, http://math.nist.org/oommf.

Publication 2

J. Appl. Phys. **93**, 8400 (2003)

JOURNAL OF APPLIED PHYSICS VOLUME 93, NUMBER 10 15 MAY 2003

Stray fields of iron electrodes for spin-polarized transport

M. Barthelmess,[a] A. Thieme, R. Eiselt, and G. Meier
Institut für Angewandte Physik und Zentrum für Mikrostrukturforschung, Universität Hamburg Jungiusstraße 11, D-20355 Hamburg, Germany

(Presented on 15 November 2002)

In semiconductor spintronic devices that incorporate ferromagnetic materials the stray-field configuration in the plane of the two-dimensional electron system is of crucial importance. We investigate the stray fields of iron electrodes suitable as injector and detector for spin-polarized transport in hybrid semiconductor/ferromagnet devices. Magnetic-force microscopy images of an electrode pair are derived from simulated magnetization patterns. The calculated averaged stray field is compared to the experimental signal of a ballistic Hall micromagnetometer comprising a two-dimensional electron system in a GaAs/AlGaAs-heterostructure 90 nm below the electrodes. Good agreement between simulation and experiment is obtained. © *2003 American Institute of Physics.* [DOI: 10.1063/1.1543131]

I. INTRODUCTION

Spintronics with semiconductors and ferromagnets is a vivid and intensively investigated research field.[1,2] Electrical spin injection has been demonstrated successfully for ferromagnet/semiconductor hybrid systems utilizing the degree of circular polarization of light emitted from the semiconductor.[3–5] All-electrical detection of spin-polarized transport has been observed, e.g., by Hu *et al.*[6] Recently, we could measure a gate-voltage-dependent magnetoresistance in InAs/permalloy hybrid transistors.[7] However, the amplitudes in these transport experiments are rather small and difficult to interpret since parasitic effects in the semiconductor could mimic spin-dependent transport. To exclude them and to corroborate the interpretation of the magnetoresistance as spin effect detailed investigations of the stray fields are imperative. Here we compare experimental results obtained from magnetic-force microscopy (MFM) and Hall micromagnetometry with stray fields inferred from micromagnetic simulations of the domain structure of the electrodes. We take advantage of the fact that Hall micromagnetometry seizes the averaged stray field in the channel of a ballistic two-dimensional electron system (2DES).[8–11]

II. MICROMAGNETIC SIMULATIONS

The iron electrodes have a thickness of 20 nm and a size of $2\ \mu\text{m}\times 1\ \mu\text{m}$ and $1\ \mu\text{m}\times 1\ \mu\text{m}$, respectively. They are separated by a 150 nm wide spacing (see Fig. 1). The asymmetric geometry results in distinct micromagnetic behaviors. In particular, it provides different switching fields in externally applied magnetic fields. The magnetization pattern of the electrodes is simulated with a computer code supplied by Porter and Donahue.[12] For iron, a saturation magnetization of 1 700 000 A/m, an exchange constant of 21×10^{-12} J/m, and an anisotropy constant of 48 000 J/m^3 are chosen. A grid size of 5 nm close to the exchange length of iron is employed to calculate the as-prepared $B=0$ state. In order to obtain a reasonable computing time, the hysteresis loop itself is calculated with a grid size of 10 nm using the as-prepared state as starting magnetization configuration. The external magnetic-field B is applied parallel to the easy axis of the larger structure (x direction, see Fig. 1) and is increased in steps of 1 mT up to +200 mT, then decreased to −200 mT. The loop is completed by increasing the field again to +200 mT.

To be able to compare the simulation to the Hall-micromagnetometer measurements,[8,11] the stray fields of the iron electrodes are determined from the array of magnetic dipoles resulting from the micromagnetic calculation. The strength of each dipole is given by the volume of the lattice cell $10\times 10\times 20\ \text{nm}^3$ times the saturation magnetization. With this model the z component of the stray field, that is effective for a 2DES, can easily be calculated for various distances. The second derivative of the z component of the stray field with respect to the z direction corresponds to the signal measured with magnetic-force microscopy.[13]

III. COMPARISON TO EXPERIMENTAL RESULTS

Figure 1(a) shows the magnetization of both electrodes calculated for $B=0$. The sketch in Fig. 1(b) illustrates the domains. The quadratic electrode exhibits a Landau pattern, the larger electrode two vortices separated by a cross-tie wall. The vortices consist of 90° and 180° Neél walls, while the cross-tie wall is a combination of a 180° Neél wall and a 180° Bloch wall, such that the magnetization is oriented out-of-plane at the center of the cross-tie wall. Figure 1(c) represents the z component of the second derivative of the stray field calculated in a vertical distance of 70 nm, which is a typical MFM lift-scan height. Here, the cross-tie wall can be clearly observed and should not be misinterpreted as a magnetization curl which is often observed in permalloy structures of the same geometry.[11,14,15] Most interesting is the region in the gap between the electrodes since in a spin-transistor device this is the semiconductor channel. At $B=0$, the magnetizations at the channel are aligned antiparal-

[a]Electronic mail: mbarthel@physnet.uni-hamburg.de

J. Appl. Phys., Vol. 93, No. 10, Parts 2 & 3, 15 May 2003

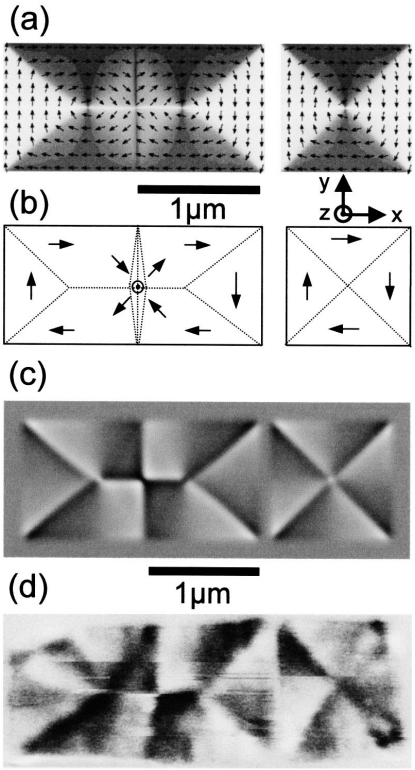

FIG. 1. (a) Calculated magnetization pattern of two 20-nm-thick iron electrodes separated by a 150-nm-wide gap at $B=0$. (b) Sketch of the domains illustrating the formation of the cross-tie wall in the larger electrode. (c) Second derivative of the stray field calculated at a vertical distance of 70 nm. (d) MFM image of the electrode structure prepared by electron-beam lithography. Note that the upper scale is valid for (a) and (b) and the lower for (c) and (d).

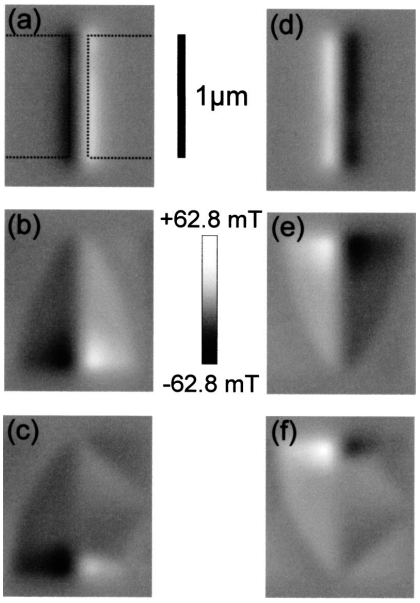

FIG. 2. Stray field strengths in a 1150 nm×1400 nm section of the structure in Fig. 1 calculated for six external magnetic fields. The large and small electrodes lie on the left- and right-hand side, respectively. Downsweep: (a) +200 mT which is next to positive saturation, (b) 0 mT, and (c) −5 mT after the first irreversible magnetization change. Upsweep: (d) −200 mT, (e) 0 mT, and (f) +5 mT. The maximum and minimum local stray-field strengths are +62.8 mT and −62.8 mT, respectively.

lel as can be seen in Fig. 1(c). This results in an overall stray field smaller than in the parallel configuration.

Polycrystalline iron electrodes of the geometry discussed above are prepared by electron-beam lithography, thermal evaporation, and a lift-off process. Their MFM image in Fig. 1(d) agrees well with the simulated one, see, e.g., the chessboardlike structure at the cross-tie wall in Figs. 1(c) and 1(d). The antiparallel magnetization next to the spacing causes the reversed gray scale along the channel in the large and small electrode observed in the simulated as well as in the measured MFM image.

In the following we analyze the region between the ferromagnetic contacts in more detail. Figure 2 shows a 1150 nm×1400 nm section of the local stray-field distribution at different external magnetic-field strengths, calculated for a distance of 90 nm below the ferromagnetic electrodes. The contour of the contacts is indicated in Fig. 2(a) which shows the saturated state at +200 mT. Figure 2(b) represents the remnant state. In Fig. 2(c), the external magnetic field of −5 mT has caused the magnetization pattern of the smaller electrode to reverse its direction resulting in a parallel alignment of the domains next to the channel. The strongest local stray fields occur at $B=\pm 5$ mT just after this irreversible magnetization change. They have an absolute value of 62.8 mT. Figures 2(d)–2(f) represent the situation at the corresponding points in the upsweep of the loop underlining the symmetry of the hysteresis curve. In the saturated states of Figs. 2(a) and 2(d) the average stray-field penetration into the semiconductor channel is strongest.

Experimentally, the average of the stray field is measured by means of Hall micromagnetometry. The Hall micromagnetometer consists of a modulation-doped GaAs/AlGaAs heterostructure with a 2DES 90 nm below the surface. The Hall crosses are patterned as mesas by electron-beam lithography and chemical etching with a geometrical width of $w=1150$ nm and an electronic width of $w_{el}=850$ nm. Experimental details are reported elsewhere.[11] To compare the simulation with the experimental results the average of the stray field is calculated 90 nm below the surface in a 850 nm×850 nm wide region which corresponds to the active sensor area. This procedure is performed for each value of the applied magnetic field. The resulting ''hysteresis'' curve is shown in Fig. 3(a) and can be compared to the measured one in Fig. 3(b). The overall shapes of the two curves are in good agreement. The stray field maxima occur at approximately the same values of the external field, namely, at −5 and +5 mT in the simulated curve, and at −5.8 and +6.2 mT in the measured one. Although the mea-

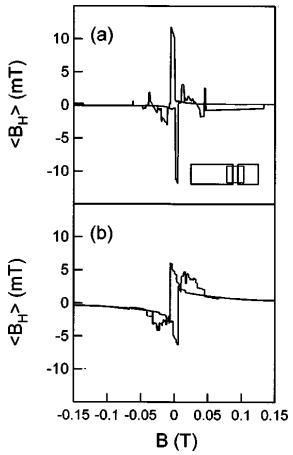

FIG. 3. (a) Calculated averaged stray fields of the 850 nm×850 nm sensor area under the iron electrodes as indicated in the inset vs the externally applied magnetic field in the range between −150 and 150 mT. (b) Hall-sensor signal measured at a temperature of $T=37$ K.

sured and simulated averaged stray-field strengths are both in the few-mT regime the theoretical values are a factor of 2 stronger than measured. This might be due to a different saturation magnetization of the real polycrystalline iron structures or due to the specific sensor area chosen. This area strongly depends on the effective electronic width which results from depletion and can only be determined rather indirectly from mesoscopic transport effects.[11]

IV. CONCLUSIONS

We have investigated stray fields of micrometer-sized iron structures that are suitable as injectors and detectors for spin-polarized transport. Simulations of the magnetization of the as-prepared state show good agreement with MFM images measured at room temperature. For the entire hysteresis curve of the electrode configuration the averaged stray fields in the 2DES channel between the ferromagnetic electrodes are calculated in the region of a Hall micromagnetometer and are compared to the measured sensor response. In summary, the combination of Hall micromagnetometry and micromagnetic simulation provides a powerful tool for the analysis of stray fields in ferromagnet/semiconductor hybrid systems.

ACKNOWLEDGMENTS

The authors would like to thank U. Merkt for encouragement and D. Grundler for valuable discussions about Hall micromagnetometry. We acknowledge financial support of the Deutsche Forschungsgemeinschaft via the Sonderforschungsbereich 508 ''Quantenmaterialien,'' the Graduiertenkolleg ''Physik Nanostrukturierter Festkörper,'' the NEDO International Joint Research Grant Program, and the BMBF (Grant No. 13N8283).

[1] G. A. Prinz, Phys. Today **48**, 58 (1995).
[2] S. A. Wolf, D. D. Awschalom, R. A. Buhrman, J. M. Daughton, S. von Molnár, M. L. Roukes, A. Y. Chtchelkanova, and D. M. Treger, Science **294**, 1488 (2001).
[3] H. J. Zhu, M. Ramsteiner, H. Kostial, M. Wassermeier, H.-P. Schönherr, and K. H. Ploog, Phys. Rev. Lett. **87**, 0166011 (2001).
[4] V. F. Motsnyi, J. De Boeck, J. Das, W. Van Roy, G. Borghs, E. Goovaerts, and V. I. Safarov, Appl. Phys. Lett. **81**, 265 (2002).
[5] A. T. Hanbicki, B. T. Jonker, G. Itskos, G. Kioseoglou, and A. Petrou, Appl. Phys. Lett. **80**, 1240 (2002).
[6] C.-M. Hu, J. Nitta, A. Jensen, J. B. Hansen, and H. Takayanagi, Phys. Rev. B **63**, 125 333 (2001).
[7] G. Meier, T. Matsuyama, and U. Merkt, Phys. Rev. B **65**, 125327 (2002).
[8] F. M. Peeters and X. Q. Li, Appl. Phys. Lett. **72**, 572 (1998).
[9] A. Geim, S. V. Dubonos, J. G. S. Lok, I. V. Grigorieva, J. C. Maan, L. Theil Hansen, and P. E. Lindelof, Appl. Phys. Lett. **71**, 2379 (1997).
[10] T. M. Hengstmann, D. Grundler, N. Klockmann, H. Rolff, Ch. Heyn, and D. Heitmann, IEEE Trans. Magn. **38**, 2535 (2002).
[11] G. Meier, R. Eiselt, and M. Halverscheid, J. Appl. Phys. **92**, 7296 (2002).
[12] *Oommf*, object oriented micromagnetic framework, http://math.nist.org/oommf
[13] U. Hartmann, Phys. Lett. A **137**, 475 (1989).
[14] S. McVitie, G. S. White, J. Scott, P. Warin, and J. N. Chapman, J. Appl. Phys. **90**, 5220 (2001).
[15] G. Meier and T. Matsuyama, Appl. Phys. Lett. **76**, 1315 (2000).

3.3. Hall effect and bend resistance measurements

In the previous section stray field measurements on microstructured electrodes made of iron are presented. Iron is advantageous regarding the application in spintronic devices due to its large saturation magnetization $M_S = 1.700.000\ \frac{A}{m}$ and comparatively strong exchange constant. These properties guarantee a high stability of the magnetization to external magnetic noise. However, an important requirement is the reproducibility of specified domain configurations. Permalloy offers simple domain structures even in electrodes of micrometer sizes. In contrast to pure iron the alloy $Ni_{80}Fe_{20}$ has an almost vanishing anisotropy constant, $K_1 = 100\ \frac{J}{m^3}$. This guarantees micromagnetic properties independent of the crystallographic structure of the substrate. In addition, Permalloy shows no magnetostrictive effect.

The Py electrodes which have been produced for investigation with Hall micromagnetometry have a lateral geometry of $4 \times 0.8\ \mu m^2$ and $8 \times 0.8\ \mu m^2$ with a thickness of 17 nm (confer Sec. 2.3). The electrodes exhibit nearly single-domain configurations. Since spintronic devices most commonly are used as switches, only two magnetic states of the electrodes are desired. In Fig. 2.3 the spin-valve and the spin-transistor configuration has been introduced. In the following, we first discuss measurements in spin-valve configuration.

For characterization of the 2DES the fifth Hall sensor (see Fig. 2.3(b)) has been used on which no ferromagnetic structure is prepared. In Fig. 3.6 the longitudinal voltage, V_{xx}, and the bend voltage, V_{Bend}, are depicted in dependence on a perpendicular external magnetic field, B_{ext}. The longitudinal voltage has been taken between the first and the fifth Hall sensor. Above a magnetic field of 0.5 T Shubnikov-de Haas (SdH) oscillations occur in both signals. The analysis of the oscillations and the Hall voltage (not plotted) result in an electron density of $n = 3.5 \cdot 10^{-11}\ cm^{-2}$ and a mobility of $\mu = 290.000\ \frac{cm^2}{Vs}$.

In the magnetic field range below 200 mT the longitudinal voltage shows a noticeable increase that can be attributed to a classical effect. Due to the large mean free path, $l_e = 2.8\ \mu m$, the electrons move ballistically and behave like classical particles [86]. At the normalized magnetic field $B_0 = \frac{\hbar k_F}{e w}$ the electron orbits have a radius in the order of the Hall bar width, $R = w$. In smaller magnetic fields ($B_{ex} < B_0$) the so-called guiding-center drift along the curved 2DES channel walls of the Hall crosses predominates. The specific enhancement of V_{xx} through guiding depends on the minimal radius of curvature of the corners.

Like V_{xx} the bend voltage, V_{Bend}, shows a strong dependence on weak magnetic fields. Especially at zero magnetic field the negative value of V_{Bend} is of interest. However, the measured curve also can be explained with a classical model in which electrons are billiard balls and guiding-center drifts occur. The inset of Fig. 3.6 shows the calculated bend resistance for a Hall sensor with hard walls and finite curvature of the corners [87]. The resistance is normalized by the contact resistance of the leads, $R_0 = \frac{h}{2e^2}\frac{\pi}{k_F w}$. The measured and the calculated curve similar characteristics. Due to the larger curvature of the corners in the simulation the negative bend resistance at zero magnetic field is larger than the measured bend resistance of $\frac{R_{Bend}}{R_0} = -0.09$.

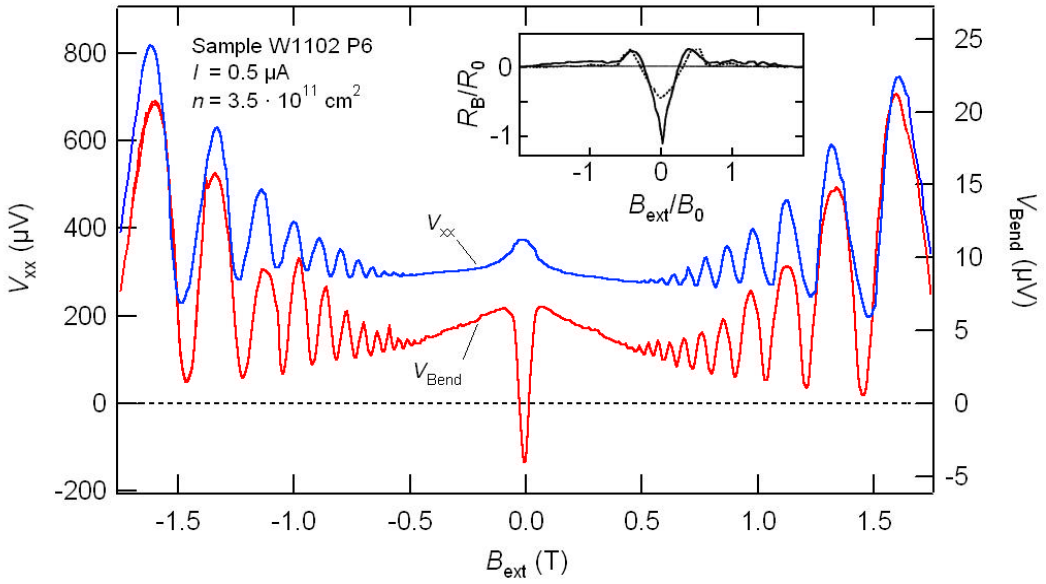

Fig. 3.6.: Longitudinal voltage, V_{xx}, and bend voltage, V_{Bend}, in dependence on a perpendicular external magnetic field. Below 200 mT both signals show variations due to classical effects. Simulations of the bend resistance (inset) qualitatively match the measured signal [87].

For comparison of the stray fields of the electrodes depicted in Fig. 2.3(b) the parallel measured signals of all Hall sensors are shown in Fig. 3.7. The external magnetic field is applied in the plane of the 2DES along the easy axis of the electrodes. On the left axis the Hall voltages, V_{Hall}, are plotted for two subsequent hysteresis curves (No. 6, 7). The hysteresis curves are offset for clarity. The right axis shows the average perpendicular stray field, B_{Hall}, according to Eq. (2.3). Variations in B_{Hall} solely originate from the response of the ferromagnetic electrodes to the external magnetic field which is evident from the constant signal of the fifth empty Hall sensor. The measurements are performed at 10 K and show a high signal-to-noise ratio with well reproducible jumps in the Hall response of the electrodes. The resolution of the Hall signal is less than 20 μT.
The hysteresis curves of the second, third, and fourth Hall sensor clarify that primarily the small ferromagnetic electrode is relevant to the signal. A schematic drawing next to the numbering of the Hall sensors illustrates the electrode configuration. Whereas the large electrode upon sensor four has no significant jump in the hysteresis curve the signal of the second sensor with the double electrode nearly matches the third sensor with the small electrode. The large jumps of the Hall voltage of sensor two and three correspond to a complete reversal of the magnetization of the small electrode. The reversals of the large electrode are not detected, since the end domains are located outside the sensor area. The external magnetic field, at which the reversal of the small electrode in double configuration occurs, is increased to a value of $B_{\mathrm{ext,d}} = \pm 12$ mT in comparison to $B_{\mathrm{ext,s}} = \pm 10$ mT for the single electrode. The increase is due to stray field coupled stabilization of the

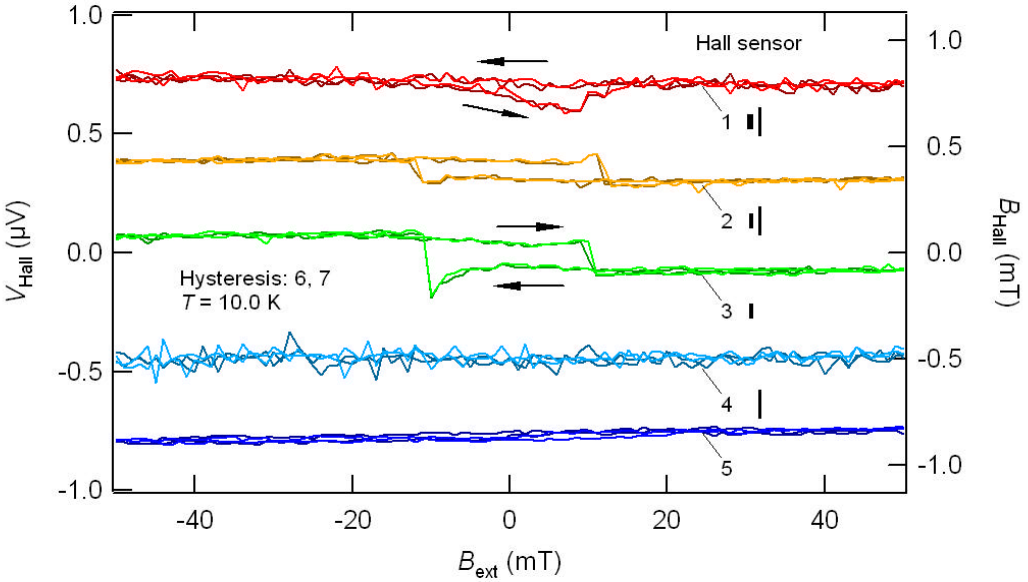

Fig. 3.7.: Hall signal, V_{Hall}, and calculated average stray field, B_{Hall}, of the electrodes from Fig 2.3(b). The external magnetic field is applied along the easy axes, i. e. long axes of the electrodes. The hysteresis curves of the Hall sensors are offset for clarity.

small electrode by the large one. In addition, the stray field coupling between the electrodes induces a reduction of the stray field within the sensor area. A smaller difference in Hall voltage between the two saturation states can also be seen clearly .
The small electrode upon sensor one is 200 nm wider than the other electrodes and has a size of $4 \times 1.0\ \mu\mathrm{m}^2$. The inter-element distance is the same as the one in the double electrode on sensor two. However, the hysteresis notably differs from the signal of the second sensor. The Hall signal at positive and negative saturation is nearly equal, which points to an almost ideal symmetry of these two magnetization states. In addition, since no jump of the Hall signal during the down-sweep is observable the switching of the magnetization also proceeds symmetrically. The up-sweep of the hysteresis exhibits a more complicated signal around zero external field. After a reversible domain wall movement two jumps occur at $= +10$ mT and $+13$ mT, These values lie in the same range as the ones of the double electrode upon sensor two.
No concrete conclusion can be drawn regarding the sign of the Hall signal and the circulation direction of the hysteresis. Since the electrodes are symmetrically located on top of the sensors all changes of the magnetization within the whole electrode are detected as average. This includes minor switching processes in the end domains.
The temperature dependence of the stray field of the double electrode on top of Hall sensor two also has been investigated. In Fig. 3.8 the hysteresis curves between $T = 10$ K and $T = 40$ K are plotted with offsets for clarity. The left and right axis show the Hall voltage and calculated average stray field, respectively. The range of the external field, B_{ext}, is -60 mT to $+40$ mT. Subsequent measured hysteresis curves demonstrate the re-

producibility of the Hall signals at different temperatures.
Two significant properties of the smaller electrode in double configuration can be identified with rising temperature. First, the difference of stray field in positive and negative saturation stays constant. This means, the magnetization of the double electrode in saturation is nearly independent of temperature as expected far below the Curie temperature of $T_{C,Py} = 870$ K [88]. Secondly, the external magnetic field, at which the smaller electrode totally changes its magnetization direction, decreases at higher temperatures. The switching field of $B_{sw} = \pm 11$ mT at 10 K is reduced to a value of ± 6 mT at 40 K. The inset of Fig. 3.8 illustrates the decrease of the measured switching fields, B_{sw}, with temperature. The value of 0.2 mT at room temperature was achieved by MFM measurements on the same structure. At finite temperatures the local magnetization will fluctuate due to thermal excitations. The probability that a new magnetization configuration with a change in energy ΔE will be reached is given by the Boltzmann factor, $\exp(-\frac{\Delta E}{k_B T})$. This explains the roughly exponential temperature dependence of the switching probability.
A further method which has been used to analyze the magnetization states of electrodes in spin-valve configuration is the measurement of the bend resistance. This technique is appropriate to this configuration since the bend resistance sensitively responds to the position of stray fields within the area of the sensor. In particularly symmetrically located end domains produce a finite magneto-resistive signal. The investigation of magnetic switching fields by bend resistance measurements has specific advantages in comparison

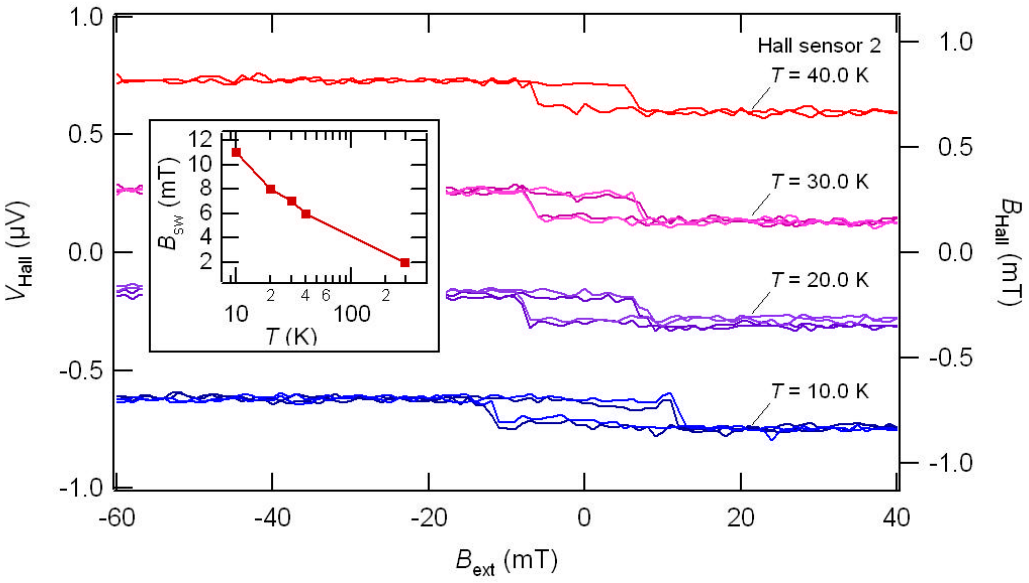

Fig. 3.8.: Temperature dependent measurement of the stray field of the double electrode on top of sensor two. The magnetic switching field, B_{sw}, of the small electrode, which is primarily detected, decreases with temperature. The jump height of the switching stays almost constant. The inset shows an exponential temperature dependence of B_{sw}. The value of 0.2 mT at room temperature is obtained by MFM measurements.

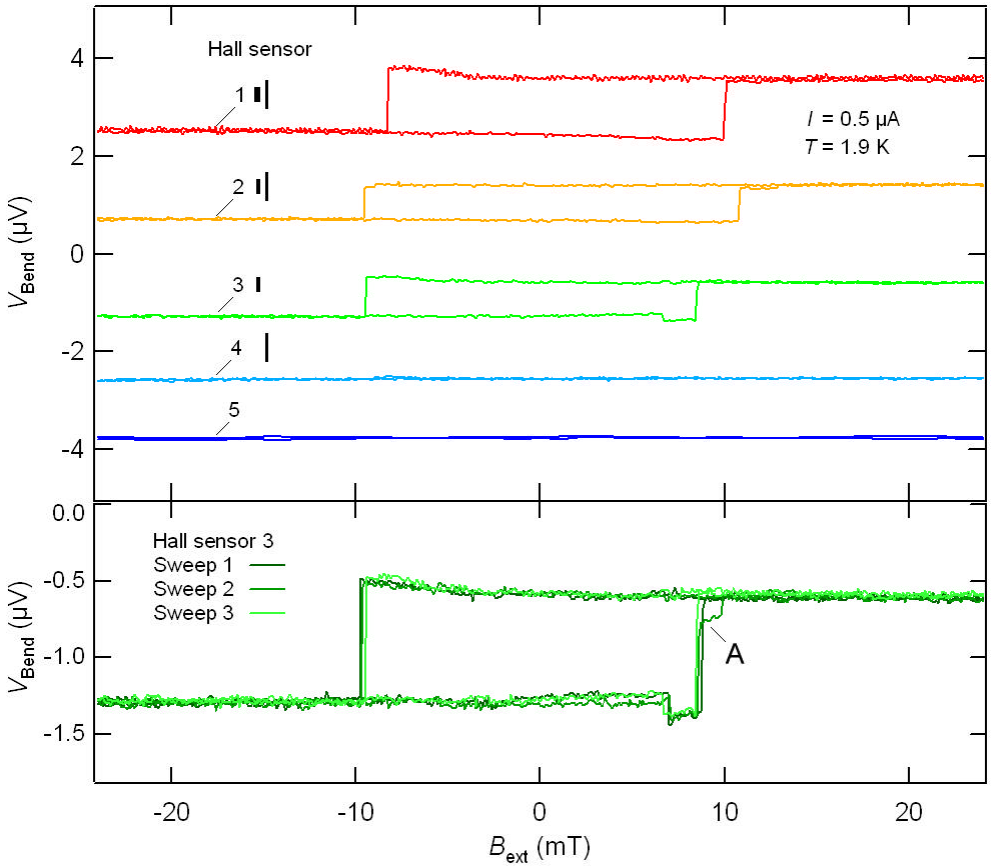

Fig. 3.9.: Bend resistances of electrodes in spin-valve configuration (compare Fig. 2.3(b)). The signals of sensors one to three are dominated by the stray field of the small electrode. The magnetic fields at which the reversal process occurs is comparable to results of Hall measurements. Additional steps of the bend voltage can be resolved at the magnetization reversal (A) in the up-sweep of sensor three.

to Hall micromagnetometry due to the enhanced signal-to-noise ratio. However, to measure the bend resistance of ferromagnetic microstructures on top of a Hall bar only one sensor chosen at the same time because of the bias current. Additionally, the bend voltage, V_{Bend}, cannot be interpreted like the Hall voltage as average magnetic stray field. On the other hand, the signal strongly depends on the detailed stray field distribution within the sensitive area. No conclusion can be drawn on the local stray field strength.
The bend resistance has been measured for the five Hall sensor plotted in Fig. 2.3(b). In Fig. 3.9 the results are depicted in an external magnetic field range of ± 24 mT. A current of $I = 0.5\ \mu$A has been chosen at a temperature of 1.9 K. Similar to measurements of the Hall voltage in Fig. 3.7 no signal of the large electrode on top of sensor four can be detected. Thus, the signals of sensor one to three are dominated by the stray field of the small electrode. This is supported by the similarity of the hysteresis curves one to three. The measurements show one large jump of the bend voltage in the up and down sweep, respectively, which can be identified as complete magnetization reversal. In comparison

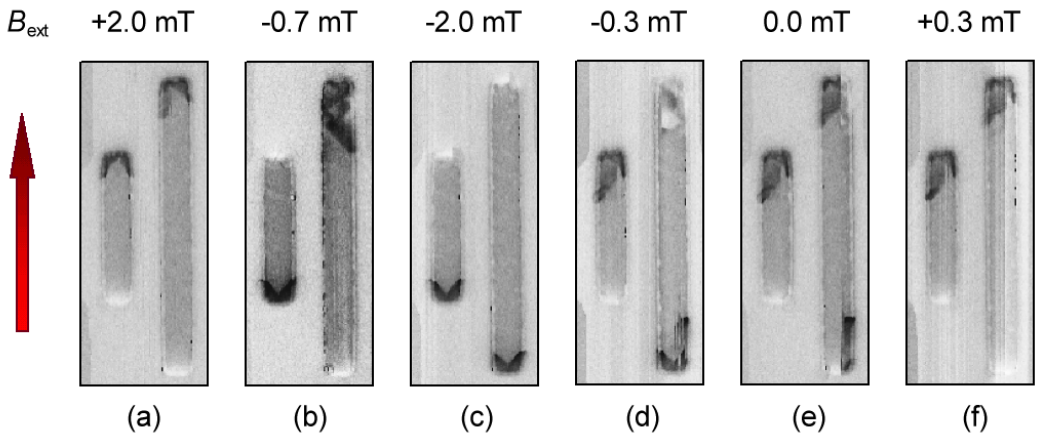

Fig. 3.10.: MFM measurements of the double electrode upon Hall sensor two. The sequence of images shows a complete hysteresis. The magnetization of the double electrode can be aligned to a parallel (a, c, e, f) and anti-parallel (b, d) configuration as required for spin-valve devices.

to the Hall signal the jumps more precisely indicate the switching processes since the signal strength is enhanced by a factor of five resulting in an increased signal-to-noise ratio. The reason for this is due to the direction of the bend current which is driven around the sensor corner and primarily detects only one of the two end domains. The sensitive area principally is expanded along the lead of the current direction. However, the positions of the end domains of the large electrode are outside the sensitive area and do not influence the bend signal. In addition, an influence of the small electrode on the magnetization reversal of the large electrode by stray field interaction cannot be seen.
The magnetic field strengths at which the jumps of the bend voltage appear correspond to the measurements of the Hall voltage. The single small electrode on top of sensor three shows a reversal process at -9.4 mT and $+8.6$ mT. The switching fields of the small electrode in double configuration upon sensor two are increased to a value of -9.6 mT and $+10.8$ mT. This effect can be attributed to stray field interaction between the electrodes which already has been found in Hall measurements. The high resolution of the bend signal also reveals minor switching processes. The small electrode on sensor three shows additional steps of the bend voltage at the magnetization reversal in the up-sweep (see (A) in Fig. 3.9). Additionally, the final reversal is preceded by a first step which occurs at $+7$ mT. The decrease of the step is in contrast the final reversal which shows an increase of the signal. This behavior of the electrode indicates the creation of a domain wall. The complete magnetization reversal finally proceeds in two steps. A slight difference between subsequently measured hysteresis curves of the complete reversal can be observed. Though the jump height of the bend voltage cannot clearly be connected a stray field strength, a comparison between the bend signals of electrodes with the same positions upon a sensor is possible. Due to the same position and size of the small electrodes on top of sensor two and three they have an almost equal jump height. The different jumps

of the small electrode upon sensor one can directly be attributed to its larger width. Only a single reversal step in each sweep direction is observed which is 80 % larger than the jump heights of sensor two and three.
A magnetic-force microscope has been used to study the domain pattern of the permalloy structures in spin-valve configuration. In Fig. 3.10 MFM images of the double electrode upon sensor two are depicted. The measurements are performed at room temperature with an external magnetic field applied along the easy axes of the electrodes. The magnetic field strength has been varied between ± 2 mT in steps of 0.33 mT. The sequence of MFM images shows the magnetization changes of both electrodes within a complete hysteresis.
The dark and light contrast indicates the orientation of the stray field which is detected by the MFM tip above the sample surface. Both ends of the electrodes show a particularly strong contrast. The grey areas can be interpreted as single domains. The small electrode always changes the magnetization direction first (b, d). Thus, by means of an external magnetic field the magnetization of the double electrode can be aligned to a parallel and anti-parallel configuration. This property of the double electrode is essentially for their applications in spin-valve devices.

3.4. Magnetic transmission x-ray microscopy of interacting iron elements

In the following article the influence of dipole interaction on square lattice arrays of thin microelements of Fe is measured with magnetic transmission x-ray microscopy for varying inter-element distances. For comparison isolated elements are prepared on the same sample. The magnetostatic field caused by inter-element interaction leads to a substantial stabilization of the elements in the center of the array comparable to the magnetization process previously found by numerical solution of the Landau-Lifshitz equation for magnetic dot arrays. Micromagnetic simulations reveal that for high field strengths the dipolar interaction is collinear with the external field while in the low-field regime the stray fields have significant perpendicular components leading to a complex reversal mechanism.

Publication 3

J. Appl. Phys. **99**, 08H301 (2006)

JOURNAL OF APPLIED PHYSICS **99**, 08H301 (2006)

Real space observation of dipolar interaction in arrays of Fe microelements

Markus Bolte, René Eiselt, and Guido Meier[a)]
Institut für Angewandte Physik und Zentrum für Mikrostrukturforschung, Universität Hamburg, Jungiusstrasse 11, 20355 Hamburg, Germany

Dong-Hyun Kim and Peter Fischer
Center for X-Ray Optics, Lawrence Berkeley National Lab, 1 Cyclotron Road, Mail Stop 2R0400, Berkeley, California 94720

(Presented on 2 November 2005; published online 17 April 2006)

Square lattice arrays of thin microelements of Fe are investigated by magnetic transmission x-ray microscopy. The influence of dipole interaction is analyzed by varying the interelement distance. For comparison isolated elements are prepared on the same sample. The magnetostatic field caused by interelement interaction leads to a substantial stabilization of the elements in the center of the array comparable to the magnetization process previously found by numerical solution of the Landau-Lifshitz equation for magnetic dot arrays. Micromagnetic simulations show that for high field strengths the dipolar interaction is collinear with the external field while in the low-field regime the strayfields have significant perpendicular components leading to a complex reversal mechanism. © *2006 American Institute of Physics*. [DOI: 10.1063/1.2158387]

I. INTRODUCTION

Arrays of magnetic micro- and nanoelements are the basis for magnetic data storage and magnetic memory applications.[1–3] Dipolar interactions in dense arrays are important to consider because the magnetic properties such as magnetization process, remanence, and coercive field can be significantly different from those of noninteracting systems.[4–6] Arrays of magnetic elements exhibiting dipolar interactions have been studied theoretically[4–8] and experimentally.[1,3,9,10] Dipole interactions significantly affect the high-frequency response and the reversal dynamics of coupled arrays.[11] A nontrivial variation of the switching time as a function of the packing density is predicted. Because of its relevance for magnetic random access memory cells, it is interesting to use time resolved microscopy techniques to measure directly the expected influence on the reversal dynamics.

Here we focus on the real space observation of the effects of dipolar interaction on the static magnetic properties and the magnetization process in arrays of Fe microelements.

II. SAMPLE PREPARATION AND MEASUREMENT SETUP

We have prepared arrays of Fe microelements on Si_3N_4 membranes consisting of 5 nm Al as a seed layer and 20 nm Fe as a ferromagnetic layer. A 3 nm thick Al cap serves as protection. The microelements are defined by electron-beam lithography, electron-beam evaporation of the Fe layer at a rate of 0.1 nm/s with a base pressure in the 10^{-8} mbar range, and lift-off processing.

We use magnetic transmission x-ray microscopy (MTXM) in external magnetic fields of up to ±100 mT.[12] MTXM is an excellent tool to investigate the fragile and complex dipolar magnetic interaction in arrays of micro- and nanostructured elements. It allows noninvasive exploration of magnetic reversal within large arrays due to the full-field scope with a high spatial resolution.[13,14]

The MTXM images taken at the Fe L_3 absorption edge at a photon energy of 706 eV exhibit a contrast reversal from dark to light when the external field is reversed from +100 to −100 mT. With a proper normalization of each image to the saturated images, MTXM can be used as a highly sensitive local magnetometer. To achieve this, the mean value of the gray scale data in the magnetic part of an image is offset by the corresponding mean value of the nonmagnetic neighborhood and normalized with it. By this method, possible spatial fluctuations of the synchrotron light intensity are significantly reduced and hysteresis loops of a single microelement can be measured. The magnetic moment of one Fe microelement of 1.36×10^{-13} A m^2=0.136 nemu illustrates the ultrahigh sensitivity.

III. RESULTS AND DISCUSSION

Figure 1 shows representative images of four arrays with different interelement spacings at equal external magnetic field. The field is applied in the horizontal direction indicated by the arrow. The dichroic contrast measures the projection of the local magnetization onto the photon propagation direction; i.e., the gray scale of the MTXM image is proportional to their scalar product. For in-plane magnetizations as in the present case, the sample has to be tilted so as to obtain a nonvanishing projection.[15] Areas of magnetization in Fig. 1 pointing to the right appear white, while the ones in the opposite direction appear dark gray. Domains in the perpendicular, i.e., in the vertical direction in Fig. 1, exhibit an intermediate gray value. An example of a magnetization state of a single element interpreted using this gray scale is given in the inset of Fig. 1(d).

Before discussing the hysteresis loops inferred from the sequences of images we estimate the interelement spacing,

a)Electronic mail: meier@physnet.uni-hamburg.de

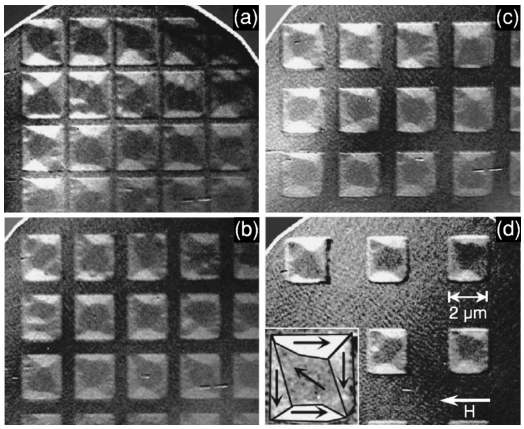

FIG. 1. MTXM images of arrays of Fe microelements with (a) 200 nm, (b) 600 nm, (c) 800 nm, and (d) 2000 nm interelement spacing in a magnetic field of $\mu_0 H = +8.7$ mT (state A in Fig. 3). Its direction is indicated by the arrow. The inset in (d) is an enlarged zoom of one microelement of this array with the magnetization indicated by arrows.

where significant dipolar interaction is expected. For this, an isolated Fe microelement and its strayfield was simulated. We use the object oriented micromagnetic framework (OOMMF)[16] with standard iron parameters (saturation magnetization 1.700 kA/m, anisotropy constant 48.0 kJ/m^3, exchange constant 21×10^{-12} J/m), and a cell size of 5 nm in each direction. The evaporation process yields polycrystalline films with virtually no texture, thus justifying the choice of a random distribution of anisotropy axes in the simulations. Two representative results are shown in Fig. 2, where the magnetization of the microelement is plotted on top of the strayfield distribution. Although the exact magnetization state as measured in the nearly noninteracting elements of the array in Fig. 1(d) could not be reproduced by the micromagnetic simulation, it is worth calculating the strayfields. Significant field strengths of 16 and 6.5 mT at distances of 200 and 400 nm, respectively, are obtained. While at saturation the strayfield is almost completely aligned in the direction of the external field [see Fig. 2(b)], it has significant perpendicular components at zero applied field [see Fig. 2(a)]. This will cause a complex interaction while reversing the magnetization of an array of such elements. Although there is a long tradition in using computer simulations to

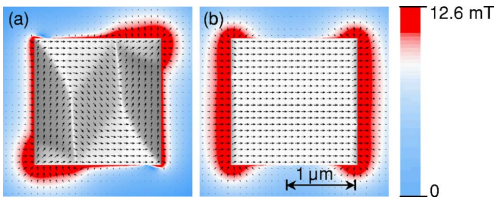

FIG. 2. (Color online) Micromagnetic simulation of the magnetization and the strayfield of an isolated element at zero field (a) and next to saturation at 100 mT (b). The color scale indicates the strength of the strayfield outside the element. A field strength of more than 10 mT is present up to a distance of 250 nm indicated by the sharp transition from red to white.

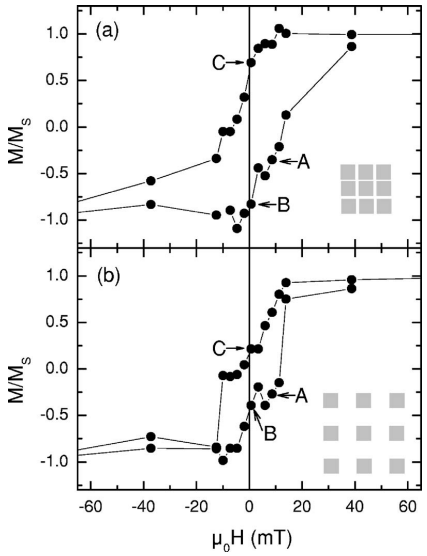

FIG. 3. Normalized hysteresis curves of the arrays determined from MTXM images at different fields for an interelement distance of (a) 200 nm and (b) 2000 nm.

understand the magnetic dipole interaction problem,[7] the simulation of arrays of real microelements is even today a time- and resource-consuming task. Often the elements of the array are assumed to be uniformly magnetized. If essential features of the magnetic ordering are governed by the net magnetic moment of the particle this is a reasonable assumption.[4] However, in the present case we can merely expect a qualitative description of the magnetization process by such an approach.

In the following, we discuss hysteresis loops inferred from MTXM images like the ones in Fig. 1 that were taken at 29 magnetic fields in the ±100 mT range. The hysteresis curves of the arrays with interelement spacings of 200 and 2000 nm are shown in Fig. 3. Magnetization state A corresponds to the images in Fig. 1. It is obvious that the hysteresis loops widen as the interelement distance is decreased. This is due to the dipolar coupling and is theoretically predicted.[4–6]

For a more quantitative interpretation it is interesting to study the dependence of the dipolar interaction characterized by the interelement distance on the reduced remanence M_R/M_S and the reduced coercive field H_C/M_S. The values can either be directly read off the raw data or deduced from sigmoidal fits. Results are shown in Fig. 4. The reduced coercive field H_C/M_R goes up steadily when dipolar interaction becomes stronger. This implies that a substantial additional field is required to change the ferromagnetic order of the magnetic moments. The reduction of coercivity with decreasing interaction strength is confirmed by micromagnetic simulations of interacting chains of Permalloy™ elements.[6]

A remanence $M_R \approx 0.6 M_s$ is measured when the dipolar interaction is strong; i.e., at a spacing of 200 nm. The remanence sharply drops as the interelement distance is increased

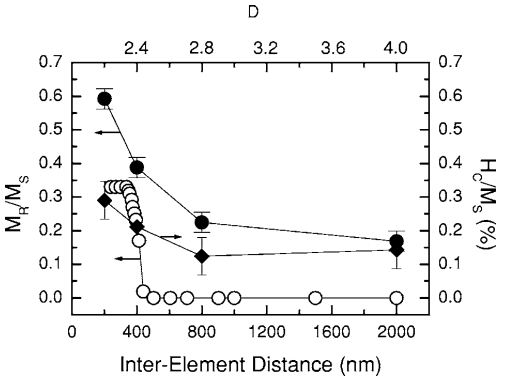

FIG. 4. Measured reduced remanent magnetizations (solid circles) and coercive fields (solid diamonds) of the arrays versus interelement distance. Open symbols are reduced remanences taken from numerical calculations by Zhang *et al.* (see Ref. 5). Lines are guides to the eye.

(spacing $\geqslant$400 nm). This is in good qualitative agreement with the results of Zhang *et al.*[5] Using their notation $D=a/R$ with the lattice constant a, the element radius R, and by describing the size of the microelements by the radius R, our arrays range from $D=2.2$ to $D=4$. Thus, a direct comparison of the reduced remanences of our arrays with this theory is possible. They agree qualitatively well as can be seen in Fig. 4. It is clear that a quantitative agreement cannot be expected because the model describes arrays of interacting single-domain dots. However, the sharp decrease of the reduced remanence is seen in the calculation as well as in our experiment. The offset in the measured remanence in comparison to the calculated one is presumably caused by the additional shape anisotropy of our Fe microelements. When subtracting the anisotropy offset from the experimental remanences, an almost perfect quantitative agreement is obtained.

The high value of the reduced remanence at a spacing of 200 nm represents the tendency of the magnetization to stabilize itself at zero field. This effect can be observed directly in the images shown in Fig. 5, where magnetization states next to zero field are shown. They correspond to states B and C of Fig. 3. In case of stronger interaction, i.e., for an interelement spacing of 200 nm, an almost saturated state is kept [see Figs. 5(a) and 5(c)], while in case of nearly isolated elements irreversible magnetization processes have already switched significant parts of the element's magnetization [see Figs. 5(b) and 5(d)].

IV. CONCLUSION AND OUTLOOK

With MTXM we have directly observed the influence of dipolar interaction on dense arrays of Fe microelements. The magnetization processes are in qualitative agreement with the theoretical predictions. Arrays of increased density and reduced interelement spacing will be accessible with a new type of zone plates.[17] Future time-resolved investigations of

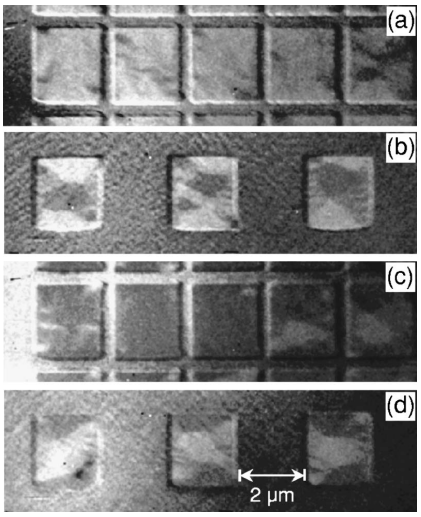

FIG. 5. Magnetization states next to zero applied field. State B in the upward sweep of the array with an interelement distance of (a) 200 nm and (b) 2000 nm. (c) and (d) corresponding magnetization in the down sweep (state C, see Fig. 3).

nanostructured magnetic arrays prepared on strip lines with MTXM in the pump-and-probe mode are very tempting and of great interest for fast magnetic memories.

ACKNOWLEDGMENTS

We would like to thank Ulrich Merkt for valuable discussions. Financial support of the Deutsche Forschungsgemeinschaft via the Sonderforschungsbereich 508 "Quantenmaterialien" and the Sonderforschungsbereich 668 ″Magnetismus vom Einzelatom zur Nanostruktur″ is gratefully acknowledged.

[1]D. W. Abraham and Y. Lu, J. Appl. Phys. **98**, 023902 (2005).
[2]S. Chou, IEEE Trans. Magn. **85**, 652 (1997).
[3]C. A. Ross *et al.*, J. Appl. Phys. **91**, 6848 (2002).
[4]R. L. Stamps and R. E. Camley, Phys. Rev. B **60**, 11694 (1999).
[5]L. F. Zhang, C. Xua, P. M. Hui, and Y. Q. Ma, J. Appl. Phys. **97**, 103912 (2005).
[6]P. Wadhwa and M. B. A. Jalil, J. Magn. Magn. Mater. **294**, 83 (2005).
[7]R. Moskowitz and E. Della Torre, J. Appl. Phys. **38**, 1007 (1967).
[8]D. Süß, T. Schrefl, J. Fidler, and J. Chapman, J. Magn. Magn. Mater. **196–197**, 617 (1999).
[9]G. Meier, M. Kleiber, D. Grundler, D. Heitmann, and R. Wiesendanger, Appl. Phys. Lett. **72**, 2168 (1998).
[10]D. Grundler, G. Meier, K.-B. Broocks, C. Heyn, and D. Heitmann, J. Appl. Phys. **85**, 6175 (1999).
[11]R. L. Stamps and R. E. Camley, Phys. Rev. B **60**, 12264 (1999).
[12]P. Fischer, Curr. Opin. Solid State Mater. Sci. **7**, 173 (2003).
[13]G. Meier, R. Eiselt, M. Bolte, M. Barthelmess, T. Eimüller, and P. Fischer, Appl. Phys. Lett. **85**, 1193 (2004).
[14]M. Bolte, R. Eiselt, T. Eimüller, P. Fischer, and G. Meier, J. Magn. Magn. Mater. **290–291**, 723 (2005).
[15]P. Fischer, T. Eimüller, G. Schütz, M. Köhler, G. Bayreuther, G. Denbeaux, and D. Attwood, J. Appl. Phys. **89**, 7159 (2001).
[16]M. Donahue and D. Porter, Interagency Report NISTIR 6376, National Institute of Standards and Technology, Gaithersburg, MD, Sept. 1999.
[17]W. Chao, B. Harteneck, J. Liddle, E. Anderson, and D. Attwood, Nature (London) **435**, 1210 (2005).

3.5. Comparison of domain imaging techniques

The following two articles describe results on magnetostatically coupled ferromagnetic electrodes. Full field magnetic transmission x-ray microscopy and magnetic-force microscopy in external fields are compared for identical samples. The images taken with both techniques are in good agreement. Evidence for a stray-field induced coupling of the domain structure in adjacent permalloy rectangles is found. With respect to transport in hybrid devices the domain structure at the edges of ferromagnetic electrodes are of utmost importance. X-ray microscopy is the technique of choice to observe rather subtle effects of dipolar interaction, which have been predicted by micromagnetic simulations [74] and observed with non-invasive Hall micromagnetometry [89]. With magnetic-force microscopy no such stray field coupling could be observed. Evidently, the stray field of typically 50 mT of the MFM tip [90] deteriorates the domain structure of the electrodes.

Publication 4

Appl. Phys. Lett. **85**, 1193 (2004)

APPLIED PHYSICS LETTERS VOLUME 85, NUMBER 7 16 AUGUST 2004

Comparative study of magnetization reversal in isolated and strayfield coupled microcontacts

Guido Meier,[a] René Eiselt, Markus Bolte, and Miriam Barthelmeß
Institut für Angewandte Physik und Zentrum für Mikrostrukturforschung, Universität Hamburg, Jungiusstrasse 11, 20355 Hamburg (Germany)

Thomas Eimüller and Peter Fischer
Max-Planck-Institut für Metallforschung, Heisenbergstrasse 3, 70569 Stuttgart (Germany)

(Received 8 March 2004; accepted 7 June 2004)

Ferromagnetic microcontacts are key components for future spintronic devices in full metal as well as in hybrid ferromagnet/semiconductor systems. Control of the micromagnetic behavior and especially the reversal process is crucial for the functionality of such devices. We have prepared isolated and strayfield coupled micron sized rectangular Ni/Fe double layer contacts on silicon nitride membranes. High-resolution magnetic microscopy studies in external fields are performed on identical samples comparing full field magnetic transmission x-ray microscopy and magnetic-force microscopy. The results of both techniques are in good agreement. We find evidence for a strayfield-induced coupling of the domain structure in adjacent contacts in accordance with micromagnetic simulations. © *2004 American Institute of Physics*. [DOI: 10.1063/1.1777824]

Hybrid ferromagnet/semiconductor systems are discussed for spintronic applications where spin injection and transport are important.[1] It is now accepted that efficient injection of spin-polarized carriers from a ferromagnetic source contact into a semiconductor heterostructure is practicable via a Schottky or an aluminum oxide barrier.[2–4] So far, in transport experiments, external magnetic fields have been used to saturate the ferromagnetic (FM) contacts, and the magnetoresistance of such devices was measured.[5–7] However, devices like the spin transistor[8] require keeping the magnetization in a well-defined state and manipulate the spin by means of electric rather than magnetic fields. Thus, a detailed understanding of the magnetic microstructure of involved FM contacts is essential. A homogeneous magnetization in the injecting area, low strayfields, and distinct switching fields so as to adjust a defined parallel or antiparallel alignment in two contacts deposited in close proximity on the substrate are desired. These features have been studied extensively by means of Hall micromagnetometry,[9] magnetic-force microscopy (MFM),[10] and micromagnetic simulations.[11] However, the results obtained so far were not fully conclusive, e.g., the elaborate interpretation of MFM signals has to take into account a possible deterioration of the sample's magnetic structure by the strayfield of the magnetic tip.

Here, we present a study of the reversal process in magnetic microstructures of isolated and strayfield coupled contacts utilizing both full field magnetic x-ray microscopy and MFM in external magnetic fields. We compare the pros and cons of both techniques with identical samples.

MFM is a common and relatively simple imaging technique with low requirements for the sample preparation, providing a rather good spatial resolution down to 20 nm (Ref. 13) and the possibility to apply magnetic fields of up to 100 mT. The MFM signal is proportional to the strayfield above the sample or, like in the present case, to the second derivative of the perpendicular field component.[13,14] MTXM combines x-ray magnetic circular dichroism (XMCD), i.e., the dependence of the absorption of circularly polarized x-rays on the projection of the magnetization onto the photon propagation direction as magnetic contrast mechanism, with full field transmission x-ray microscopy.[15] A high lateral resolution down to 20 nm can be obtained due to Fresnel zone plates used as optical elements.[16] A unique feature of MTXM is the inherent chemical specificity, i.e., the MTXM contrast is a measure of the elemental magnetization. To study in-plane magnetization, the sample's surface has to be tilted with respect to the beam direction.[17] As a pure photon-based technique, the images can be recorded in principally unlimited external magnetic fields thus allowing a detailed study of magnetization reversal processes. The penetration depth of soft x-rays sets limits to the sample thicknesses to about 100–200 nm and requires x-ray transparent substrates.

For the comparative study, we have prepared isolated and coupled microcontacts on silicon nitride (Si_3N_4) membranes consisting of 11 nm Al as a seed layer, 30 nm Fe as the lower and 30 nm Ni as the upper FM layer. A 6 nm thick Al cap serves as protection. The contacts are defined by electron-beam lithography, *in situ* electron-beam evaporation of the two FM layers at a rate of 0.1 nm/s with a base pressure in the 10^{-8} mbar range, and lift-off processing.

Specific features of both techniques regarding the contrast mechanism are demonstrated in Fig. 1 for two microcontacts with a size of 2×2 μm^2 and 2×4 μm^2 separated by 400 nm which are in a magnetic state close to saturation at an applied magnetic field of +40 mT. Micromagnetic simulations obtained with OOMMF (Ref. 18) using the fully three-dimensional code for the deposited layer sequence with an applied field of +40 mT aligned along the short axis of the contact are shown in Fig. 1(a) proving saturation. For the iron (nickel) layer, we used a saturation magnetization of 1700 kA/m (490 kA/m), an anisotropy constant of 48.0 kJ/m^3(−5.7 kJ/m^3), an exchange constant of 21×10^{-12} J/m (9×10^{-12}J/m), and a cell size of 10 nm in each direction. The evaporation process yields polycrystalline films with virtually no texture, thus justifying the choice of a random distribution of anisotropy axes in the simulations.

[a]Electronic mail: meier@physnet.uni-hamburg.de

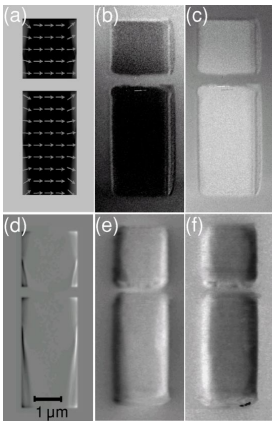

FIG. 1. 2×2 μm^2 and 2×4 μm^2 sized microcontacts deposited 400 nm apart on a Si_3N_4 membrane. The layer sequence is 11 nm Al, 30 nm Fe, 30 nm Ni, and 6 nm Al. A field of ±40 mT is applied along the short direction of the structure. (a) Simulated magnetization pattern at +40 mT. (b) Measured MTXM image at +40 mT and (c) at −40 mT. (d) Simulated MFM image at +40 mT, (e) measured MFM image at +40 mT, and (f) at −40 mT.

The MTXM images taken at the Fe L_3 absorption edge at a photon energy of 706 eV [Figs. 1(b) and 1(c)] exhibit a contrast reversal from dark to light when the external field is reversed from +40 mT [Fig. 1(b)] to −40 mT [Fig. 1(c)]. This indicates that the local magnetization vector ***m*** reverses within the external field, since the dichroic contrast measures the projection of ***m*** onto the photon propagation direction. The corresponding MFM images [Figs. 1(e) and 1(f)] are recorded at a lift-scan height of 60 nm and at the same external field strength of ±40 mT, demonstrating the more complex signal of MFM. Basically, strong strayfields at the edges correspond to the north and south poles of the saturated micromagnet and appear as dark and bright regions. By switching the magnetization bright and dark areas swap their positions indicating the reversal. With the simulated magnetization pattern in Fig. 1(a) as input, we have calculated the corresponding MFM signal for the present mode of operation [see Fig. 1(d)]. As a result of the patterning process, the shapes show deviations from perfect rectangles and the two ferromagnetic layers are not perfectly aligned. Interestingly, the irregular shape seen in the MTXM images does not show up in the MFM data. At this point, it should be mentioned that the element specificity of MTXM provides a signal from the Fe layer solely, whereas the MFM signal does not distinguish between the individual layers. Because of strong parallel coupling of the two ferromagnetic layers within the observed field range of ±40 mT a direct comparison of both techniques is justified also for nonsaturated states.

The magnetization reversal of an isolated 2×2 μm^2 Ni/Fe double-layer element is displayed in Fig. 2. It shows a sequence of images comparing MFM and MTXM data at equal strength and direction of the applied magnetic field. Excellent agreement is obtained when considering the specific detection features of the two techniques explained above. At zero field, a Landau pattern with four domains is observed with both techniques [see Figs. 2(c) and 2(d)] in agreement with the micromagnetic simulation at remanence shown in Fig. 2(a). The nonperfect shape of the element observed with both techniques seems to have a slight impact

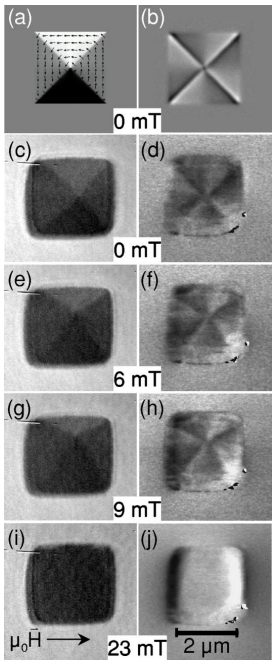

FIG. 2. Isolated 2×2 μm^2 sized microcontact. From the simulated magnetization pattern in (a) an MFM image is calculated (b) assuming a distance of 100 nm between detecting dipole and sample reasonable for the experimental lift-scan height of 60 nm (see Ref. 16). Measured MTXM images for applied fields of (c) 0 mT, (e) 6 mT, (g) 9 mT, and (i) 23 mT (saturated). The corresponding MFM images are shown in (d), (f), (h), and (j). The direction of the applied field is indicated by an arrow.

on the Landau pattern seen with MTXM yielding a nonsymmetric shift of the vortex core. The sense of rotation in the closure structure is counterclockwise since the dark domain is enlarged at the cost of the bright one on top when the magnetic field is increased in the direction of the arrow in Fig. 2(i). The corresponding sequence of MFM images in Figs. 2(d), 2(f), 2(h), and 2(j) also supports the Landau pattern. Here, in each of the four domains, a smooth progression from bright to dark is observed. At the domain walls, an abrupt change in contrast appears. This is expected as in this region the strayfield and its derivatives in the perpendicular direction are enhanced due to volume and surface charges within the walls. At the present sample thickness a mixed wall type is realized being rather of asymmetric Bloch than of Néel type.[13,16] The simulated MFM image in Fig. 2(b) is in good agreement with the measurement.

By applying a magnetic field, the vortex core of the Landau pattern is shifted in the vertical direction concomitant to the increase and decrease of the parallel and antiparallel domains. With both techniques, a field as strong as 23 mT is required to perform the irreversible switching to the fully saturated state. We conclude that in the MFM measurements, the tip–sample interaction is not strong enough to change the micromagnetic behavior of the contact significantly. This is generally not the case.[12,19] In Fig. 2, the rather weak influence of the tip is underlined by the good agreement of the position of the vortex at equal field strengths recorded with both techniques.

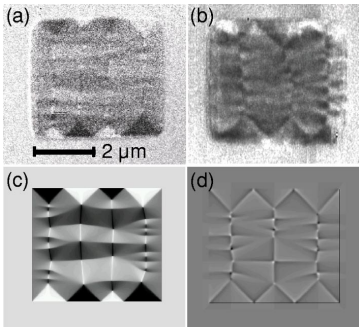

FIG. 3. (a) MTXM and (b) MFM image of an isolated 4×3.5 μm^2 microcontact at remanence. In (c) and (d), simulated images are shown. (c) Micromagnetic simulation of (a) indicating a perfect agreement with the MTXM signal. (d) Simulated MFM image obtained from a modified OOMMF simulation (see Ref. 16) in concordance with the MFM image (b).

A comparison of more complex magnetic microstructures at remanence is presented in Fig. 3 with a 4×3.5 μm^2 sized element. A multidomain structure with several closure domains on the upper and the lower sample edges is nicely seen with both techniques. Cross-tie walls divide the vertically aligned domains in the inner region and a typical checker boardlike pattern can be seen in the MFM signal corresponding to dark and bright regions in the MTXM image. Interestingly, the MTXM image indicates 13 domains while the MFM image shows only 10 [Figs. 3(a) and 3(b)]. This is presumably caused by impurities which pin the local magnetization. To interpret this finding, micromagnetic simulations by the OOMMF code have been performed in order to calculate the magnetic energies of the two patterns depicted in Figs. 3(c) and 3(d). Accordingly, a difference in the total energy of 12% between the two patterns has been obtained.

Magnetic interactions of closely coupled micromagnets are of utmost importance with regard to spintronic applications. To observe these rather subtle effects, which have been predicted by micromagnetic simulations (Barthelmeß *et al.*[10]) and observed with non-invasive Hall micromagnetometry (Meier *et al.*[9]) we find that MTXM is the technique of choice. It allows a direct observation of the magnetostatic coupling. Figure 4 shows the structure of Fig. 1 in the low field regime. It exhibits a symmetric magnetic coupling in the closure domains of the upper and lower contact. In the 400 nm gap between the contacts micromagnetic simulations yield strayfield strengths of 10 mT at the edge and 0.6 mT in the center. The parallel coupling is formed by both this strong interaction and by pinned magnetizations. With MFM no such strayfield coupling could be observed. This can be attributed to the tip's dipole field of about 50 mT (Garcia *et al.*[19]) which is sufficient to deteriorate the magnetic microstructure. The simulation also reveals that the strayfield energy is reduced by 32%, i.e., 6.8×10^{-16} J, compared to being calculated for separated contacts. The influence of the interaction amounts to 10% of the total energy (6.2×10^{-15} J) and contributes to the significant domain distortion observed with MTXM.

In conclusion, we have investigated the magnetic microstructure of double-layer Ni/Fe microcontacts prepared on thin membranes by high-resolution MFM and MTXM. The

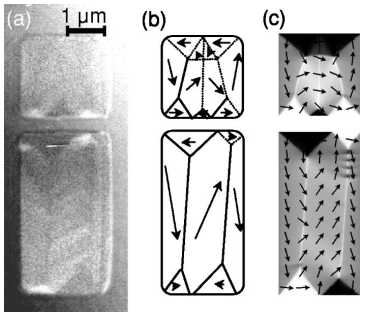

FIG. 4. Magnetic domain structures of the microcontacts shown in Fig. 1 in a field of 8.0 mT applied along the short axis. (a) MTXM image indicating a symmetric coupling between the closure domains in the upper and lower contacts. (b) Sketch of the domain-wall positions. The vertical solid lines in the lower structure indicate cross-tie walls. Dashed lines are to guide the eye in regions of weak signal. (c) Simulated magnetization pattern.

domain patterns observed with both techniques are in good agreement at remanence as well as in externally applied magnetic fields. Magnetostatic interaction between microcontacts in close proximity to each other could be observed solely by MTXM. Our results have a strong impact for future developments of coupled micro- and nanocontacts for spintronic applications.

The authors would like to thank U. Merkt for inspiring discussions and J. Gancarz for technical assistance. Financial support of the Deutsche Forschungsgemeinschaft via the Sonderforschungsbereich 508 "Quantenmaterialien" as well as the Graduiertenkolleg "Physik nanostrukturierter Festkörper" is gratefully acknowledged.

[1] S. A. Wolf, D. D. Awschalom, R. A. Buhrman, J. M. Daughton, S. von Molnár, M. L. Roukes, A. Y. Chtchelkanova, and D. M. Treger, Science **294**, 1488 (2001).
[2] A. T. Hanbicki, O. M. J. van't Erve, R. Magno, G. Kioseoglou, C. H. Li, B. T. Jonker, G. Itskos, R. Mallory, M. Yasar, and A. Petrou, Appl. Phys. Lett. **82**, 4092 (2003).
[3] E. I. Rashba, Phys. Rev. B **62**, R16267 (2000).
[4] C.-M. Hu and T. Matsuyama, Phys. Rev. Lett. **87**, 066803 (2001).
[5] F. J. Jedema, H. B. Heersche, A. T. Filip, J. J.A. Baselmans, and B. J. van Wees, Nature (London) **416**, 713 (2002).
[6] C.-M. Hu, J. Nitta, A. Jensen, J. B. Hansen, and H. Takayanagi, Phys. Rev. B **63**, 125333 (2001).
[7] G. Meier, T. Matsuyama, and U. Merkt, Phys. Rev. B **65**, 125327 (2002).
[8] S. Datta and B. Das, Appl. Phys. Lett. **56**, 665 (1990).
[9] G. Meier, R. Eiselt, and M. Halverscheid, J. Appl. Phys. **92**, 7296 (2002).
[10] M. Barthelmeß, A. Thieme, R. Eiselt, and G. Meier, J. Appl. Phys. **93**, 8400 (2003).
[11] G. Meier and T. Matsuyama, Appl. Phys. Lett. **76**, 1315 (2000).
[12] A. Hubert and R. Schäfer, *Magnetic Domains - The Analysis of Magnetic Microstructures* (Springer, Berlin, 1998).
[13] J. Lohau, S. Kirsch, A. Carl, G. Dumpich, and E. F. Wassermann, J. Appl. Phys. **86**, 3410 (1999).
[14] M. Barthelmeß, C. Pels, A. Thieme, and G. Meier, J. Appl. Phys. **95**, 5641 (2004).
[15] P. Fischer, T. Eimüller, G. Schütz, G. Denbeaux, A. Lucero, L. Johnson, D. Attwood, S. Tsunashima, M. Kumazawa, N. Takagi, M. Köhler, and G. Bayreuther, Rev. Sci. Instrum. **72**, 2322 (2001).
[16] W. Chao, E. Anderson, G. Denbeaux, B. Harteneck, J. A. Liddle, D. Olynick, A. L. Pearson, F. Salmassi, C. Song, and D. Attwood, Opt. Lett. **28**, 2019 (2003).
[17] P. Fischer, T. Eimüller, G. Schütz, M. Köhler, G. Bayreuther, G. Denbeaux, and D. Attwood, J. Appl. Phys. **89**, 7159 (2001).
[18] OOMMF, Object oriented micromagnetic framework, http://math.nist.gov/oommf
[19] J. M. García, A. Thiaville, J. Miltat, K. J. Kirk, J. N. Chapman, and F. Alouges, Appl. Phys. Lett. **79**, 656 (2001).

Publication 5

J. Magn. Magn. Mater. **290-291**, 723 (2005)

Available online at www.sciencedirect.com
SCIENCE DIRECT®
ELSEVIER
Journal of Magnetism and Magnetic Materials 290–291 (2005) 723–726
Journal of magnetism and magnetic materials
www.elsevier.com/locate/jmmm

Micromagnetic simulation as a bridge between magnetic-force and magnetic-transmission X-ray microscopy

Markus Bolte[a,*], René Eiselt[a], Thomas Eimüller[b], Peter Fischer[c], Guido Meier[a]

[a]*Institut für Angewandte Physik und Zentrum für Mikrostrukturforschung, Universität Hamburg, Jungiusstrasse 11, Hamburg 20355, Germany*
[b]*Max-Planck Institut für Metallforschung, Heisenbergstrasse 3, Stuttgart 70569, Germany*
[c]*Center for X-ray Optics, Lawrence Berkeley National Lab, 1 Cyclotron Road, Mail Stop 2R0400, Berkeley, CA 94720, USA*

Available online 8 December 2004

Abstract

Domain imaging techniques are used to analyze the micromagnetic behavior of microelements applied in spin-transport devices. Micromagnetic simulations enable direct comparison of the experimental results and give additional information which is not directly accessible experimentally. As a case study we investigate the stray-field interaction of microelements prepared on thin Si_3N_4 membranes with magnetic-transmission X-ray microscopy and magnetic-force microscopy. Micromagnetic simulations yield internal parameters such as local stray fields and total magnetic energy. Values for the strength of the stray-field interaction between two microelements of several milli Tesla are deduced. Results also show that pinned magnetizations can explain the magnetization patterns observed in the experiments.

PACS: 68.37.Rt; 68.37.Yz; 75.60.Ch; 75.60.Jk

Keywords: X-ray dichroism; Magnetic-force microscopy; Micromagnetic calculation; Domain pattern; Domain-wall pinning; Stray field

1. Introduction

Ferromagnetic microelements are required in full metal as well as in semiconductor/metal hybrid spin-transport devices. Domain imaging techniques have been used extensively to deepen the understanding of the fundamental principles in ferromagnetic nanostructures and also to optimize micro- and nanoelements in magnetoelectronic devices. Among the commonly used techniques are Hall-micromagnetometry [1], magnetic-force microscopy (MFM) [2], the use of the magneto-optical Kerr-effect (MOKE) [3], and magnetic-transmission X-ray microscopy (MTXM) [4]. Micromagnetic simulations have matured into a powerful tool of computing complex problems from basic thermodynamic considerations [5]. Current codes are capable of simulating the dynamic magnetic behavior of three-dimensional multi-layered nanostructures with great precision. These calculations allow direct access to internal parameters of ferromagnets, such as the composition of the total magnetic energy out of its several energy terms as well as their time- and space-resolved magnetic configurations. The purpose of this paper is to show how micromagnetic simulations can

*Corresponding author. Tel.: +49 40 42838 3629; fax: +49 40 42838 3954.
E-mail address: mbolte@physik.uni-hamburg.de (M. Bolte).

0304-8853/$ - see front matter © 2004 Elsevier B.V. All rights reserved.
doi:10.1016/j.jmmm.2004.11.276

serve as a bridge between two experimental techniques, in our case MTXM and MFM.

For this comparative study we have prepared isolated and coupled microelements on silicon nitride (Si_3N_4) membranes consisting of 11 nm Al as seed layer, 30 nm Fe as lower and 30 nm Ni as top ferromagnetic layer. A 6 nm thick Al cap serves as protection. The same samples are first examined by MFM and then by MTXM. The MFM-measurements are performed at a lift-scan height of 60 nm. The signal is proportional to the second derivative of a sample's stray field, perpendicular to the surface of the sample leading to strong gray contrasts in the areas of changes in the outer stray fields, e.g. in the region of domain walls. The MTXM-signal, on the other hand, corresponds to the scalar product of the transmitting X-ray beam with the magnetization of a ferromagnet, showing areas of homogeneous gray shades for the regions of a ferromagnet having the same magnetization, i.e. domains. Thus the one technique (MFM) best resolves the domain walls while the other shows the domains themselves. Therefore, a direct comparison is not intuitively possible. Micromagnetic simulations can help to bridge the gap between these techniques. We have extended the open source simulation code OOMMF supplied by the National Institute for Standards and Technology (NIST) [6] to produce images alike those measured by magnetic-force microscopy. Methods and algorithms used for this additional code are explained in detail elsewhere [7,8].

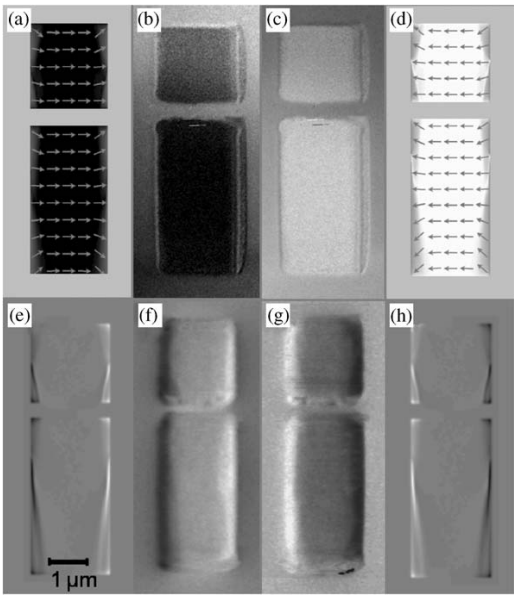

Fig. 1. $2 \times 2\,\mu m^2$ and $2 \times 4\,\mu m^2$-sized microelements deposited 400 nm apart on a Si_3N_4 membrane. A field of ± 40 mT is applied along the short direction of the structure. (a) Simulated magnetization pattern at $+40$ mT, (b) measured MTXM image at $+40$ mT and (c) at -40 mT, (d) simulated magnetization pattern at -40 mT. (e and h) simulated MFM image at ± 40 mT, respectively, (f and g) measured MFM images at ± 40 mT, respectively.

2. Results

Fig. 1 demonstrates how to compare MFM and MTXM images via the simulation code for two microelements with a size of 2×2 and $2 \times 4\,\mu m^2$ separated by 400 nm which are in a magnetic state close to saturation at an applied magnetic field of ± 40 mT along the short axis of the elements. For the iron (nickel) layer, a saturation magnetization of 1700 kA/m (490 kA/m), an anisotropy constant of 48.0 kJ/m^3 (-5.7 kJ/m^3), an exchange constant of 21×10^{-12} J/m (9×10^{-12} J/m), and a cell size of 10 nm in each direction are used. The evaporation process in the preparation of the samples yields polycrystalline films with virtually no texture [9] so that a random distribution of anisotropy axes in the simulations is justified.

Figs. 1(b) and (c) show MTXM images of the double structure in saturated states, in fields of ± 40 mT, respectively. The images, taken at the Fe L_3 absorption edge at a photon energy of 706 eV exhibit a strong contrast reversal from dark to light when the external field is reversed. This indicates that the local magnetization vector $\vec{m}$ reverses within the external field, since the dichroic contrast measures the projection of $\vec{m}$ onto the photon propagation direction. Figs. 1(a) and (d) show the corresponding micromagnetic simulations with the color coding adapted to facilitate comparison with the measurements. In the lower row the results from MFM-measurements, recorded at a lift-scan height of 60 nm and at the same external field strength of ± 40 mT, are shown in Figs. 1(e–h) the images from the extension of the existing code as described in Ref. [8]. For the computations of the MFM-images in (e) and (h) the magnetization patterns in (a) and (d) are used. The strong stray-fields at the edges correspond to north and south pole of the saturated micromagnet and appear as dark and bright regions. It should be noted, however, that the MFM signal does not distinguish between the individual layers, while MTXM provides an element-specific signal, allowing a vertical resolution of domain imaging in the case of multi-layered structures with different materials. Because of the strong parallel coupling of the iron/nickel layers within the observed field range of ± 40 mT, a direct comparison of both techniques is justified also for non-saturated states.

The methodology of using micromagnetic simulation to combine MTXM and MFM offers new insight

into the magnetic configuration of a sample not available by any of the techniques alone, especially for more complex structures as shown in detail in Ref. [10], where the energetic difference between two multi-domain structures measured with MFM and MTXM are computed. In Ref. [10], it is presumed that the relatively large difference of 12% of the total energy is caused by stray-field interaction and impurities. To validate this, we investigate the structure shown in Fig. 2.

Fig. 2(a) shows the magnetization of a $2 \times 2/2 \times 4\,\mu m^2$ double structure composed of the said Fe/Ni double layer with a 400 nm separating gap in an external field of $+8$ mT along the short axis as measured by MTXM. Multiple domains are visible. Fig. 2(b) gives the computed magnetization as derived with OOMMF when relaxing an initial state close to the one shown in (a) and assuming a pinned magnetization in the region marked with a square. It shows that the magnetic configuration cannot change much when this small area is pinned in its magnetization. (d) Shows the final state of the simulation when no pinning is assumed.

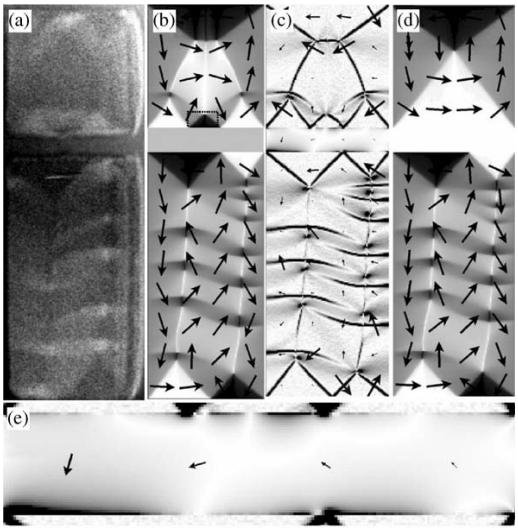

Fig. 2. (a) MTXM measurement of the microelements of Fig. 1 revealing the actual magnetization at $+8$ mT, (b) simulated magnetization with a black rectangle indicating the pinned region, (c) simulated stray field of magnetization shown in (b), gray shades represent absolute field strength along the long axis, (d) alternative simulated magnetization when no pinning is assumed, (e) enlargement of the stray-field distribution within the 400 nm gap showing interaction between the domains. The arrows represent the averaged strength and direction of magnetization or stray field of a cluster of simulation cells.

As magnetic interactions of coupled micromagnets are of great importance with regard to spintronic applications, a systematic study of the stray field interaction of such a structure is beneficial. Ref. [11] states that the stray field energy of a volume V can be derived by either integrating over V or over the whole space Ω:

$$E_d = -K_d \int_V \vec{m}(\vec{r})\vec{h}_d(\vec{r})\,dV = K_d \int_\Omega \vec{h}_d^2(\vec{r})\,dV. \quad (1)$$

OOMMF calculates the stray field energy by integrating over V. If the stray field energy of the double structure in Fig. 2 is computed separately for each contact, the sum of the energies is larger than the integral over the whole structure including the gap, because the sum is equivalent to integration over the space of the elements and twice over the complete space outside each contact. The difference between the two integrations is the stray-field energy of each micro contact at the location of the other and in the space outside both elements. It amounts to 6.8×10^{-16} J or 32% of the total stray-field energy of the double contact (1.9×10^{-15} J) or roughly 11% of its total magnetic energy (6.2×10^{-15} J). Fig. 2(c) shows the local stray-field strengths in direction of the long axis, with black representing 50 mT or higher. It reaffirms that most of the stray field is stored inside the domain walls. Fig. 2(e) shows the distribution of stray fields inside the small gap between the elements having local densities up to 50 mT, and average values across the gap of 0.6 mT (center) to 10 mT (left edge).

3. Conclusion

We have shown the comparability of MFM and MTXM images via micromagnetic simulations with adequate extensions of existing programs. We have investigated the magnetic microstructure of double-layer Ni/Fe microelements. To compare the patterns observed with MTXM with numerical simulation, "pinning" has to be assumed for the simulation. Stray-field interaction strengths are determined by applying electrodynamic principles.

Acknowledgements

We would like to thank U. Merkt for persistent support and J. Gancarz for technical assistance. Financial support of the Deutsche Forschungsgemeinschaft via the Sonderforschungsbereich 508 "Quantenmaterialien" as well as the Graduiertenkolleg "Physik nanostrukturierter Festkörper" is gratefully acknowledged.

References

[1] G. Meier, R. Eiselt, M. Halverscheid, J. Appl. Phys. 92 (2002) 7296.
[2] M. Barthelmeß, A. Thieme, R. Eiselt, G. Meier, J. Appl. Phys. 93 (2003) 8400.
[3] J.P. Park, P. Eames, D.M. Engebretson, J. Berezovsky, P.A. Crowell, Phys. Rev. B 67 (2003) 020403.
[4] P. Fischer, T. Eimüller, G. Schütz, G. Denbeaux, A. Lucero, L. Johnson, D. Attwood, S. Tsunashima, M. Kumazawa, N. Takagi, M. Köhler, G. Bayreuther, Rev. Sci. Instrum. 72 (2001) 2322.
[5] W.F. Brown Jr., Micromagnetics, Interscience Publishers, New York, 1963.
[6] M.J. Donahue, D.G. Porter, OOMMF User's Guide, Version 1.0. Interagency Report NISTIR 6376, National Institute of Standards and Technology, Gaithersburg, MD (Sept 1999).
[7] J. Lohau, S. Kirsch, A. Carl, G. Dumpich, E.F. Wassermann, J. Appl. Phys. 86 (1999) 3410.
[8] M. Barthelmeß, C. Pels, A. Thieme, G. Meier, J. Appl. Phys. 95 (2004) 5641.
[9] M. Kurfiß, R. Anton, private communication.
[10] G. Meier, R. Eiselt, M. Bolte, M. Barthelmeß, Th. Eimüller, P. Fischer, Appl. Phys. Lett. 85 (2004) 1193.
[11] D.V. Berkov, K. Ramstöck, A.D.V. Hubert, Phys. Stat. Sol. A 137 (1993) 207.

4. $CoPt_3$ nanoparticles

Nanoparticles are at the forefront of the present revolution of nanoscience and nanotechnology. They are fabricated in solution by a synthesis process in large numbers of the order of 10^{10}–10^{15} particles per milliliter with a narrow distribution of size and shape and at low cost. In particular, ferromagnetic nanoparticles are promising candidates for a wide field of applications ranging from ultra-high storage media to medical therapy like drug targeting as well as biomedical markers for diagnostics. Favored compounds are FePt and CoPt nanoparticles. These materials have a high crystalline anisotropy which is required for a good thermal stability – an important property for storage applications.
In this section a short introduction to superparamagnetism is given followed by a description of the investigation of $CoPt_3$ nanoparticles by means of Hall micromagnetometry.

4.1. Superparamagnetism

Ferromagnetic particles below a critical size consist of a single magnetic domain with a uniform magnetization at any external applied magnetic field [91]. At elevated temperatures such particles behave magnetically analogous to the Langevin paramagnetism of moment-bearing atoms. In this temperature regime the thermal energy exceeds the energy barrier E_B and provides a coherent rotation of the particle moment $\vec{m}_P$. The magnetic state of the nanoparticles in this regime is called the Langevin-type superparamagnetism. The main distinction to the Langevin paramagnetism is that the moment of a nanoparticle may

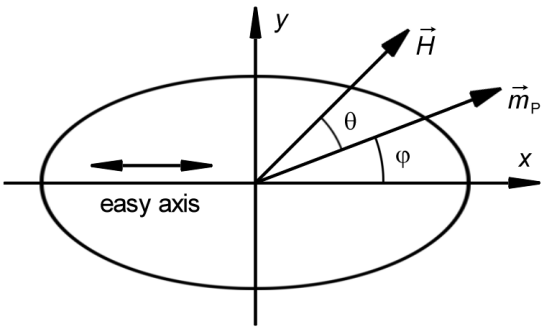

Fig. 4.1.: Magnetization $\vec{m}_P$ of a single-domain particle with shape anisotropy in the presence of an external magnetic field $\vec{H}$. Due to the minimization of the total energy the magnetization $\vec{m}_P$ is rotated against the easy axis of the particle by φ and includes an angle θ to the external magnetic field.

be 10^5 times the atomic moment.
A single-domain particle with a total magnetic moment $\vec{m}_\mathrm{P}$ and an easy axis along the x-axis is shown in Fig. 4.1. An external magnetic field $\vec{H}$ changes the direction of the magnetization. The equilibrium condition of the magnetization direction is determined by a minimum of the contributing energy terms. The Zeeman energy $-m_\mathrm{P} H \cdot \cos\theta$ considers the magnetization in the applied magnetic field. Since the particle in the example has only one easy axis the anisotropy energy consists of one term which is proportional to $\sin^2\varphi$. An ensemble of particles without anisotropy in thermodynamic equilibrium with the field will have a Boltzmann distribution of angles θ. The fraction of the total magnetization that has been aligned by the field is calculated by averaging $\cos\theta$ over the Boltzmann distribution, which yields the Langevin function

$$\mathscr{L}\left(\frac{\mu_0 H}{k_\mathrm{B} T}\right) = \coth\left(\frac{\mu_0 H}{k_\mathrm{B} T}\right) - \frac{k_\mathrm{B} T}{\mu_0 H} \quad . \tag{4.1}$$

At a critical temperature a transition of the magnetic state of the nanoparticles can be observed. The so-called blocking temperature $T < \frac{E_\mathrm{B}}{25 k_\mathrm{B}}$ which has been defined by Bean and Livingstone [91] in a seminal work specifies a dynamical crossover to the blocked superparamagnetism. In this temperature regime remanent magnetizations and coercivity appear.
The magnetic properties of large three-dimensional ensembles of superparamagnetic $CoPt_3$ nanoparticles synthesized by the organometallic route have been analyzed extensively by SQUID-magnetometry [20]. However, the magnetic analysis of a small number of such particles in restricted geometries, i. e., in two-, one-, or even zero-dimensional arrangements is an unanswered question. Hall micromagnetometry provides an excellent means for this task.

4.2. Experimental results

The $CoPt_3$ nanoparticles have been investigated with Hall sensors which have a lateral size of $3.2 \times 3.2\ \mu\mathrm{m}^2$ (see Fig. 2.6). The two-dimensional electron system of the AlGaAs heterostructure which is used to measure the magnetic stray field of the particles is located 90 nm below the surface. The characteristic parameters of the 2DES within the Hall sensors are the mobility and the electron density. These values affect the signal-to-noise ratio and the sensitivity of the sensors. The size of the sensitive area results from the width of the conducting channel. Due to the depletion region [16] the channel is approximately 200 nm smaller than the lithographically defined Hall bar.
The electron density is decisive for the measured Hall voltage and varies with temperature. To obtain an accurate interpretation of the Hall voltage as average stray field the Hall voltage and the electron density have to be investigated temperature dependent. In Fig. 4.2 measurements of the Hall voltage of sensor 3 and 4 of Fig. 2.6 are depicted between 6 K and 60 K. A constant external magnetic field of 100 mT has been applied perpendicular to the two-dimensional electron system. The magnitude of the external magnetic field

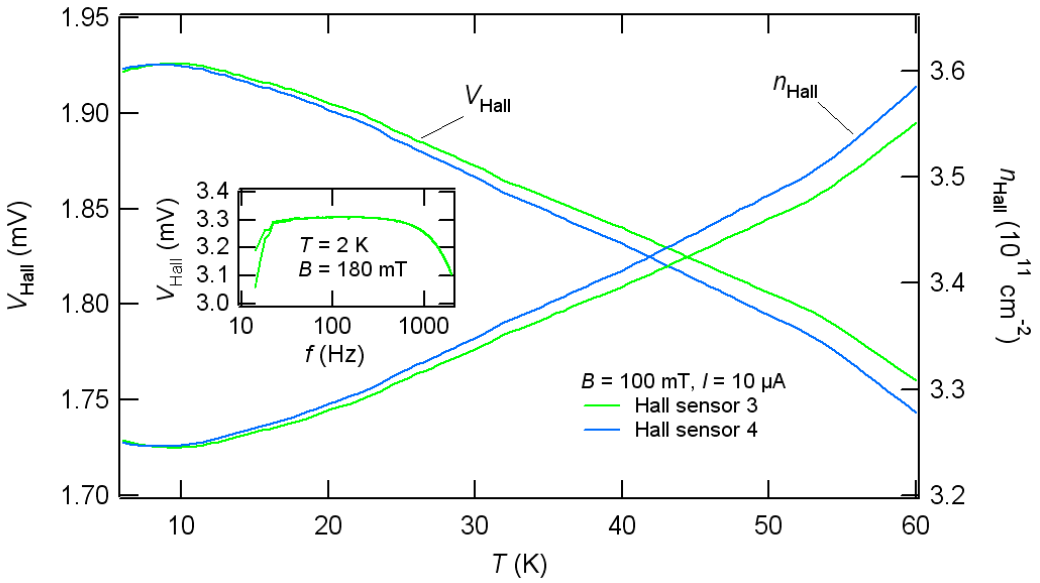

Fig. 4.2.: Temperature dependent measurement of the Hall voltage, V_{Hall}, in a constant external magnetic field of 100 mT. On the right axis the calculated electron density, n_{Hall}, is plotted. With rising temperature an increase of the electron density by almost 10 % can be seen. The inset shows the frequency dependence of the Hall voltage.

guarantees a strong Hall signal within the linear range of the Hall sensor. The influence of the $CoPt_3$ nanoparticles on the signal can be neglected in this geometry since the stray field of the particles is more than 10^3 times smaller than the external magnetic field. The right axis of Fig. 4.2 shows the calculated electron density according to Eq. (2.3). At temperatures below 60 K only a fraction of donors are thermally excited into the conduction band. With rising temperature the electron density increases as expected. The difference between the electron densities at 6 K and 60 K amounts to nearly 10 %. At temperatures around 60 K the measured Hall voltages of the two sensors show slightly different values. The deviation between the curves is presumably caused by the etching process.

In order to increase the signal-to-noise ratio the Hall measurements are performed with lock-in technique. The optimal frequency range is determine by maximizing the Hall voltage. The inset of Fig. 4.2 shows the result of a frequency dependent measurement with an external magnetic field of $B = 180$ mT at $T = 2$ K. At small frequencies below $f = 30$ Hz a decrease of the Hall signal can be observed. In the frequency range between 30 Hz and 300 Hz the Hall signal stays almost constant and is decreased for high frequencies again. To avoid resonances with measuring instruments a frequency of $f = 117.6$ Hz has been chosen for the experiments.

The deposition of the $CoPt_3$ nanoparticles has been accomplished by spin coating. They are located on the whole sample and cover the five Hall sensors which have a distance of 10 μm to each other. The solution which has been used to cover the sample consists of two particle sizes with diameters of 3 nm and 6 nm. The numerical proportion between the smaller and the larger nanoparticles is $\frac{n_{\mathrm{s}}}{n_{\mathrm{l}}} = 4.4$. In the following the measurements

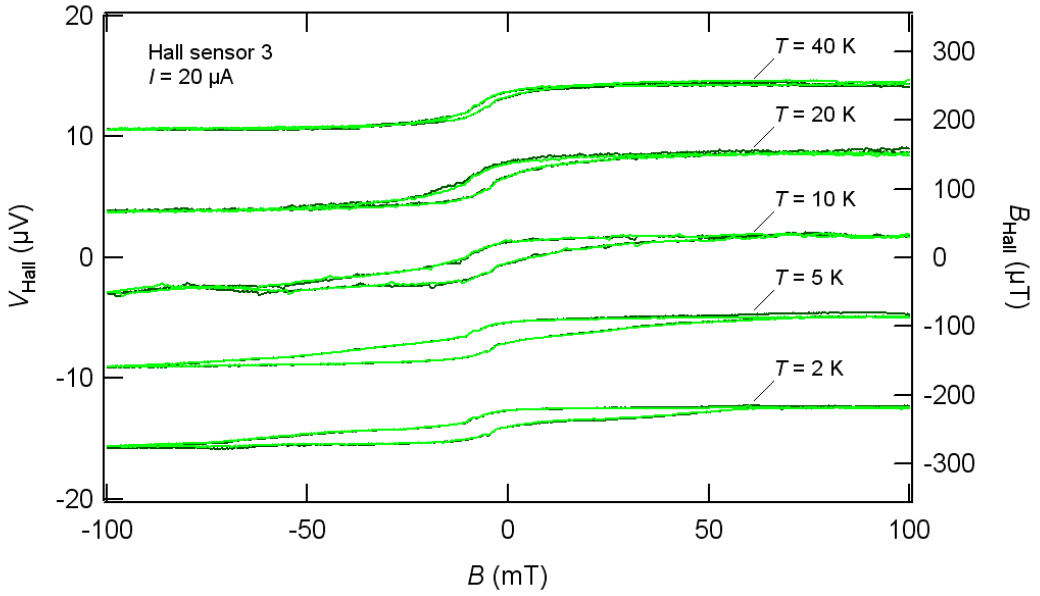

Fig. 4.3.: Hall measurements of sensor 3 in a magnetic field range of ± 100 mT. The temperature has been varied between 2 K and 60 K. Results above 40 K are not shown. A decrease of the coercivity above 20 K can be observed.

and results of sensor 3 and 4 are discussed (see Fig. 2.6). On top of both sensors the $CoPt_3$ nanoparticles are primarily arranged in a monolayer. In some areas with a higher coverage the particles are self-assembled into a hexagonal lattice. In addition to the monolayer a cluster of nanoparticles is located upon Hall sensor 4. In the left bottom area of the sensor a multilayer of particles can be seen. Within the cluster the nearest neighbor distance of the nanoparticles has a minimum value which is limited by the organic shell of the particles. The distribution can be considered as almost close-packed and is denoted as bulk state.

The stray field of the nanoparticles and the stray field interaction has been studied in dependence of an external magnetic field. After characterization of the Hall sensors the direction of the external field has been adjusted parallel to the two-dimensional electron system by a rotation of the sample holder. In parallel orientation the Hall sensors are not affected by the external field and solely detect the stray field of the particles. Thus the sensitivity of the sensors on the stray field of the particles is drastically improved.

In Fig 4.3 the Hall measurements of two subsequent sweeps of sensor 3 are shown at different temperatures. On the left axis the measured Hall voltage is plotted. On the right axis the average stray field calculated according to Eq. (2.3) is depicted. An offset has been added for clarity. With rising temperature a variation in the shape of the hysteresis loops can be observed. In Fig. 4.3 the coercivity is 9 mT at $T = 2$ K. The coercive field as well as the external magnetic field at which the ensemble of nanoparticles is saturated decreases for higher temperatures. Traces measured above 40 K finally show no hysteresis and have zero coercivity. The disappearance of the hysteresis can be identi-

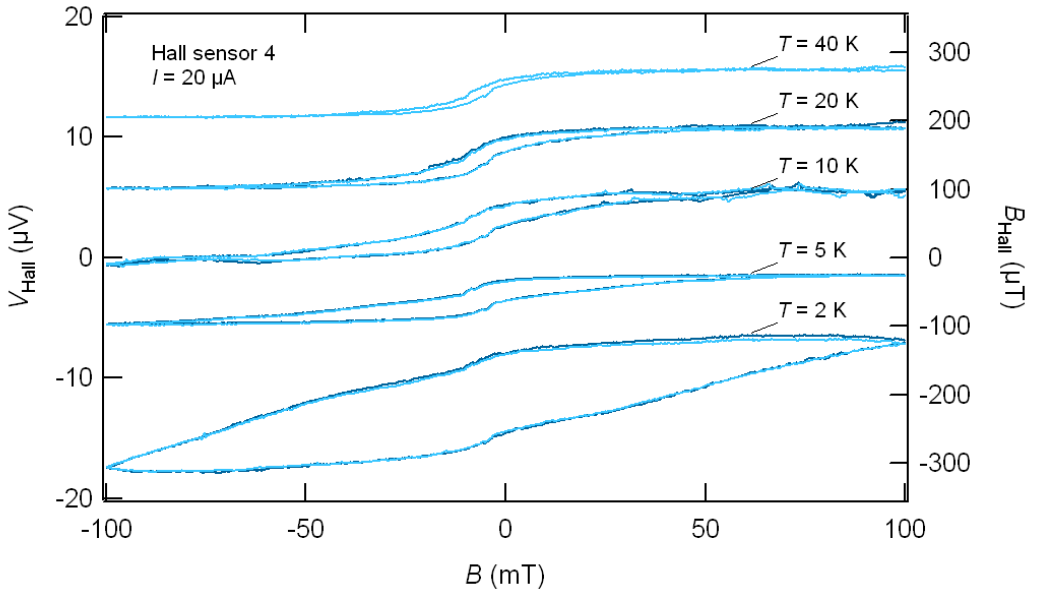

Fig. 4.4.: Stray field measurements of the $CoPt_3$ nanoparticles on top of Hall sensor 4. The hysteresis loops have predominantly the same shape and temperature dependence as sensor 3. At 2 K the two subsequent measured hysteresis curves show a strong increase of the Hall voltage due to the influence of a cluster of nanoparticles (see Fig. 2.6).

fied as transition of the larger $CoPt_3$ nanoparticles from blocked superparamagnetism to Langevin-type superparamagnetism. Due to the larger volume of the 6 nm particles the mean energy barrier E_B is higher and the blocking temperature is expected to be above the value of the 3 nm particles. The blocking temperature of $T_B = 40$ K for the 6 nm particles has also been verified by SQUID magnetometry [20]. The gradual decrease of the coercivity above 20 K can be explained by the distribution of the particle diameters. $CoPt_3$ nanoparticles with sizes larger than 6 nm are still blocked at temperatures $T > 40$ K.
The stray field of the 3 nm particles is contained in the total signal of the Hall sensor. The variation of the coercivity in the hysteresis loops between 20 K and 10 K can be attributed to the superparamagnetic transition of the 3 nm particles. The estimated range of the blocking temperature is in agreement with the expected value of $T_B = 8$ K for the 3 nm particles [20].
The measurements of Hall sensor 4 are depicted in Fig. 4.4. The hysteresis loops measured with sensor 4 above $T = 5$ K have predominantly the same shape and temperature dependence as the loops measured with sensor 3. With rising temperature the coercivity of the curves decreases. Above $T = 40$ K a hysteresis is no longer observable. This result indicates that in the temperature range down to 5 K solely the monolayer on top of sensor 4 contributes to the Hall signal. The cluster of $CoPt_3$ nanoparticles, that have been mentioned above, has no additional influence in this temperature range. At a temperature of 2 K there is a strong increase of the Hall voltage. The difference of the stray fields, B_{Hall}, at positive and negative saturation has grown from a value of 70 μT to 180 μT. The

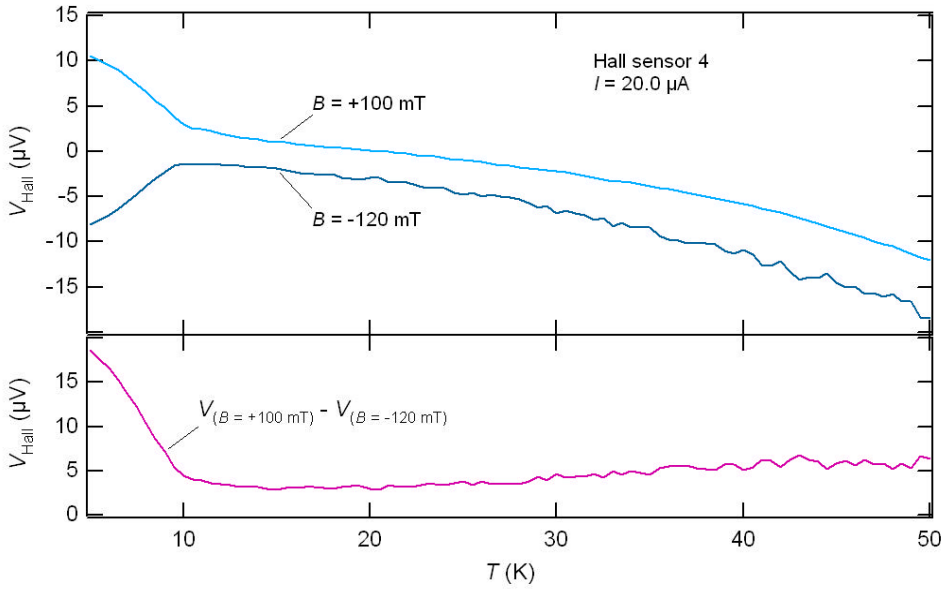

Fig. 4.5.: Temperature dependent measurement of the stray field of sensor 4 in positive (+100 mT) and negative saturation (−120 mT). The difference between the curves is plotted in the lower diagram. Below 10 K the additional influence of the cluster (see text) on the signal is visible. Above 10 K a constant saturation can be observed.

strong increase of the signal can be ascribed to an interaction of the nanoparticles.
The temperature dependence of the stray field of the nanoparticles upon sensor 4 has been investigated in constant external magnetic fields. In the upper diagram of Fig. 4.5 the measurements of the Hall voltage at $B = +100$ mT and $B = -120$ mT are shown. Considering the hysteresis loops in Fig. 4.4 the nanoparticles in these magnetic fields can be assumed to be saturated. Below 10 K an increase of the stray fields in positive saturation (+100 mT) and decrease in negative saturation (−120 mT) is observable. The result agrees with the variation of hysteresis loops at different temperatures. The lower diagram of Fig. 4.5 shows the difference of the two curves. In the temperature range above 10 K the differential signal stays almost constant. The transition between the blocked superparamagnetism and the Langevin-type superparamagnetism at $T = 40$ K occurs without a particular variation of the Hall signal. The saturation of interaction-free particles is therefore independent of the superparamagnetic state.

5. Conclusions and Outlook

Various techniques have been used to prepare ferromagnetic micro- and nanostructures. The investigation of their magnetic properties has been performed predominantly with three different methods. With magnetic-force microscopy (MFM) magnetic domain configurations are imaged in external magnetic fields. Measurements with magnetic transmission X-ray microscopy (MTXM) have been carried out at the Center of X-Ray Optics in Berkeley, USA. Hall micromagnetometry, which has been further improved in this work, has been employed as an excellent non-invasive and adaptable tool to detect local stray fields of nanostructured ferromagnets. Due to its high sensitivity and applicability in a wide temperature range from 2 K to 100 K the investigation of $CoPt_3$ nanoparticles has been possible. The combination of magnetic microscopy methods and Hall micromagnetometry on the same micro- and nanostructures has led to a comprehensive understanding of the magnetic properties, i. e. domain structures, coercive fields, blocking temperatures, switching behavior, and dipolar interaction.

Important results have been obtained for the design of spin-injecting electrodes for spintronic devices. Different electrodes suitable for spin-valves have been prepared and studied with respect to their domain configurations, magnetic stray fields between adjacent electrodes, and inter-element coupling. Also the switching fields in the temperature range from liquid helium to room temperature have been determined. By adjusting the shape of quasi-single domain electrodes the switching fields could be tuned.

Hall micromagnetometry paves the way to the magnetic characterization beyond the 100 nm limit. With stray field measurements of $CoPt_3$ nanoparticles which have a diameter of less than 10 nm the high sensitivity of the microstructured Hall sensors could be demonstrated. The study of the superparamagnetic behavior of the $CoPt_3$ nanoparticles was performed at different temperatures. Below the blocking temperature the stray field of the particles shows a hysteretic dependence on the external magnetic field. The formation in two- and three-dimensional arrangements of the $CoPt_3$ nanocrystals results in different stray fields.

In future experiments at the Center of X-Ray Optics in Berkeley, USA we aim at the simultaneous measurement of the spatially resolved magnetization with 10 nm resolution and of the anisotropic magnetoresistance. We have also planned to investigate the dynamics of ferromagnetic electrodes with a time resolution given by picosecond flashes of the Advanced Light Source synchrotron. These techniques give direct access to the measurement of current-induced magnetization dynamics. This topic is of great interest for the functionality and reliability of future magnetoresistive elements.

A. Preparation parameters

A.1. Electron-beam lithography

Parameters	**Value**	
Zeiss DSM 962		
Acceleration voltage	10 kV	
Aperture	4	
Emission current	20 μA	
Working distance (z-coordinate)	5 mm (20.000 μm)	
Write field	200×200 μm^2	2000×2000 μm^2
Magnification	360	36
Step size (Pixel)	6.1 nm (2)	30.5 nm (1)
Area dose	$60-80$ $\frac{\mu C}{cm^2}$	$70-90$ $\frac{\mu C}{cm^2}$
Beam current	14 pA	350 pA
LEO SUPRA 55		
Acceleration voltage	10 kV	
Extractor voltage	4.55 kV	
Working distance (z-coordinate)	5 mm (49.2 mm)	
Write field	200×200 μm^2	2000×2000 μm^2
Magnification	300	30
Step size (Pixel)	9.2 nm (3)	30.5 nm (1)
Area dose	$55-80$ $\frac{\mu C}{cm^2}$	$70-90$ $\frac{\mu C}{cm^2}$
Aperture size	10 μm (20 μm)	30 μm (60 μm)
Beam current	30 pA (90 pA)	220 pA (810 pA)

Table A.1.: Process parameters for the electron-beam lithography with the Zeiss DSM 962 and LEO SUPRA 55 scanning-electron microscope. The samples have been spin-coated with the electron-beam resists PMMA 600K and PMMA 950K.

A.2. Exposure patterns for Hall sensors

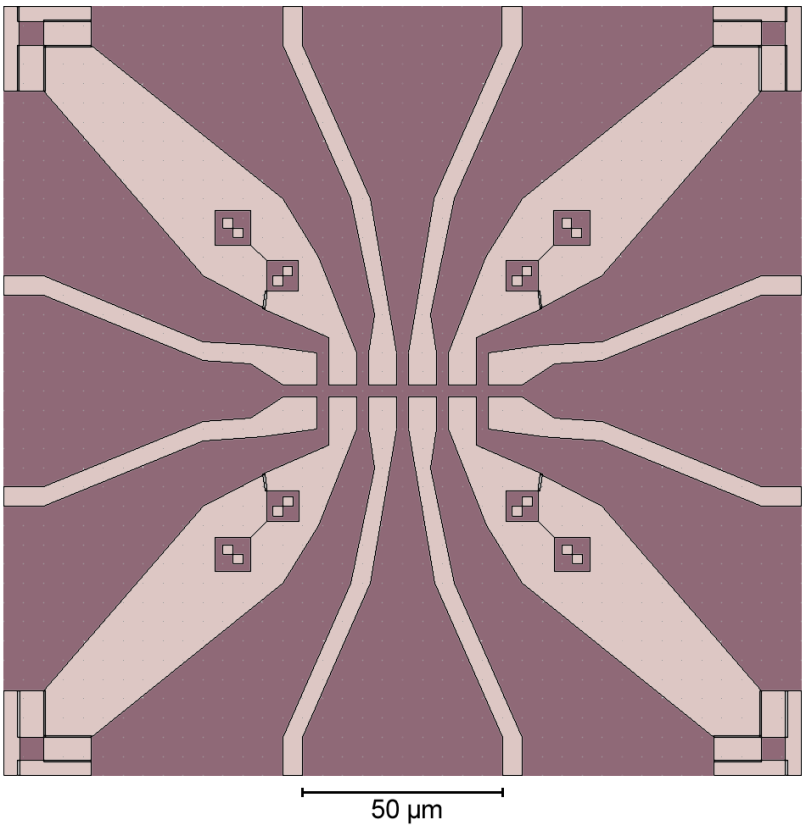

Fig. A.1.: Center area of a Hall structure. The light color indicates the etched areas of the substrate. The five Hall sensors have a distance of 10 μm and a width of 3.2 μm. Square marks close to the Hall bar are used to align the write field for subsequent exposure processes.

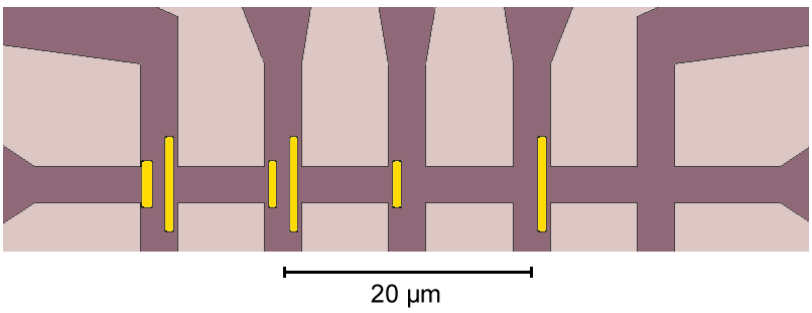

Fig. A.2.: Exposure pattern for permalloy electrodes in spin-valve configuration. The large electrodes have a size of 8.0×0.7 μm^2 and the small ones of 4.0×1.0 μm^2 and 4.0×0.7 μm^2.

Bibliography

[1] E. W. Pugh, R. A. Henle, D. L. Critchlow, and L. A. Russell, IBM J. Res. and Dev. **25**, 585–602 (1981).

[2] T. M. Maffitt, J. K. DeBrosse, J. A. Gabric, E. T. Gow, M. C. Lamorey, J. S. Parenteau, D. R. Willmott, M. A. Wood, and W. J. Gallagher, IBM J. Res. and Dev. **50**, 25 (2006).

[3] J. M. Daughton, Thin Solid Films **216**, 162–168 (1992).

[4] B. Dieny, V. S. Speriosu, S. Metin, S. S. P. Parkin, B. A. Gurney, P. Baumgart, and D. R. Wilhoit, J. Appl. Phys. **69**, 4774 (1991).

[5] S. S. P. Parkin, K. P. Roche, M. G. Samant, P. M. Rice, and R. B. Beyers, J. Appl. Phys. **85**, 5828 (1999).

[6] A. Wachowiak, J. Wiebe, M. Bode, O. Pietzsch, M. Morgenstern, and R. Wiesendanger, Science **298**, 577 (2002).

[7] A. Hubert and R. Schäfer, *Magnetic Domains. The Analysis of Magnetic Microstructures* (Springer, New York, 2000).

[8] W. Chao, B. Harteneck, J. Liddle, E. Anderson, and D. Attwood, Nature **435**, 1210 (2005).

[9] G. Prinz, Physics Today **48**, 58 (1995).

[10] R. F. C. Farrow, *Molecular Beam Epitaxy* (Noyes, New Jersey, 1995).

[11] H. Ibach and H. Lüth, *Festkörperphysik* (Spinger, Berlin, 2002).

[12] H. Morkoç, *The Technology and Physics of Molecular Beam Epitaxy* (Plenum, Berlin, 1985).

[13] D. W. Shaw, J. Electrochem. Soc. **128**, 874 (1981).

[14] B. L. Henke, E. M. Gullikson, and J. C. Davis, At. Data Nucl. Data Tables **54**, 181 (1993).

[15] C. Schierholz, *Rashba Spin-Orbit Interaction in Low and High Magnetic Fields* (Cuvillier, Göttingen, 2005), Ph.D. thesis.

[16] T. Demel, D. Heitmann, P. Grambow, and K. Ploog, Appl. Phys. Lett. **53**, 2176 (1988).

[17] C. Pels, *Ferromagnetic Electrodes for Spin Polarized Transport - Technology and Experiment* (Cuvillier, Göttingen, 2003), Ph.D. thesis.

[18] J. C. Sun and M. J. Bevan, Science **300**, 339 (2003).

[19] E. Shevchenko, D. Talapin, A. Kornowski, F. Wiekhorst, J. Kötzler, M. Haase, A. Rogach, and H. Weller, Adv. Mater. **14**, 287 (2002).

[20] F. Wiekhorst, E. Shevchenko, H. Weller, and J. Kötzler, Phys. Rev. B **67**, 224416 (2003).

[21] F. Luis, J. M. Torres, L. M. Garcia, J. Bartolom, J. Stankiewicz, F. Petroff, F. Fettar, J. L. Maurice, and A. Vaurs, Phys. Rev. B **65**, 094409 (2002).

[22] T. Ibusuki, S. Kojima, O. Kitakami, and Y. Shimada, IEEE Trans. Magn. **37**, 1295 (2001).

[23] E. V. Shevchenko, D. V. Talapin, A. L. Rogach, A. Kornowski, M. Haase, and H. Weller, J. Am. Chem. Soc. **124**, 11480 (2002).

[24] S. Sun, C. B. Murray, D. Weller, L. Folks, and A. Moser, Science **287**, 1989 (2000).

[25] V. F. Puntes, K. M. Krishnan, and A. P. Alivisatos, Science **291**, 2115 (2001).

[26] W. Wernsdorfer, D. Mailly, and A. Benoit, J. Appl. Phys. **87**, 5094 (2000).

[27] D. A. Brawner, N. P. Ong, and Z. Z. Wang, Nature **358**, 567 (1992).

[28] S. Wirtha and S. von Molnár, Appl. Phys. Lett. **76**, 3283 (2000).

[29] A. K. Geim, I. V. Grigorieva, S. V. Dubonos, J. G. S. Lok, J. C. Maan, A. E. Filippov, and F. M. Peeters, Nature **390**, 259 (1997).

[30] F. G. Monzon, D. S. Patterson, and M. L. Roukes, J. Magn. Magn. Mater. **195**, 19 (1999).

[31] G. Meier, D. Grundler, K.-B. Broocks, Ch. Heyn, and D. Heitmann, J. Magn. Magn. Mater. **210**, 138 (2000).

[32] A. Oral, S. J. Bending, and M. Henini, Appl. Phys. Lett. **69**, 1324 (1996).

[33] A. D. Kent, S. von Molnár, S. Gider, and D. D. Awschalom, J. Appl. Phys. **76**, 6656 (1994).

[34] M. Donahue and D. Porter, Object Oriented Micromagnetic Framework, http://math.nist.gov/oommf.

[35] R. Eiselt, Master's thesis, University of Hamburg, 2001.

[36] A. K. Geim, S. V. Dubonos, J. G. S. Lok, I. V. Grigorieva, J. C. Maan, L. Theil Hansen, and P. E. Lindelof, Appl. Phys. Lett. **71**, 2379 (1997).

[37] X. Q. Li and F. M. Peeters, Superlattices and Microstructures **22**, 2 (1997).

[38] H. U. Baranger, D. P. DiVincenzo, R. A. Jalabert, and A. D. Stone, Phys. Rev. B **44**, 10637 (1991).

[39] F. M. Peeters and X. Q. Li, Appl. Phys. Lett. **72**, 572 (1998).

[40] S. J. Bending and A. Oral, J. Appl. Phys. **81**, 3721 (1997).

[41] Y. Martin and H. K. Wickramasinghe, Appl. Phys. Lett. **50**, 1455 (1987).

[42] G. Binnig, H. Rohrer, Ch. Gerber, and E. Weibel, Phys. Rev. Lett. **49**, 57 (1982).

[43] U. Hartmann, Phys. Lett. A **137**, 475 (1989).

[44] V. Elings and J. Gurley, US Patent No. 5308974, Digital Instruments, Santa Barbara, CA, 1994.

[45] S. McVitie, G. S. White, J. Scott, P. Warin, and J. N. Chapman, J. Appl. Phys. **90**, 5220 (1994).

[46] A. Wadas and H. J. Güntherodt, Phys. Lett. A **146**, 277 (1990).

[47] M. Barthelmeß, *Magnetic-force microscopy and micromagnetic simulations on domains of structured ferromagnets* (http://www.sub.uni-hamburg.de/opus/volltexte/2004/2245/, Hamburg, University, 2004), Ph.D. thesis.

[48] P. Fischer, G. Schütz, G. Schmahl, P. Guttmann, and D. Raasch, Z. Phys. B: Condensed Matter **101**, 313 (1996).

[49] W. Chao, E. Anderson, G. P. Denbeaux, B. Harteneck, J. A. Liddle, D. L. Olynick, A. L. Pearson, F. Salmassi, C. Y. Song, and D. T. Attwood, Opt. Lett. **28**, 2019 (2003).

[50] P. Fischer, T. Eimüller, G. Schütz, G. Denbeaux, A. Lucero, L. Johnson, D. Attwood, S. Tsunashima, M. Kumazawa, N. Takagi, M. Köhler, and G. Bayreuther, Rev. Sci. Instr. **72**, 2322 (2001).

[51] P. Fischer, T. Eimüller, G. Schütz, P. Guttmann, G. Schmahl, K. Pruegl, and G. Bayreuther, J. Phys. D **31**, 649 (1998).

[52] P. Fischer, T. Eimüller, G. Schütz, M. Köhler, G. Bayreuther, G. Denbeaux, and D. Attwood, J. Appl. Phys. **89**, 7159 (2001).

[53] G. Meier, R. Eiselt, M. Bolte, M. Barthelmeß, T. Eimüller, and P. Fischer, Appl. Phys. Lett. **85**, 1193 (2004).

[54] M. Bolte, R. Eiselt, T. Eimüller, P. Fischer, and G. Meier, J. Magn. Magn. Mater. **290–291**, 723 (2005).

[55] L. Bergmann and C. Schaefer, *Lehrbuch der Experimentalphysik, Band 6, Festkörper* (Walter de Gruyter, Berlin, 1992).

[56] Ch. Kittel, *Introduction to Solid State Physics* (Wiley, New York, 2005).

[57] P. Weiss, J. Phys. **6**, 661 (1907).

[58] W. Heisenberg, Z. Physik **49**, 619 (1928).

[59] S. Chikazumi, *Physics of Ferromagnetism* (Oxford University Press, Oxford, 1997).

[60] C. Zener, Phys. Rev. **81**, 440 (1951).

[61] O. K. Andersen, J. Madsen, U. K. Paulsen, O. Jepsen, and J. Kollar, *Proc. Int. Conf. Magnetism 1976, Vol. I* (North-Holland, Amsterdam, 1976).

[62] I. I. Mazin, Phys. Rev. Lett. **83**, 1427 (1999).

[63] W. F. Brown, Phys. Rev. **58**, 736 (1940).

[64] W. F. Brown, *Micromagnetics* (Interscience Publishers, New York, 1963).

[65] L. Landau and E. Lifshitz, Physik. Z. Sowjetunion **8**, 153 (1935).

[66] W. F. Brown, Phys. Rev. **60**, 139 (1941).

[67] A. Aharoni, *Introduction to the Theory of Ferromagnetism* (Clarendon, Oxford, 1996).

[68] T. L. Gilbert, Phys. Rev. **100**, 1243 (1955).

[69] F. Bloch, Z. Phys. **74**, 295 (1932).

[70] L. Néel, Compt. Rend. **241**, 533 (1955).

[71] H. Kronmüller and M. Fähnle, *Micromagnetism and the Microstructure of Ferromagnetic Solids* (Cambridge University Press, Cambridge, 2003).

[72] H. D. Dietze and H. Thomas, Z. Phys. **163**, 523 (1961).

[73] W. F. Brown and A. E. LaBonte, J. Appl. Phys. **36**, 1380 (1965).

[74] M. Barthelmeß, A. Thieme, R. Eiselt, and G. Meier, J. Appl. Phys. **93**, 8400 (2003).

[75] E. E. Huber, D. O. Smith, and J. B. Goodenough, J. Appl. Phys. **29**, 8400 (1958).

[76] D. D. Awschalom, M. E. Flatté, and N. Samarth, Scientific American **286**, 53 (2002).

[77] S. A. Wolf, D. D. Awschalom, R. A. Buhrman, J. M. Daughton, S. von Molnár, M. L. Roukes, A. Y. Chtchelkanova, and D. M. Treger, Science **294**, 1488 (2001).

[78] D. Grundler, Physics World **15**, 39 (2002).

[79] S. Datta and B. Das, Appl. Phys. Lett. **56**, 665 (1990).

[80] T. Dietl, H. Ohno, F. Matsukura, J. Cibert, and D. Ferrand, Science **287**, 1019 (2000).

[81] R. A. de Groot, F. M. Mueller, P. G. van Engen, and K. H. J. Buschow, Phys. Rev. Lett. **50**, 2024 (1983).

[82] W. E. Pickett, J. S. Moodera, Phys. Today **54**, 39 (2001).

[83] T. Matsuyama, C.-H. Hu, D. Grundler, G. Meier, and U. Merkt, Phys. Rev. B **65**, 155322 (2002).

[84] F. G. Monzon, M. Johnson, and M. L. Roukes, Appl. Phys. Lett. **71**, 3087 (1997).

[85] G. Meier and T. Matsuyama, Appl. Phys. Lett. **76**, 1315 (2000).

[86] C. W. J. Beenakker and H. van Houten, Phys. Rev. B **63**, 1857 (1989).

[87] R. J. Blaikie, K. Nakazato, J. R. A. Cleaver, and H. Ahmed, Phys. Rev. B **46**, 9796 (1992).

[88] R. M. Bozorth, *Ferromagnetism* (Wiley, New York, 1994).

[89] G. Meier, R. Eiselt, and M. Halverscheid, J. Appl. Phys. **92**, 7296 (2002).

[90] J. M. García, A. Thiaville, J. Miltat, K. J. Kirk, J. N. Chapman, and F. Alouges, Appl. Phys. Lett. **79**, 656 (2001).

[91] C. P. Bean and J. D. Livingston, Suppl. J. Appl. Phys. **30**, 120S (1959).

Danksagung

Diese Arbeit wäre ohne den Einsatz und Mühen vieler Menschen nicht möglich gewesen. Ich bin sehr dankbar für die Unterstützung und eingehende Hilfe, die ich in den letzten Jahren zur Vollendung der Dissertation erfahren habe. Mein Dank gilt..

- Prof. Dr. Ulrich Merkt für die Möglichkeit, diese Arbeit in seiner Forschungsgruppe anzufertigen sowie die stete Unterstützung und sein Vertrauen, die Betreuung der Rasterelektronenmikroskope an mich zu übergeben,
- Prof. Dr. Wolfgang Hansen für die Übernahme des Zweitgutachtens der Dissertation,
- Prof. Dr. Detlef Heitmann für die Übernahme des Zweitgutachtens der Disputation.

Mindestens ebenso wichtig wie das Thema einer Arbeit ist nach meinen Erfahrungen sowohl eine umfassende Betreuung als auch eine nette Atmosphäre innerhalb der Arbeitsgruppe. Ich freue mich, dass dieser Zustand immer erfüllt war und bedanke mich bei allen Mitgliedern der Gruppe N für die schöne Zeit. Inbesondere bedanken möchte ich mich bei..

- PD Dr. habil. Guido Meier für die Leitung des Teilbereichs "Hybrid Quantum Structures" und das intensives Engagement innerhalb der Gruppe. Niemand sonst kann seine physikalische Begeisterung so eingehend auf andere übertragen wie er.
- Dr. Toru Matsuyama für die Hilfe bei der Lösung von physikalischen und technischen Fragestellungen mit einem fundamentalen Know-How. Es ist beeindruckend mit welcher Leidenschaft er vermeintlich unlösbare Aufgaben überwindet.
- Dr. Christian Pels dafür, dass er als Ansprechpartner zu und in allen Situationen zur Verfügung stand. Die Skate-Runden um die Alster sind legendär und der nächste Marathon kommt bestimmt.
- Dr. Peter Baars für die Erkenntnis, dass der Büroalltag nicht nur für wissenschaftlich-orientierte Arbeit geeignet ist. Man muss auch mal ein Späßchen machen.
- Dr. Marcus Steiner für ein stets offenes Ohr, den zahlreichen Tips und hilfreichen Unterhaltungen zur Laborarbeit. Ein nettes Pläusch'chen ist immer drin.
- Dr. Christopher Schierholz für die Quelle des Wissens bei allen Fragen zur Programmierung von Igor über Delphi bis Latex sowie den kritischen Diskussionen von Ergebnissen und ob die überhaupt Sinn machen.

- Dr. Alexander van Staa für die Kooperation Rund um den Kryostaten und den Support der Sputter-Anlagen. Denkwürdig sind die ausgelassenen Squash-Abende und zahllosen Stammtisch-Plaudereien. Die Perfektion der Zweideutigkeit liegt bei ihm.

- Dipl.-Phys. Sebastian von Oehsen für wertvolle Diskussionen beim Aufbau der Messplätze und Verfeinerung der Präparationstechniken. Ich freue mich, dass er mit großem Anteil die Gruppendynamik in Schwung gehalten hat. Die Vielfältigkeit der Lokalitäten bleibt für mich faszinierend und alle gemeinsamen Abende in sehr schöner Erinnerung.

- Dipl.-Phys. Jan Michael Scholtyssek für alle innovativen Hilfestellungen und die höchst trickreichen "Basteleien", insbesondere auch der Doktorhüte. Das Klettern am DAV-Turm und Bezwingen neuer Routen macht immer besonders viel Spass.

- Dipl.-Phys. / Dipl.-Inf. Markus Bolte für die zahlreichen Simulationsrechnungen und die Planung von Hochfrequenzbauelementen sowie für die erfolgreichen Messaufenthalte in Berkeley.

- Dipl.-Phys. Christian Uhrich und Dipl.-Phys. Jann Kruse für die schöne gemeinsame Zeit während ihrer Diplomarbeiten.

Seit dem Beginn meiner Promotion hat sich die Zusammenarbeit aller Gruppen unseres Instituts deutlich intensiviert. Der Austausch und die Nutzung anderer Laborgerätschaften ist nicht selbstverständlich. Daher danke ich allen Mitgliedern der anderen Gruppen des Instituts für die freundliche Koorperation und die vielen konstruktiven Diskussionen auch mal über die Physik hinaus. Zudem ist ein Großteil der Laborarbeit nur durch den technischen Support vieler Angestellter des Instituts möglich. Vielen Dank an Jerzy Gancarz, Thomas Finger, Wolfgang Hatje, Klaus Ahrens, Rolf Benecke, Horst Biedermann, die mechanische und elektronische Werkstatt, wie auch die Mitglieder der Verwaltung und die Sekretärin unserer Gruppe Petra Roth.
Für die Unterstützung jenseits physikalischer Themen und ausserhalb der Institutsgrenzen möchte ich mich bei meiner Familie und allen meinen Freunden bedanken, die mich tatkräftig am Wochenende und auch mal in der Woche auf andere Gedanken gebracht haben. Mein ganz besonderer Dank gilt..

- Meiner Freundin Kristina für ihre Liebe und ihre Offenherzigkeit sowie für ihr Verständnis an den Tagen und Nächten vieler Arbeit. Sie hat mir jederzeit neuen Schwung und viel Ausgeglichenheit gegeben.

- Meinen Eltern für ihre umfassende Unterstützung und unentwegte Hilfsbereitschaft sowie für ihr Vertrauen in mich und meine Arbeit. Ich freue mich, dass ich stets Rückhalt durch sie erfahren konnte.